

Felix Reimold

## **Numerical simulations of tungsten impurity transport in ASDEX-Upgrade with EIRENE**

**IPP 17/27  
Mai, 2011**



# **Numerical simulations of tungsten impurity transport in ASDEX-Upgrade with EIRENE**

Physik-Department der  
Technischen Universität München (TUM)  
&  
Max-Planck-Institut für Plasmaphysik (IPP)

Diplomarbeit vorgelegt von  
Felix Reimold





# Numerical simulations of tungsten impurity transport in ASDEX-Upgrade with EIRENE



Physik-Department der  
Technischen Universität München (TUM)  
&  
Max-Planck-Institut für Plasmaphysik (IPP)

Diplomarbeit vorgelegt von  
Felix Reimold

Erstgutachter: Prof. Dr. S. Günter  
Zweitgutachter: Prof. Dr. J. Finley

May 10, 2011



---

## Abstract

---

This report deals with numerical simulations of tungsten impurity transport[1][2] in the all-tungsten device ASDEX Upgrade[3]. A new version of the kinetic Monte-Carlo code EIRENE[4] including a new Trace-Ion Module (TIM)[5][6] was employed to perform numerical simulations on fixed SOLPS plasma backgrounds[7]. The magnetic equilibria are based on ASDEX-Upgrade L- and H-Mode discharges. Seebacher's Trace-Ion Module includes the effects of  $\vec{E} \times \vec{B}$ , curvature and grad B drift and a Fokker-Planck collision term[6][8][9] in velocity space into EIRENE for kinetic ion tracing in a gyroaveraged approach. The current version of EIRENE is not coupled to a fluid code. Hence, the plasma backgrounds are fixed and the tungsten impurities are treated in the trace approximation.

Results of the presented studies are the evaluation of the tungsten transport description of the Trace-Ion Module as well as the determination of the core penetration probability of tungsten impurity released at different positions at the divertor targets and the limiting structures in the main chamber. The evaluation of the transport model was done by benchmarking the results to NEOART calculations[10][11].

The report starts with an overview of different theoretical models EIRENE is based on. The introduction comprises three parts: Sources, Transport and Reactions. Subsequently, the numerical tools used in this thesis are presented. Apart from a general overview of available state-of-the-art codes, EIRENE is introduced in detail with respect to its implementation. Code improvements accomplished in the course of this work are presented along with the setup preparations of the EIRENE simulations.

An analysis of the applicability of the EIRENE code to tungsten transport studies in ASDEX Upgrade plasmas is performed. Several problems, including thermalization and numerical drifts, are discussed. Moreover, a benchmark of the Trace-Ion Module transport against NEOART results is conducted and last but not least simulation results for L- and H-Modes plasmas at different separatrix electron densities are evaluated. The core penetration probability and characteristic features of the tungsten profiles are discussed.



---

# Contents

---

1	Introduction	1
1.1	Nuclear Fusion . . . . .	2
1.2	Magnetic Confinement . . . . .	4
1.3	Impurities . . . . .	7
1.4	Scope of Thesis & Key Results & Structure . . . . .	9
2	Prerequisites	11
2.1	Sources . . . . .	11
2.1.1	Sputtering & Self-Sputtering . . . . .	12
2.1.1.1	Physical Sputtering . . . . .	13
2.1.1.2	Chemical Sputtering . . . . .	15
2.1.1.3	Prompt Redeposition . . . . .	16
2.2	Transport . . . . .	19
2.2.1	Classical Transport . . . . .	20
2.2.2	Neoclassical Transport . . . . .	24
2.2.2.1	Correction for Classical Transport . . . . .	26
2.2.2.2	Pfirsch-Schlüter Regime . . . . .	27
2.2.2.3	Banana Regime . . . . .	29
2.2.2.4	Plateau Regime . . . . .	31
2.2.2.5	Total Neoclassical Radial Fluxes . . . . .	32
2.2.2.6	Limitations of Neoclassical Transport Theory . . . . .	32
2.2.3	Anomalous Transport . . . . .	32
2.3	Reactions . . . . .	33
2.3.1	Plasma-Particle Interaction . . . . .	33
2.3.1.1	Inelastic Collisions . . . . .	33
2.3.1.2	Elastic Collisions . . . . .	35
2.3.2	Plasma-Wall Interactions . . . . .	36
2.3.2.1	Sputtering . . . . .	36
2.3.2.2	Reflection & Absorption . . . . .	36
3	Numerics	39
3.1	Motivation of Choice . . . . .	39
3.1.1	Available numerical tools . . . . .	40
3.2	EIRENE . . . . .	42
3.2.1	Applied Approximations . . . . .	42
3.2.2	Monte-Carlo Principles . . . . .	43
3.2.3	Introduction & Program Flow . . . . .	43
3.2.4	Sources . . . . .	44



3.2.5	Transport . . . . .	45
3.2.5.1	Neutral Transport . . . . .	45
3.2.5.2	Ion Transport . . . . .	46
3.2.6	Reactions . . . . .	47
3.2.6.1	Plasma-Particle Interactions . . . . .	47
3.2.6.2	Plasma-Wall Interactions (PWI) . . . . .	48
3.3	EIRENE Updates . . . . .	50
3.3.1	Upgrades & New Routines . . . . .	50
3.3.1.1	Sputtering . . . . .	51
3.3.1.2	Prompt Redeposition . . . . .	52
3.3.1.3	Electric Potential . . . . .	54
3.3.1.4	Perpendicular Diffusion . . . . .	54
3.3.1.5	Renewed Parallelization of EIRENE . . . . .	56
3.3.1.6	BGK-thermalization . . . . .	57
3.3.1.7	Bug Fixes . . . . .	59
3.3.2	EIRENE Preparations . . . . .	59
3.3.2.1	Mesh Generation . . . . .	59
3.3.2.2	B-field Generation . . . . .	60
3.3.2.3	Plasma Background Generation . . . . .	61
3.4	Other Numerical Codes . . . . .	63
4	Results . . . . .	65
4.1	Code Tests . . . . .	65
4.1.1	Applicability of Code . . . . .	67
4.1.2	Temperatures and Thermalization in EIRENE . . . . .	71
4.1.3	Parameter & Sensitivity Scans . . . . .	75
4.2	Benchmark against NEOART . . . . .	77
4.3	Profile Calculations & Penetration Probability . . . . .	82
4.3.1	Profiles . . . . .	82
4.3.2	Penetration Probability . . . . .	84
5	Summary & Outlook . . . . .	89
5.1	Summary . . . . .	89
5.2	Outlook . . . . .	90
	Bibliography . . . . .	93
A	Appendix . . . . .	101
A.1	EIRENE Standard Input . . . . .	101
A.2	EIRENE Source coordinates & Divertor Target Langmuir Data . . . . .	102
A.3	Plasmabackground Profiles . . . . .	104
A.4	EIRENE Program Flowcharts . . . . .	107
A.5	Derivation of Monte-Carlo Transport Calculations . . . . .	108
A.6	SOLPS Fluid Equations . . . . .	110
A.7	Mean free path - First Ionization . . . . .	112

# CHAPTER 1

---

## Introduction

---

At present and probably also in the future one of the most important resources deciding on a nation's wealth and prospects is and will be energy and related resources[12]. The last three decades displayed a constant rise of need for energy. With limited resources at hand[13] this is as ever a driving force for scientific research and technical innovations. It is of course as well a potential source of economic wealth and (armed) conflicts[14]. With natural resources depleting[15; 16] and unacceptable impact of traditional combustive energy production on the fate of humankind – such as global warming[17; 18] – the energy production process has to be reconsidered and reinvented. Efficiencies are to be increased dramatically, resources have to be recycled at all levels of consumptions, harmful products are to be reintegrated in the production cycle and remaining waste has to be disposed of properly to reach the ultimate goal of a sustainable economy and society. The search for substitutions of traditional energy sources has set in in the last decades and is continued now at a higher pace. Recent years raised awareness of these problems related to sustainability and ecological impact[19].

Nuclear fusion is a possible candidate for producing baseload electric power in the future energy production schemes. Fusion provided baseload supplemented with renewable energies like wind- and solar power – with temporal fluctuations – combined with new energy storage concepts could ensure a sustainable and feasible production mix in existing and adapting infrastructures.

Nuclear fusion is the process fueling the most powerful energy source in our solar system – the sun, which constantly radiates a power of  $3.85 \times 10^{26}$  W. Tapping into this powerful energy source is the main goal of the fusion research community. Fortunately – for scientists – there are a lot of interesting and difficult problems to be dealt with before an economical, operating power plant can supply the first fusion energy to the electric grid[20].

This introduction will give a short introduction to nuclear fusion, specializing on magnetic confinement systems and then explaining the importance and impact of impurities in a fusion plasma.

## 1.1 Nuclear Fusion

The process of two particles colliding and forming a new element with higher atomic number is called nuclear fusion. This process is the opposite to nuclear fission. Nuclear fusion is affecting the nucleus structure and thus involving energies on the order of MeV. As fission this make the reaction process so interesting for energy production. Figure 1.1 depicts the average binding energy of a single nucleon over the mass number of different elements. The Fig. shows that fission is exothermic for High-Z elements just down to iron  $^{56}_{26}\text{Fe}$  with the maximum binding energy per nucleon. Fusion only is exothermic up to the same iron  $^{56}_{26}\text{Fe}$ . Most energy is gained in fusion processes transforming hydrogen isotopes H,D,T or  $^3_2\text{He}$  to  $^4_2\text{He}$ .

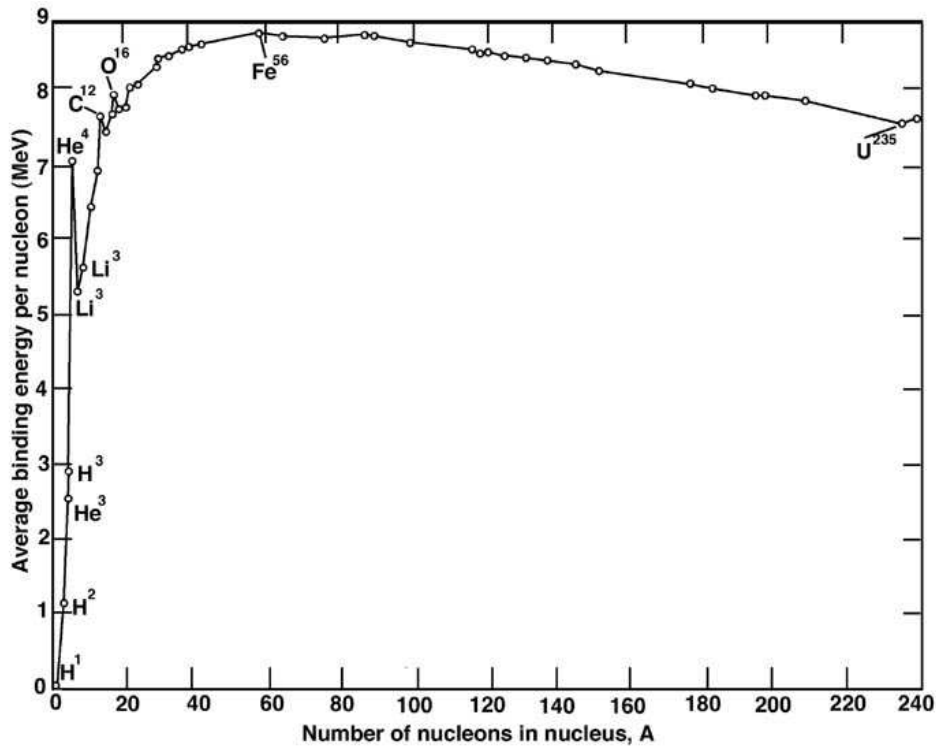
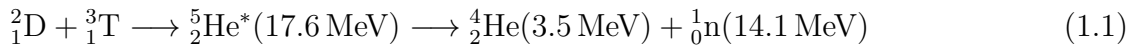


**Figure 1.1:** Average binding energy per nucleon over nucleon number[21].

A future power plant will most likely be based the fusion reaction given in Eq. (1.1). It exhibits the highest reaction cross-section of the hydrogen isotope reactions shown in Fig. 1.2. The large cross-section of this particular reaction results from a resonant energy level in the  $^5_2\text{He}$  nucleus. The transient  $^5_2\text{He}$  state decays to  $^4_2\text{He}$  and a neutron.



The maximum cross-section, as well as the maximum reaction rate, is reached for a ion temperature of approximately 64 keV – equivalent to roughly 700 Mio.°C. The plasma ion temperature future fusion devices have to sustain therefore are of at least several tens of keV. For a magnetically confined plasma, where particles thermalize (c.f. Sec. 1.2), technically feasible plasma temperatures of about 10 keV are sufficient to start fusion reactions. Particles in the high energy tail of the Maxwell distribution can overcome the Coulomb barrier. Along with the large energy gain of 17.6 MeV per reaction, an additional plus of the particular reaction is that none of the fusion products is a long-living

radioactive isotope. Neutrons and the subsequently produced positrons can be easily shielded by paraffin and concrete casings. However neutrons still activate the vessel structure and thus produce radioactive waste with envisioned decay times of about 100 years[22–24].

A economic consideration for energy production by Reaction (1.1) is the availability of the 'raw materials' deuterium and tritium. Deuterium can be distilled from usual tape water at reasonable prices. Tritium is radioactive with a decay time of approximately twelve days, which is why there are no considerable, 'natural' tritium resources. Tritium supply shall be assured by breeding of lithium in the so-called blanket. The blanket is a cavity between the first-wall and the vessel casing. A variety of lithium species and composites are tested in combination with neutron multipliers like Beryllium[25; 26]. The European Fusion Development Agreement (EFDA) organization is optimistic on the availability of necessary resources[20]:

The lithium from one laptop battery, combined with the deuterium in 100 liters of water, can cover the electricity use of an average European citizen for 30 years.

Considering fusion for energy production a confinement scheme has to be set up. Particles and kinetic energy have to be confined sufficiently long to enable enough nuclei collisions at sufficient temperature to result in fusion reactions. In addition to gravitational confinement, realized inside stars like the sun, one idea is inertial confinement. Pure momentum conservation guarantees a good energy confinement on very short timescales. In inertial fusion experiments small fuel pellets composed of deuterium and tritium are isotropically and homogeneously heated by laser or ion beams. The very intense heating (1 MJ) of the pellet within 15 ns[27] leads to ablation of the outermost pellet shell. The recoil compresses the inner parts of the pellet, thus initiating fusion reactions. The compression and the energy influx ensure both, confinement and heating, at the same time. However the necessary homogeneous and isotropic nature of the compression and connected instability problems still are a major challenge for scientists. The pulsed nature of the process with very short pulse lengths (ns) and necessarily high repetition frequencies of about 1 Hz is a problem for the use of energy production. Still laser utilities are not able to provide sufficiently frequent laser pulses at such high intensities. Pumping requirements to reach good vacuum conditions, necessary for isotropic and homogeneous heating, as well as the intense heat and particle loads on the first-wall materials will be a limiting factor for economic operation of a power plant.

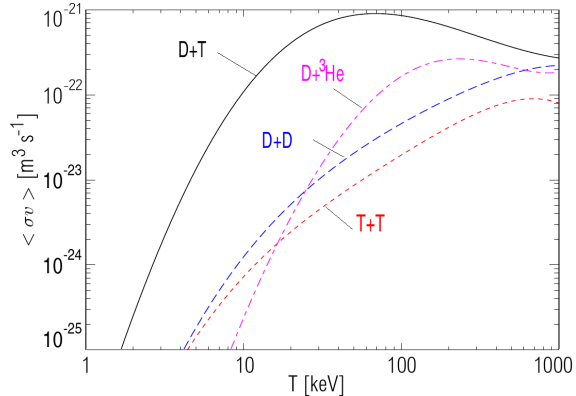


**Figure 1.2:** Reaction rates of potential fusion reactions[1].

## 1.2 Magnetic Confinement

Another scheme pursued in fusion research is the magnetic confinement of plasma. Temperatures of order of 10 keV and densities on the order of  $10^{20} \text{ m}^{-3}$  are achieved with a toroidal magnetic field with an increasing helicity along the minor radius going from the magnetic axis to the edge<sup>1</sup>. The actual field strength of a few  $T$  depends on the plasma pressure that shall be confined ( $\beta = p/2\mu_0 B^2 \approx 1 - 5\%$ ).

There are basically two magnetic configuration in fusion science different mainly in the approach of how the poloidal magnetic field is generated. The tokamak design, shown in Fig. 1.3, uses a toroidal plasma current, driven by an induced electric field, to produce the poloidal magnetic field. The stellarator as a competing concept does not rely on a current to generate magnetic fields. The field is produced uniquely by a complicated set of sophisticated field coils. Currently the tokamak design is largely dominating the present scientific research activities. However both configurations rely on the same fact of gyro-motion of electrically charged particles in magnetic fields. The gyro-motion is caused by the Lorentz force. It forces charged particles on helical trajectories around magnetic field lines. Closing these field lines on themselves in a toroidal geometry provides a possible confinement for plasma. Confined particles can experience collisions without being necessarily lost from the fusion plasma due the scattering. Particles and energy are thus confined and collisional plasma heating by the reaction secondary He is made possible.

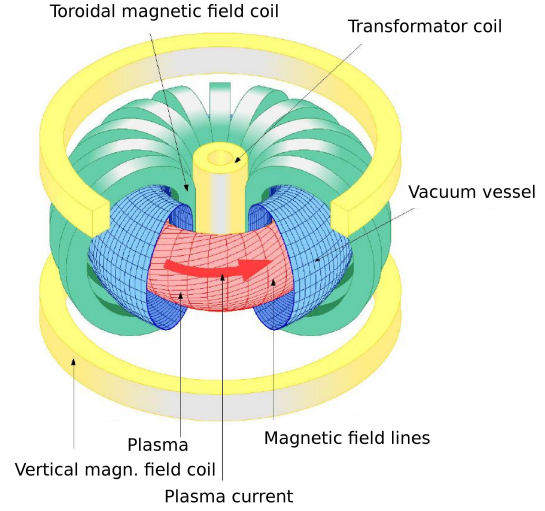


**Figure 1.3:** The tokamak fusion reactor design. Magnetic field coils produce the toroidal magnetic field  $B_t$ , while transformer coils induce the plasma current  $I_P$  to generate the poloidal magnetic field  $B_p$ [28].

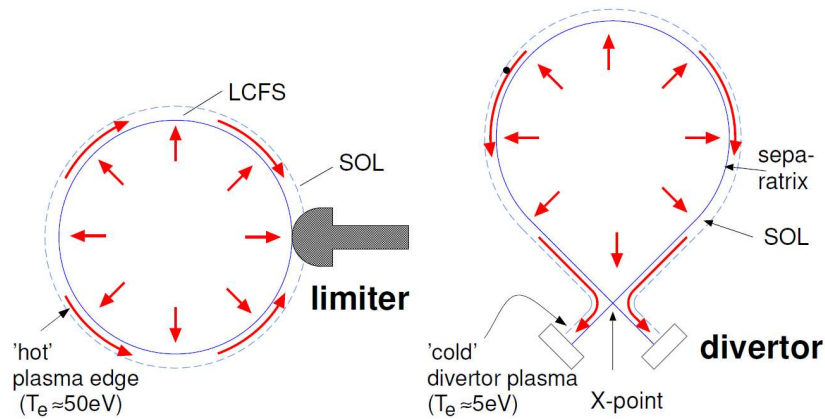


**Figure 1.4:** Limiter and divertor geometry of plasma and magnetic field[1].

<sup>1</sup> The increasingly helical geometry of the magnetic field lines is designed to suppress particle drifts due to the inhomogeneity of the toroidal field ( $\nabla B$ ,  $\text{curv } B$ ,  $\vec{E} \times \vec{B}$ ) and to avoid instabilities (Kink, Sausage, Interchange, etc.).

For magnetic confinement experiments two major magnetic field geometries can be distinguished. Figure 1.4 shows both, the limiter and the divertor configuration respectively. In limiter geometry the last closed flux surface (LCFS) is determined by the intersection of the magnetic field with the limiter. The limiter is in direct contact with the hot plasma. Intense plasma-wall interaction in direct neighborhood to the core plasma leads to a considerable amount of impurities in the plasma. The plasma density radially outward from the LCFS decays exponentially<sup>1</sup>. With the limiter virtually scraping off the outermost plasma layers, this outer part of the plasma is called Scrape-Off Layer (SOL)[29].

In divertor geometry an additional magnetic field coil introduces an X-point with zero magnetic field strength and thus a LCFS – the so-called separatrix<sup>2</sup> – without direct contact to the walls. The central plasma core is thus confined inside the LCFS without direct contact to the walls. The connection length<sup>3</sup> is considerable despite poloidally short distances to the target and the strikepoints ( $\sim 0.5$  m) as particle motion is mainly parallel and thus toroidal. Ideally the principle plasma-wall interaction (PWI) is therefore restricted to the divertor. The divertor geometry is optimized to have cold (10 eV), denser plasma in front of the target to make efficient He-ash pumping possible (compression) and to ensure the thermal stability (radiation cooling & CX-friction) of the wall material[30; 31]. Sputtering processes are also largely suppressed. Long connection lengths from the PWI zone to the core plasma also reduce the impurity content of the core and ensure good recycling conditions.

The Max-Planck-Institut für Plasma-physik (IPP) operates a tokamak called AxisSymetric Divertor EXperiment Upgrade (ASDEX Upgrade). A poloidal cut of the vessel geometry along with one of the employed magnetic configurations is shown in Fig. 1.5. ASDEX Upgrade (AUG) is the only full-tungsten tokamak device in the world and contributes to the development of tungsten as a first-wall material in future fusion devices. The operational parameters of ASDEX Upgrade are given in Tab. 1.1.

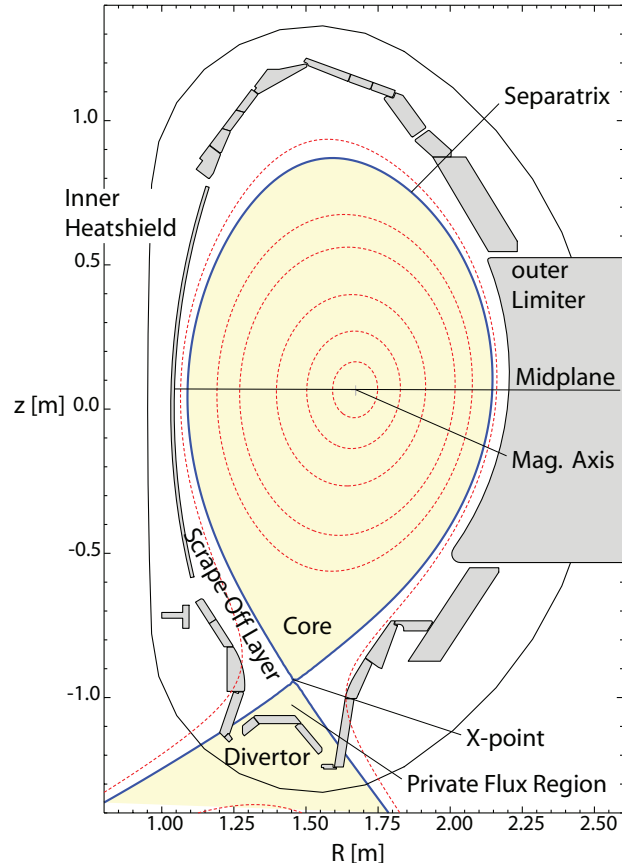


**Figure 1.5:** Poloidal cross-section of the ASDEX Upgrade vessel with a typical magnetic configuration and the standard radial coordinate  $q_p$  indicated in red. The old divertor configuration DivIIb, shown here, is used in all presented simulations.

- 1 Parallel motion, with respect to magnetic field lines, is orders of magnitudes faster than perpendicular transport. Particles on flux surfaces will hit the limiter before being able to travel great distances in the radial direction.
- 2 The separatrix denotes both, the whole flux surface with zero magnetic field on it and only the LCFS leaving out the Private Flux Region (PFR).
- 3 The connection length is the distance from wall to wall along magnetic field lines. It is a measure of distance between the core plasma and the walls[29].

At AUG's predecessor ASDEX the discovery of the first high-confinement mode (H-Mode) was successfully published in 1982 by Wagner[32]. At fixed electron density H-mode can be achieved by sufficiently strong external heating of (clean) plasmas. A sudden transition from the low-confinement mode (L-Mode) to H-mode then occurs and the pressure gradient in the pedestal rises sharply by forming an Edge Transport Barrier (ETB). H-Mode will be the confinement scheme on which all future fusion devices will base their operation. One possible explanation for the ETB in the pedestal is strong  $\vec{E} \times \vec{B}$ -shearing by electric fields inhibiting turbulent transport by destroying vortices[33]. Neoclassical transport is dominant in the ETB. However the H-Mode is not yet fully understood and remains an active domain of scientific research.

Quantity	
Major Radius	1.65 m
Minor Radius	0.5 m
Plasma Volume	14 m <sup>3</sup>
Ellipticity	1.8
Triangularity	0.4
Puls length	< 10 s
Plasma current	0.4 – 1.6 MA
Plasma temperature	60 – 100 Mio.°C
Plasma density (electrons)	10 <sup>20</sup> m <sup>-3</sup>
Ohmic Heating Power	1 MW
NBI Heating Power	20 MW @ 60 & 100 keV
ICR Heating Power	6 MW @ 30 – 40 MHz
ECR Heating Power	4 MW @ 105 & 140 GHz

**Table 1.1:** Operation parameters for ASDEX Upgrade at IPP Garching[3].

A figure of merit in fusion science is the so-called Q-Factor defined by the fusion power  $P_{fus}$  and the external heating power  $P_{ext}$ .

$$Q = \frac{P_{fus}}{P_{ext}} \quad (1.2)$$

Nowadays devices operate well below the break-even ( $Q = 1$ ). Top values of only  $Q = 0.6$  have been reached in D-T fusion experiments at JET[34]. The energetic  $\alpha$ -particles produced by fusion reactions shall heat the plasma in future fusion devices. They have to supply power equal to heat and radiation losses in steady state. A plasma solely heated by  $\alpha$ -particles ( $Q \rightarrow \infty$ ) is called ignited or burning. Additional, external heating will be applied for control and diagnostic reasons. Energy losses caused by impurity radiation play a crucial role in attaining the burn condition, especially with tungsten impurities.

## 1.3 Impurities

Lawson developed a criterion a plasma has to fulfill (c.f. Eq. (1.3)) in order to be able to ignite. The Lawson criterion results from balancing out the heating by  $\alpha$ -particles with the loss mechanisms of (impurity) radiation, fuel dilution and a limited energy confinement time. The Lawson triple product imposes limits on ion temperature  $T_i = T_e = T$ , electron density  $n_e$  and energy confinement time  $\tau_E$ .

$$n_e T \tau_E \geq 10^{21} \text{ keVsm}^{-3} \quad (1.3)$$

Ideally a fusion plasma consists only of the three reaction species plus electrons. In reality impurities are always present in the plasma due to PWI and gas puffing. Like He, impurities can dilute the core plasma and thereby decreases the fuel concentration. Fuel dilution reduces the number of fusion reactions. Even worse, High-Z elements like tungsten show two negative properties for fusion plasmas[2; 35; 36]. One, they tend to exhibit central accumulation, which must be counteracted by central heating (temperature screening, c.f. Subsec. 2.2.1)[37]. Two, High-Z elements are not fully ionized at temperatures found in the core plasma. They contribute to radiation losses of the core not only by bremsstrahlung, but also by line radiation[38]. Line radiation very effectively cools the core plasma and eventually termi-

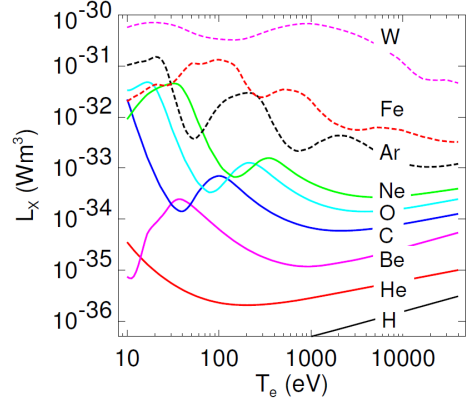


**Figure 1.6:** Radiation profiles of several impurities[1].

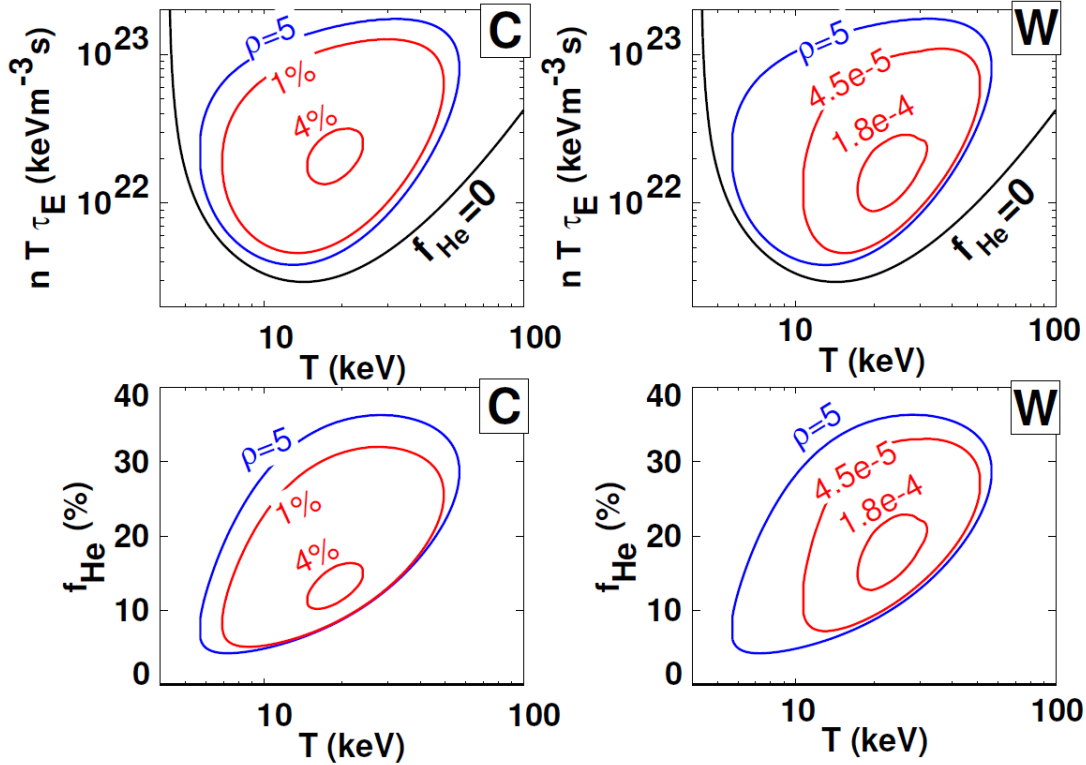


**Figure 1.7:** Impurity concentrations and operational space limitations for ignited plasma[1].



rates the fusion plasma in a disruption[39]. The sensitivity of the available operational space to different kinds of impurities is strongly varying as shown in Fig. 1.7. Tungsten is a challenging choice as a first-wall material, because the allowed impurity concentration to guarantee operation is rather restrictive.

Nonetheless future fusion devices are likely to have tungsten based first-wall materials. Tungsten exhibits the highest sputtering thresholds and the lowest sputtering yields due to its high mass (184 AU) and its high surface binding energy (8.6 eV). Unlike carbon, tungsten is not subject to chemical sputtering. Figure 1.8 shows a compilation of sputtering yields for sputtering by  $D^+$ -ions. The sputtering yield for tungsten in Fig. 1.8 are exaggerated, because prompt redeposition effects are neglected in the calculations. Due to very low erosion yields tungsten is now widely recognized as the most probable candidate for future fusion devices' plasma facing components (PFC). The low erosion could guarantee sufficiently long maintenance intervals to operate a reactor economically despite the necessary low concentrations of High-Z elements in the plasma. Safety issues with radioactivity by activation and co-deposition of radioactive tritium are also reduced with tungsten[40].

In contrast to High-Z elements, lighter elements like  $N_2$ , Ne and Ar are deliberately introduced into the SOL by gas puffing in order to form a radiative mantle[41]. The radiative mantle spreads the power load of the outflowing energy crossing separatrix into SOL over a wider wall area<sup>1</sup>

The impact of impurities on the plasma performance assigns a crucial role to impurity handling in the setup and control of a fusion plasma. The development and the enhancement of predictive capabilities regarding the effect, the sources and the transport

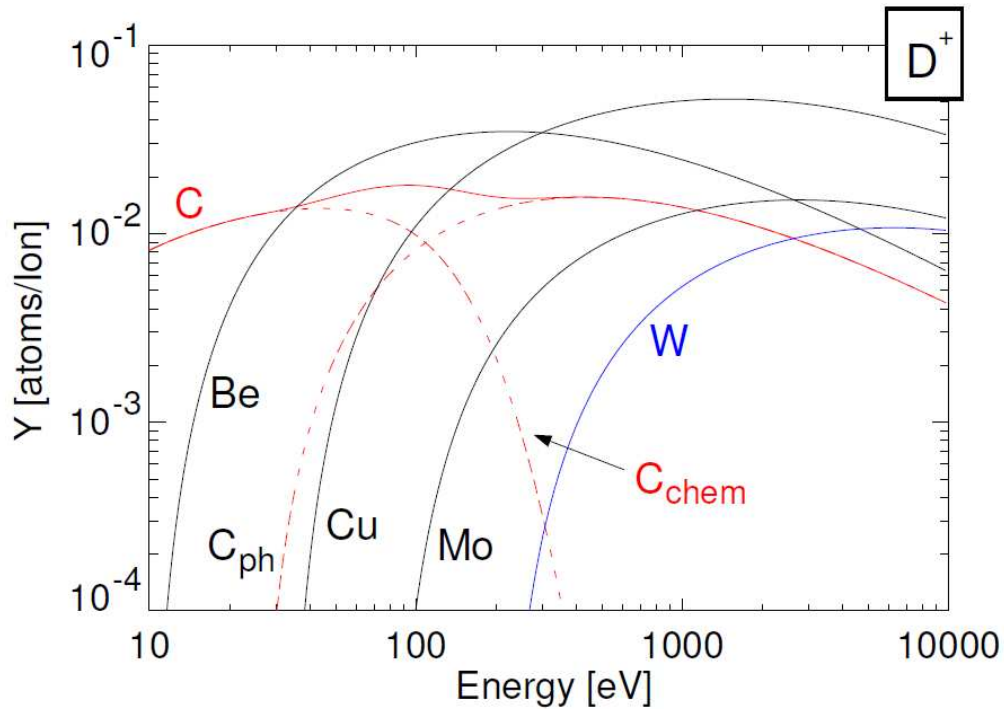


**Figure 1.8:** Sputtering yields for  $D^+$ -bombardment of several wall materials[1].

<sup>1</sup> A concentrated power load on the targets at the strikepoints can result in excessive material stresses.

of (High-Z) impurities is hence a necessity. This thesis shall contribute to provide such predictive capabilities by making the recently developed Trace-Ion Module (TIM) available to be used in the transport code EIRENE. The TIM enables the former transport code for neutrals to follow also the ion motion[6].

## 1.4 Scope of Thesis & Key Results & Structure

The presented thesis aims at the determination of tungsten transport as a trace impurity in the all-tungsten device ASDEX Upgrade. The new EIRENE 2010 version is prepared for standard use at IPP in the process. Lately the gyroaveraged, kinetic Monte-Carlo code EIRENE was enhanced by the introduction of a Trace-Ion Module (TIM), written by J. Seebacher. The TIM includes the  $\vec{E} \times \vec{B}$ -, curvature- and gradB drift effects as well as the mirror force and a Fokker-Planck collision operator in velocity space, accounting for thermal and frictional forces. The TIM basically simulates neoclassical banana transport. EIRENE is used in this thesis to simulate tungsten particles and evaluate the core penetration probability of tungsten released at different divertor target positions and at limiter positions in the main chamber. The core penetration probability is defined as the probability for a tungsten particle to cross the separatrix, thus entering the core plasma. The trace impurity approximation for tungsten as well as the gyro-averaged description of EIRENE are assumptions imposed on all presented simulations.

Key results of this thesis are a successful benchmark of the TIM transport against the well-established NEOART code[10], which calculates neoclassical transport coefficients. The benchmark showed that EIRENE simulations result in the right magnitude of fluxes expected from neoclassical banana transport. The applicability of the code and the trace and gyroaverage assumptions to the employed backgrounds are examined and are found to be respected for reliable simulation results. However some problems remain and have to be investigated in further. A particular problem of EIRENE was the thermalization of highly ionized tungsten, already reported for carbon under different circumstances by Seebacher[6]. The analysis of the penetration probability showed that divertor sources show considerable probabilities of around 1% above the strikepoint at the outer target. For L-Mode the penetration probability is largest at the upper boundary of the target and favorable with regard to the target temperature and deuterium influx profiles, while for H-Mode the regions of maximum target influx, temperature and core penetration profiles coincide. Limiter source showed in all cases extremely peaked penetration probability profiles at the HFS midplane and below. The maximum penetration probabilities for limiter sources were around 20%. Higher electron density reduced the penetration probabilities in L- and H-mode.

The thesis is divided into five chapters. The introduction give a short explanation of the key ingredients fusion, confinement and impurities in fusion plasmas. Then a number of theoretical models employed in EIRENE are presented in the second chapter. Source models, transport description of neoclassical theory and particle reactions are explained in more detail. The third chapter start with an overview of different numerical approaches to plasma simulations, like fluid and kinetic, and gives examples for present state-of-

the-art tools. Then the kinetic Monte-Carlo code EIRENE and its transport model, including the TIM, is detailed. Some important enhancements of the EIRENE code, such as an update of the sputter model and the implementation of a spatial diffusion routine, were done in the course of the work on this thesis and are presented afterwards. The setup preparations for the EIRENE simulations are explained before the last chapter gives detailed information about the validity of the EIRENE code for our purposes, a benchmark of the TIM transport against the NEOART code and finally the analysis of the simulations with respect to the core penetration probability. The thesis closes with a brief summary and an outlook.

# CHAPTER 2

---

## Prerequisites

---

Following this short introduction to the basic concepts and designs of nuclear fusion this chapter will present some theoretical prerequisites, which are necessary to understand the different models used in this thesis. The chapter also aims at providing an idea of the impact of assumptions or approximations by these models. The theoretical models are introduced following the history of a simulated particle. A particle is produced at a 'Source' (Sec. 2.1), then being subject to 'Transport' (Sec. 2.2) and finally undergoing 'Reactions' (Sec. 2.3) in the plasma terminating the particle trajectory eventually.

### 2.1 Sources

Excluding artificial impurities, like seeded Ar or N<sub>2</sub>, introduced by gas puffing, the main sources of plasma impurities are a variety of plasma-wall interactions such as sputtering or arc melting. In this thesis we investigate stationary fusion plasmas in an all-tungsten device without edge-localized modes (ELM). In this mode of operation, the dominant impurity source is sputtering by plasma particles, like Deuterium and, more important, impurities like C, N, O, Ar or W in ASDEX Upgrade[40; 42].

There are two major reasons to prefer divertor over limiter configuration. First, the restriction of substantial impurity production to a small and relatively cold interaction zone at the strike points – where plasma primarily hits the first wall – leads to reduced impurity production by sputtering. Second, impurities can be effectively retained in the divertor and do not affect the core plasma, because of large distances from the divertor plates to the main plasma along magnetic field lines. Recycling is also strongly reduced[31]. Hence the divertor configuration allows to gain control over important plasma parameters.

With the use of a divertor, impurities can be introduced intentionally, seeded, without damage to the plasma performance. A certain control over the species mix and the amount of impurities is possible. Apart from sputtering of the first wall material, gas puffing is the most important impurity source in most fusion plasmas. There are various reasons to introduce impurities artificially. Impurities can be used as a diagnostic tool (Li-beam[43]), to study the impurity transport with a well-defined source (laser blow-off[44] or modulated ion cyclotron heating [45]), to mitigate ELMs [46; 47] or to control

the power outflux distribution (radiating mantle[48]). Neither of these sources will be included in our simulations. Apart from seeded impurities there is a variety of plasma-processes that result in the release of impurities.

### 2.1.1 Sputtering & Self-Sputtering

Sputtering often is a main source for impurities in fusion plasmas. Sputtering occurs when plasma particles (ions or neutrals) hit plasma facing components, transferring momentum and energy onto the surface in the process and eventually releasing surface material particles. Three sputtering mechanisms can be distinguished. Physical sputtering with differing particle-projectile species is the most basic one. Chemical sputtering is in fact physical sputtering or thermal release of previously formed chemical compounds. Volatile or lightly bound chemical compounds can form due to the ion influx onto the surface – most important for hydrogen fluxes in carbon devices. Finally self-sputtering has to be mentioned. Self-sputtering is physical sputtering with identical particle-projectile species and exhibits some peculiarities physical sputtering does not.

Sputtering can take a pronounced importance amongst plasma-wall interactions in terms of impurity production – especially with tungsten. Therefore it is important to employ a most precise description of sputtering processes in the numerical models. Only an exact source definition can guarantee a reliable result for simulated impurity concentrations.

High-Z impurities, like tungsten, exhibit in general low sputtering yields for light projectiles, like hydrogen isotopes or carbon, due to a low energy transfer factor  $\gamma = \frac{4m_1m_2}{(m_1+m_2)^2}$  and high sputtering threshold energies  $E_{th}$ . The energy transfer factor is proportional to the transferred momentum of impinging particles of mass  $m_1$  on target material of mass  $m_2$ . In interplay with the surface binding energy, the energy transfer factor determines  $E_{th}$ . Below  $E_{th}$  no sputtering occurs. Despite low sputtering yields and high thresholds, self-sputtering can become an important issue for High-Z materials. Their matching mass ( $\gamma = 1$ ) and strong acceleration ( $\Delta E_{kin} \approx 2.8 \times k_b T_e Z_W$ ) of multiply ionized particles by the electric field in the Debye sheath can overcome both limiting effects. At low plasma temperatures in front of the surface (high) self-sputtering yields for High-Z first wall materials are counteracted by a process called prompt redeposition. The large gyro radii of High-Z particles, released as neutrals, imply ionization of the particles close enough to the surface to return to it during the first gyration. The particle then can be redeposited. However at plasma temperatures well above 70 eV in front of the surface this can also lead to runaway sputter cascades due to sheath acceleration. A more detailed description of prompt redeposition is given in Subsec. 3.3.1.2.

The investigated plasmas in this thesis are tokamak plasmas in the all-tungsten device ASDEX Upgrade. For tungsten chemical sputtering is not an issue although compound formation may lead to varying sputtering and material properties[49]. Physical sputtering is however the dominant sputtering process.

### 2.1.1.1 Physical Sputtering

To describe physical sputtering by particle bombardment a sputtering yield  $Y$  is introduced. It is defined as the number of particles released from the surface per incident particle.

$$Y = \frac{\text{\#sputtered atoms}}{\text{\#incident particles}} \quad (2.1)$$

Incident particles are assumed to be absorbed during the sputtering process and sputtered particles are always released as neutral atoms. The velocity distribution of sputtered particles is usually assumed to be a cosine distribution[50] with a Thompson energy distribution[51].

#### Sputter Model '93

A description of the sputtering yield is the revised Bohdansky formula improved by Eckstein. Eckstein replaced the Thomas-Fermi interaction potential in the original Bohdansky formula by the more appropriate Kr-C interaction potential, which gives a better description of the interaction on short distances[52; 53]. This substitution leads to an improvement in the description of the self-sputtering yield. The sputtering yield depends on incidence angle  $\vartheta$  and energy  $E_0$  of the projectile particle. Until now the angular dependence has not yet been implemented in EIRENE and a constant average angle was assumed for all cases.

The energy dependent sputtering yield for normal incidence ( $\vartheta = 0$ ) is given by

$$Y(E_0, \vartheta = 0) = q s_n^{KrC}(\epsilon_L) \left(1 - \left(\frac{E_{th}}{E_0}\right)^{2/3}\right) \left(1 - \frac{E_{th}}{E_0}\right)^2 \quad (2.2)$$

where  $s_n(\epsilon_L)$  is the stopping cross section based on the Kr-C potential and  $\epsilon_L$  is the reduced energy.  $E_{th}$  and  $q$  are used as fitting parameters.  $E_{th}$  gives the threshold for the onset of sputtering and  $q$  fits the profile to the absolute yield. A set of these parameters as well as algebraic approximations in case of missing experimental data are given in [52].

The Kr-C stopping cross section is given by

$$s_n^{KrC}(\epsilon_L) = \frac{0.5 \ln [1 + 1.2288 \epsilon_L]}{\omega(\epsilon_L)} \quad (2.3)$$

with  $\omega(\epsilon_L)$  being defined by

$$\omega(\epsilon_L) = \epsilon_L + 0.1728 \sqrt{\epsilon_L} + 0.008 \epsilon_L^{0.1504} \quad (2.4)$$

The reduced energy  $\epsilon_L$  is

$$\epsilon_L = E_0 \frac{M_2}{M_1 + M_2} \frac{a_L}{Z_1 Z_2 e^2} \quad (2.5)$$

where  $e$  is the electron charge,  $Z_1$  and  $Z_2$  are the nuclear charge numbers and  $M_1$  and  $M_2$  are the masses of the projectile and the target species respectively. The Lindhard

screening length  $a_L$  is given by

$$a_L = \left( \frac{9\pi^2}{128} \right)^{1/3} a_B \left( Z_1^{2/3} + Z_2^{2/3} \right)^{-1/2} = 0.4685 \left( Z_1^{2/3} + Z_2^{2/3} \right)^{-1/2} \quad (2.6)$$

where  $a_B$  is the Bohr radius.

Until now the presented equations were the basis of the physical sputter model included in EIRENE, which we refer to as 'Eckstein93'. The need to update this sputter model to the recent model 'Eckstein07' was felt, because of the impact tungsten sputtering can have on the impurity content of the simulated plasma.

### Sputter Model '07

This recent model was developed by Eckstein[54] based on more extensive and updated experimental data and state-of-the-art simulations with numerical tools like TRIM.SP [55]. Eckstein modified the revised Bohdansky formula and introduced two more fit parameters for the incident energy dependence. He also provided a more sophisticated model for the angular dependence of the sputtering yield. The model is governed by two equations. The first gives the sputter yield for normal incidence at different energies  $E_0$

$$Y(E_0, \vartheta = 0) = q s_n^{KrC} (\epsilon_L) \frac{\left( \frac{E_0}{E_{th}} - 1 \right)^\mu}{\frac{\lambda}{\omega(\epsilon)} + \left( \frac{E_0}{E_{th}} - 1 \right)^\mu} \quad (2.7)$$

The second formula gives a prefactor to describe the angular dependence

$$\frac{Y(E_0, \vartheta)}{Y(E_0, 0)} = \left( \cos \left[ \left( \frac{\vartheta_0 \pi}{\vartheta_0^* 2} \right)^c \right] \right)^{-f} \exp \left[ b \left( 1 - \frac{1}{\cos \left[ \left( \frac{\vartheta_0 \pi}{\vartheta_0^* 2} \right)^c \right]} \right) \right] \quad (2.8)$$

$\mu$ ,  $\lambda$ ,  $c$ ,  $f$  and  $b$  are additional fitting parameters and  $\vartheta$  is the incident angle enclosed between the velocity vector of the incident particle and the surface normal (angle  $\beta$  in Fig. 3.1). The parameter  $\lambda$  triggers the onset of the decrease of the sputtering yield at energies towards the threshold and  $\mu$  describes the strength of this decrease. The parameters  $c, f$  and  $t$  are not accessible to a comparable direct interpretation.  $\vartheta_0^*$  is a prefactor to prevent an incident angle of  $\pi/2$  in self-sputtering processes. This must be excluded to account for the interaction of the incident particle with the surface atoms parameterized by the binding energy  $E_{sp}$  and resulting in decreased angles

$$\vartheta_0^* = \pi - \arccos \left[ \sqrt{\frac{1}{1 + E_0/E_{sp}}} \right] \geq \frac{\pi}{2} \quad (2.9)$$

All fit parameters were obtained by Bayesian statistics on either experimental or numerical results[54].

EIRENE now uses the Eckstein07 sputter model whenever the parameters are available and falls back to Eckstein93 if not. The same is true for angular dependence inclusion. The angular correction factor is energy dependent and the according fit parameters vary for different energies  $E_0$ . In the present work this is accounted for by taking the fit parameters closest in energy space as parameter values for the calculations.

## 2.1.1.2 Chemical Sputtering

Chemical sputtering is not an issue for a tungsten first wall such as in AUG. Nevertheless carbon, as an impurity, is still present in today's experiments at AUG. First wall materials like carbon exhibit an additional impurity source. The formation of volatile molecules and loosely bound compounds, which exhibits enhanced desorption and sputtering, is called chemical sputtering.

Only a short introduction of EIRENE's theoretical model introduced by Roth and Pacher at the PSI 1998 is given [56; 57]. Roth distinguishes three different kinds of processes contributing to chemical sputtering with respect to the cause of impurity release. First is thermal release of hydrocarbons ( $C_xH_y$ ) above temperatures of about 400 K. Hydrocarbons form at these temperatures due to the hydrogenation of carbon atoms by thermalized hydrogen ions. Above 600 K the amount of released hydrocarbons reduces and recombined hydrogen molecules ( $H_2$ ) are primarily released. The second process leading to an enhanced thermal release of carbon derivatives is radiation damage in the material by kinetic energy, transferred from impinging ions to surface atoms. The generated defects provide free electrons for hydrogenation. Below an energy threshold  $E_{dam}$  no such enhancement occurs. For low surface temperatures almost no hydrocarbons are thermally released. Hydrogenation then leads to the formation of a hydrated surface layer. The hydrocarbon radicals forming this layer have much lower surface binding energies (1 eV) than carbon in regular lattice configuration (7.4 eV). Yet again this leads to increased sputtering and impurity release.

The total chemical sputtering yield is thus constituted of these three individual processes, each dominant for a certain temperature regime.

$$Y_{tot} = Y_{th} + DY_{th} + Y_{surf} \quad (2.10)$$

The thermal erosion yield  $Y_{th}$  is given by

$$Y_{th} = c^{sp^3} \frac{0.033 \times \exp \left[ -\frac{E_{th}}{k_b T} \right]}{2 \times 10^{-32} \Phi + \exp \left[ -\frac{E_{th}}{k_b T} \right]} \quad (2.11)$$

where  $\Phi$  is the ion influx on the surface and  $c^{sp^3}$  is defined by

$$c^{sp^3} = C \frac{\left( 2 \times 10^{-32} \Phi + \exp \left[ -\frac{E_{th}}{k_b T} \right] \right)}{2 \times 10^{-32} \Phi + \left( 1 + \frac{2 \times 10^{-29}}{\Phi} \exp \left[ -\frac{E_{th}}{k_b T} \right] \right) \exp \left[ -\frac{E_{th}}{k_b T} \right]} \quad (2.12)$$

Here  $C$  is a temperature or flux dependent constant [56]. Radiation damage  $Y_{dam}$  enhances the thermal chemical sputtering accounting for reduced binding energies due to structural damage in the surface and bond breaking. The constant  $D$  determines the weight of this effect. Lastly the surface erosion yield  $Y_{surf}$  accounts for the loosely bound hydrocarbon radicals (mainly  $-CH_3$ ) forming a layer on the actual graphite structure especially at low temperatures. The formation of this so called ion induced desorption layer is described by  $Y_{des}$ .

$$Y_{surf} = c^{sp^3} \frac{Y_{des}(E_0)}{1 + \exp \left[ \frac{E_0 - 65 \text{ eV}}{40} \right]} \quad (2.13)$$



The radiation damage yield  $Y_{dam}$  and the desorption yield  $Y_{des}$  both take the same form as the physical sputtering yield of the 1993 model by Eckstein in Eq. (2.2). The parameters  $E_{dam}$  or  $E_{des}$  are substituted for  $E_{th}$  respectively. Typical values for the chemical sputtering parameters for hydrogen are  $E_{dam} = 15$  eV,  $E_{des} = 2$  eV,  $D = 250$  and a gaussian distribution of activation energies  $E_{th}$  centered at  $m = 1.7$  eV with  $\sigma = 0.3$  eV.

### 2.1.1.3 Prompt Redeposition

Prompt redeposition is a phenomenon which can have an impact on the effective sputtering yield. It calls for the introduction of two quantities called net and gross sputtering yield. The net sputtering yield takes into account all redeposition effects. The gross sputtering yield is simply the sputtering yield directly derived from the sputter model. Prompt redeposition is important mainly for HighZ impurities. The gyroradius  $\varrho$  then can approach the mean ionization length  $\lambda$  of the sputtered atom. An ionization event can thus lead to redeposition on the surface during the first gyration.

$$\varrho = \frac{v_{\perp}}{\omega_c} \quad \& \quad \lambda = \frac{v}{n_e \langle \sigma v \rangle} \quad (2.14)$$

where  $\varrho$  is the gyroradius,  $\omega_c$  is the cyclotron frequency,  $\sigma$  is the cross-section for the first ionization and  $v$  is the particle velocity. Typical values of the gyroradii of singly ionized tungsten and carbon are  $\varrho_{W+} = 5.1$  mm and  $\varrho_{C+} = 1.3$  mm with  $B = 1$  T and  $E_{kin} = 10$  eV, while the mean ionization length is in the  $10 \mu\text{m}$  range for tungsten (c.f. Fig. A.9). Prompt redeposition can reduce the sputtering yield significantly, especially at high electron densities in front of the surface – another advantage of the divertor configuration with larger electron densities in front of the target. Tungsten self-sputtering is strongly reduced by prompt redeposition at edge temperatures below 70 eV and electron densities approaching  $5 \times 10^{19} \text{ m}^{-3}$ . The difference between the gross sputtering yield without prompt redeposition and the net sputtering yield, shown in Fig. 2.2, shows the importance of prompt redeposition. The necessity to include its effects into the code to obtain valuable net erosion fluxes when dealing with tungsten is thus evident. The prompt redeposition mechanism can – if studied in more detail as in [49] – lead to tungsten migration and pattern formations on the in-vessel components like the divertor tiles. A model to treat prompt redeposition in a simple geometrical approach is developed in [58]. The decisive parameter for a redeposition process is the ration  $p$  of mean free path to first ionization  $\lambda$  and gyroradius  $\varrho$ .

$$p = \frac{\lambda}{\varrho} = \frac{qB}{mS n_e} \quad (2.15)$$

$q$  being the electric charge,  $B$  the absolute value of the magnetic field,  $m$  the particle mass,  $n_e$  the electron density and  $S$  the rate coefficient for ionization. Assume a surface

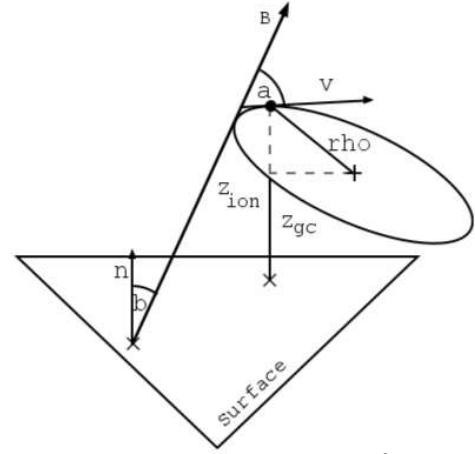


**Figure 2.1:** First gyration of a recently ionized particle after being released at the surface.

in the xy-plane with the normal pointing along the positive z-direction  $\vec{n}_s = \vec{e}_z$  and a magnetic field parallel to the surface, directed along the positive y-direction  $\vec{b} = \vec{e}_y$ . The approximation of a magnetic field parallel to the surface is legitimate as the magnetic field usually hits the vessel surfaces purposely at oblique angles to distribute heat load over a wider area. The geometrical errors of the model remain small. On average a sputtered neutral atom is ionized after traveling the mean free path. The ionized particle experiences the Lorentz force and gyrates on the gyro circle. The gyration might eventually transport the particle back to the surface and lead to its redeposition. A detailed geometrical analysis assuming a cosine velocity distribution of sputtered atoms gives a redeposited fraction  $r$  of sputtered particles.

$$r = \frac{1}{1 + p^2} \quad (2.16)$$

The above analysis, however, was carried out for a fixed ionization length. Accounting for the actual exponential distribution of the ionization length with mean  $\lambda$  one has to average over this distribution to get the effectively redeposited fraction.

$$\langle r \rangle = \frac{1}{p} \int_0^\infty \exp\left(-\frac{x}{p}\right) r(x) dx = \frac{1}{p} \int_0^\infty \exp\left(-\frac{x}{p}\right) \frac{1}{1 + x^2} dx \quad (2.17)$$

with a normalization factor  $1/p$ .

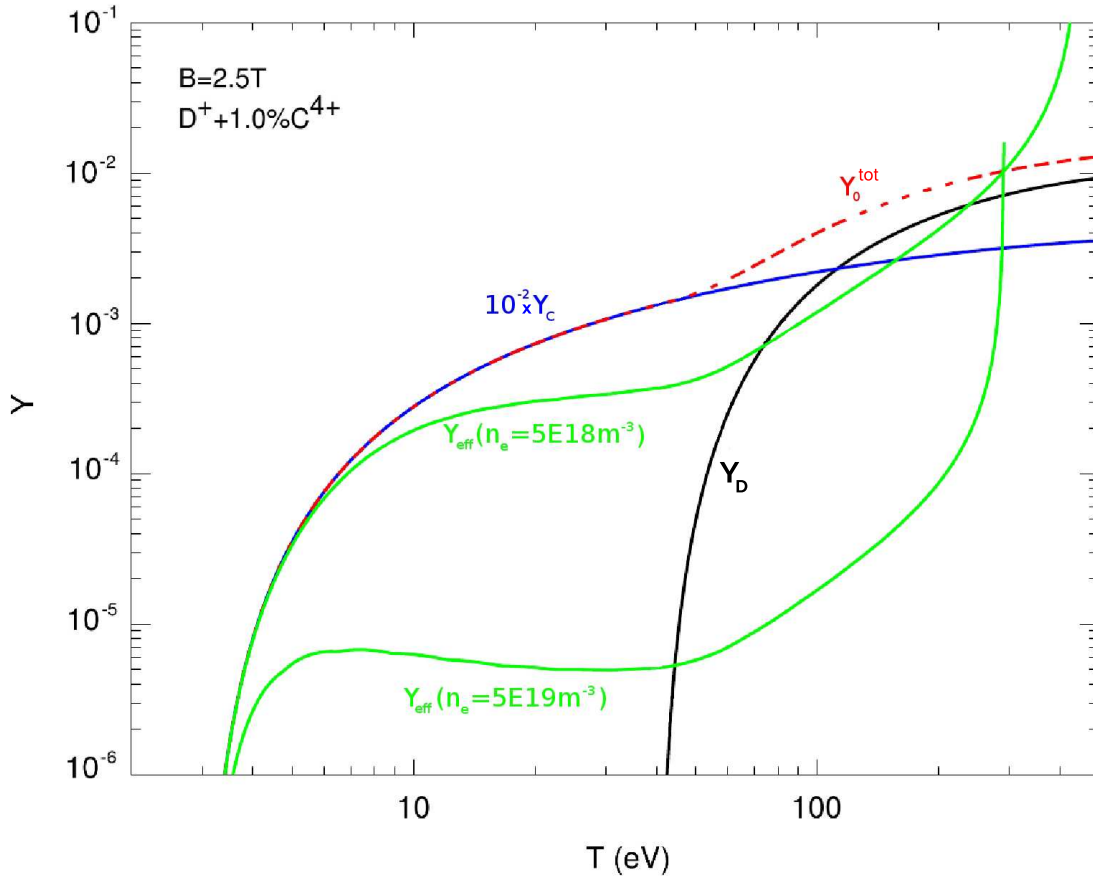


**Figure 2.2:** Sputter yield of tungsten for different projectile ensembles with and without prompt redeposition.[58]

For ionization lengths considerably larger than the Debye sheath width a redeposited particle will hit the surface with the initial kinetic energy plus the energy due to the sheath acceleration. Sputtering by the redeposited particle is possible. This implies a recursive sputter chain leading to a net sputter yield  $Y_{eff}$ .

$$Y_{eff} = \frac{1 - \langle r \rangle}{1 - \langle r \rangle Y_W} \sum_i f_i Y_i \quad (2.18)$$

where  $Y_W$  is the tungsten self-sputtering yield,  $Y_i$  is the tungsten sputtering yield by incident particles of species  $i$  and  $f_i$  is the fractional abundances of the incident particle fluxes of species  $i$ . For  $\langle r \rangle = 1$  the effective sputter yield is zero as all sputtered particles are redeposited afterwards. With  $Y_W \geq 1$  for  $E_{kin}^W \geq 1$  keV the energy gain due to sheath acceleration of  $\approx 3k_b T_e$  leads to a runaway sputter cascade for edge temperatures above 300 eV. Nevertheless the net erosion is largely reduced by prompt redeposition at electron densities above  $5 \times 10^{19} \text{ m}^{-3}$ , when  $\lambda$  becomes comparable to  $\varrho$ . Figure 2.2 shows the effect of the analytical model on the effective sputtering yield in a plasma constituted by  $D^+$  and 1%  $C^{4+}$  respecting  $T_e = T_i = T$  and  $E_{kin} \approx 2k_b T_i + 3k_b T_e$  [30]. To account for the major modification of the sputtering yield by prompt redeposition a prompt redeposition routine was implemented in EIRENE. There is a multitude of further impurity sources, we can not describe in detail, including arc-melting, evaporation and dust.

## 2.2 Transport

Transport of any kind of quantity, may it be particles, energy or heat, is the most prominent feature determining plasma characteristics. In the early days of fusion science it was a common belief, based on classical transport, that table top sized fusion devices could be build and operated successfully. If not for the occurrence of neoclassical and anomalous transport phenomena this would have been feasible. There is a number of extensive introductory textbooks for neoclassical plasma transport theory such as [1; 60; 61].

Even after extensive development of neoclassical theory, the transport observed in experiments could not be properly described. An anomalous transport, not yet understood, was needed to account for the missing theoretical transport. Today it is commonly believed that anomalous transport is of turbulent nature and driven by fluctuating electric potentials,  $\vec{E} \times \vec{B}$ -flows and vorticity in the edge[2]. A summary on transport in tokamaks can be found in [33].

This section sketches the derivation of classical and neoclassical transport. Only minor remarks regarding anomalous transport are made, because there is no first-principle theory on turbulent transport in fusion plasmas yet. EIRENE is anyhow not considering any kind of anomalous transport. The framework of neoclassical transport is explained in greater detail, because the recently included Trace-Ion Module (TIM) of EIRENE is considering neoclassical transport effects, namely the banana regime transport. EIRENE employs only neoclassical theory for ion tracing so far and thus is especially interesting in the Edge Transport Barrier (ETB), where flux surfaces are still closed and anomalous transport is largely reduced.

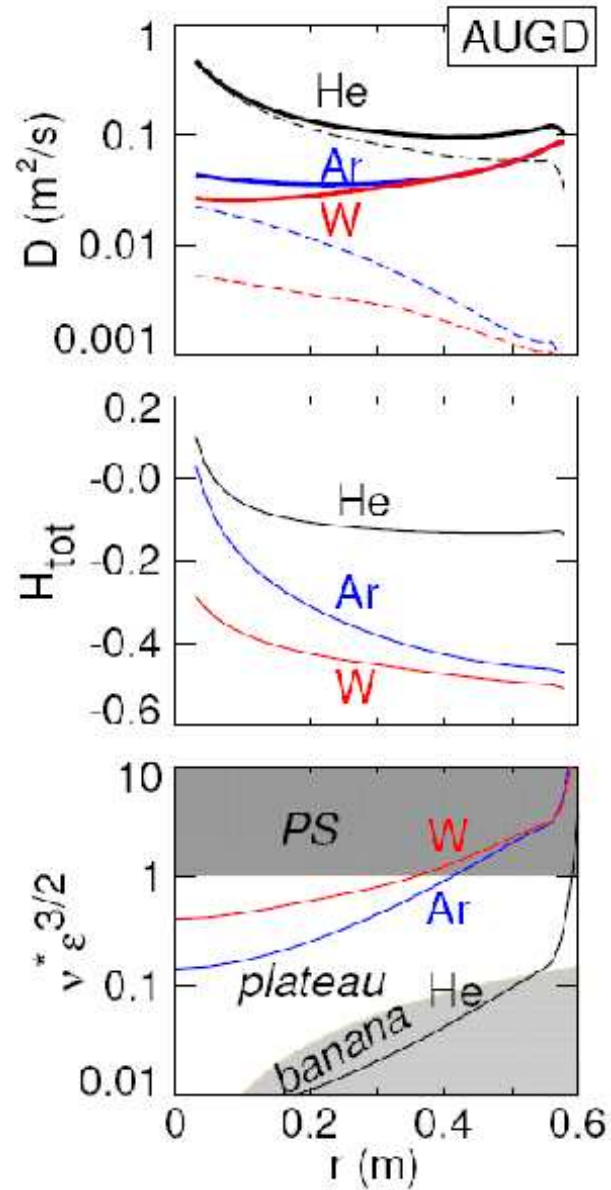


**Figure 2.3:** Transport regimes and coefficients for different impurities at ASDEX Upgrade at  $n_e = 10^{20} \text{ m}^{-3}$ ,  $T_e = 2.5 \text{ keV}$ ,  $q_{95} = 3.3$  and  $B_t = 2.5 \text{ T}$ [59].

### 2.2.1 Classical Transport

The object of all kinetic calculations in plasma transport studies is the determination of the one-particle distribution function  $f_a(\vec{x}, \vec{v}, t)$  for particles of species  $a$  or at least its moments. The one-particle distribution function describes the microscopic state of the examined system in statistical terms. The probability to find a particle of species  $a$  at time  $t$  in an infinitesimal volume  $d^3x$  at  $\vec{x}$  with a velocity in the volume  $d^3v$  around  $\vec{v}$  is given by  $f_a(\vec{x}, \vec{v}, t) d^3x d^3v$ . The moments of the particle distribution function allow to quantify the transport in a given system and compare them to experimental or fluid model results. The particle distribution function is normalized such that

$$\int f_a(\vec{x}, \vec{v}, t) d^3x d^3v = 1 \quad \forall t > 0 \quad (2.19)$$

The kinetic equation governs the evolution of the distribution function  $f_a$  in time. The external electromagnetic fields  $\vec{E}$  and  $\vec{B}$  impose forces on charged particles with the nuclear charge number  $Z_a$  and mass  $m_a$ .

$$\partial_t f_a + \vec{v} \cdot \nabla_{\vec{x}} f_a + \frac{Z_a e}{m_a} (\vec{E} + \vec{v} \times \vec{B}) \cdot \nabla_{\vec{v}} f_a = \sum_b C_{ab}(f_a, f_b) \quad (2.20)$$

where the notation  $\partial_t \equiv \frac{\partial}{\partial t}$  is introduced and  $\nabla_i$  with  $i = \{\vec{x}, \vec{v}\}$  operates on space or velocity coordinates respectively. The Coulomb interaction between plasma particles acting in velocity space is represented by the Fokker-Planck collision operator  $C_{ab}$  on the right-hand side of Eq. (2.20)[9].

$$C_{ab}(f_a, f_b) = - \sum_i \frac{\partial}{\partial v_{ai}} (K_i^{ab} f_a) + \frac{1}{2} \sum_{i,k} \frac{\partial^2}{\partial v_{ai} \partial v_{ak}} (D_{ik}^{ab} f_a) \quad (2.21)$$

For the sake of a simplified notation the dependence of  $C_{ab}$  on  $f_a$  and  $f_b$  is henceforth not explicitly denoted. The Coulomb interaction has some desirable properties, which facilitate the calculations. These are:

1. Positivity of the distribution function:

$$f_\alpha \geq 0 \text{ for } t = 0 \implies f_\alpha \geq 0 \text{ for } t > 0 \quad (2.22)$$

2. Particle conservation:

$$\int C_{ab} d^3v = 0 \quad (2.23)$$

3. Momentum conservation:

$$\sum_{a,b} \int m_a \vec{v} C_{ab} d^3v = 0 \quad (2.24)$$

4. Energy conservation:

$$\sum_{a,b} \int m_a v^2 C_{ab} d^3v = 0 \quad (2.25)$$

Additionally the H-Theorem applies. These properties finally entail the fluid balance Eqs. (2.31-2.32) below.

Averaging powers of the velocity  $\vec{v}$  over the distribution function gives the moments of the distribution function. These moments can be identified by characteristic fluid properties. From now on the dependence of  $f_a$  on  $\vec{x}$ ,  $\vec{v}$  and  $t$  will be omitted.

The particle density  $n_a$ :

$$n_a = \int f_a d^3v \quad (2.26)$$

The fluid/drift velocity  $\vec{u}_a$ :

$$\vec{u}_a = \frac{1}{n_a} \int \vec{v} f_a d^3v \quad (2.27)$$

The pressure  $p_a$  and the viscosity tensor  $\overleftrightarrow{P}_{i_a}$ :

$$p_a = \frac{m_a}{3} \text{Tr} \left[ \int |\vec{v} - \vec{u}_a|^2 f_a d^3v \right] \quad (2.28)$$

$$\overleftrightarrow{H}_a = m_a \int (\vec{v} - \vec{u}_a) \otimes (\vec{v} - \vec{u}_a) f_a d^3v - p_a \overleftrightarrow{I} \quad (2.29)$$

And the heat flux  $q_a$ :

$$q_a = \frac{m_a}{2} \int |\vec{v} - \vec{u}_a|^2 (\vec{v} - \vec{u}_a) f_a d^3v \quad (2.30)$$

Multiplying the kinetic equation of motion, Eq. (2.20), with powers  $k$  of the velocity  $\vec{v}$  and integrating over the velocity phase space, respecting the properties (2.23-2.25), we arrive at the fluid equations. Each fluid equation of order  $k$  includes moments of higher orders  $(k+1, \dots)$ . In order to get a complete set of equations it has to be closed by approximating higher moments. For the classical radial transport the first two moment equations are taken into account.

$$\frac{\partial n_a}{\partial t} + \nabla \cdot (n_a \vec{u}_a) = 0 \quad (2.31)$$

$$m_a n_a \left[ \frac{\partial u_a}{\partial t} + (\vec{u}_a \cdot \nabla) \vec{u}_a \right] = q_a n_a (\vec{E} + \vec{u}_a \times \vec{B}) - \nabla p_a - \nabla \cdot \overleftrightarrow{H}_a + \sum_{b \neq a} \vec{F}_{ab} \quad (2.32)$$

where  $\vec{F}_{ab}$  is the friction force exerted on particles of type  $a$  by particles of type  $b$ . The average friction force density can be described using a potential function  $h$  accounting for the velocity distribution of species  $b$  by [1; 59]

$$\vec{F}_{ab} = -A_{ab} \int f_a \nabla_v h(\vec{v}) d^3v \quad \& \quad h(\vec{v}) = \int \frac{1}{|\vec{v} - \vec{v}_b|} f_b(\vec{v}_b) d^3v_b \quad (2.33)$$

The fluid equations are closed with the assumption of a divergence-free viscosity and a small mean velocity  $u_a$  of the Maxwellian distributed particle velocities with respect to thermal velocity  $v_{th}$ .

$$\nabla \cdot \vec{\Pi}_a = 0 \quad \& \quad u_a \ll v_{th} = \sqrt{2k_B T/m} \quad (2.34)$$

The later assumption implies the expansion of the Maxwellian exponential around  $\vec{v} - \vec{u}_a$  to the linear first order leading to a friction force of

$$\vec{F}_{ab} = m_a n_a \nu_{ab} (\vec{u}_b - \vec{u}_a) \quad (2.35)$$

with the collision frequency  $\nu_{ab}$  for  $T_a = T_b$

$$\nu_{ab} = \frac{4\sqrt{2\pi}}{3(4\pi\epsilon_0)^2} q_a^2 q_b^2 n_b \sqrt{\frac{m_{ab} \ln \Lambda_{ab}}{(k_B T)^3}} \quad (2.36)$$

where  $m_{ab}$  is the reduced mass and the Coulomb logarithm  $\ln \Lambda_{ab} = \ln [b_{min}/b_{max}]$  is given by the maximum/minimum impact parameters  $b_{max/min}$ . A common approach is to identify the impact parameters with the Debye shielding length  $\lambda_D$  and the  $\pi/2$  deflection impact parameter respectively.

$$b_{min} = \lambda_D = \sqrt{\frac{\epsilon_0 k_B T}{n_e e^2}} \quad \& \quad b_{max} = r_0 = \frac{q_a q_b}{12\pi\epsilon k_B T} \quad (2.37)$$

In order to further facilitate the calculations, a stationary, magnetized plasma close to thermal equilibrium is assumed. The following ordering applies

$$\delta_1 = \frac{\nu_a}{\omega_a} \ll 1 \quad \& \quad \delta_2 = \frac{r_{g,a}}{L_{n/T}} \ll 1 \quad (2.38)$$

and the fluid velocity is expanded with respect to the small parameters  $\delta_{1/2}$

$$\vec{u}_a = \vec{u}_a^{(0)} + \vec{u}_a^{(1)} \quad (2.39)$$

The stationary first order momentum balance equation includes no friction force as the friction term is of order  $\delta^2$ . We get

$$\vec{u}_a^{(0)} \times \vec{B} = -\vec{E} + \frac{\nabla p_a}{q_a n_a} \quad (2.40)$$

The second order equation reads

$$\vec{u}_a^{(1)} \times \vec{B} = -\frac{m_a}{q_a} \sum_{b \neq a} \nu_{ab} (\vec{u}_b^{(0)} - \vec{u}_a^{(0)}) \quad (2.41)$$

Cross product with  $\vec{B}$  yields

$$\vec{u}_{a,\perp}^{(0)} = \frac{\vec{E} \times \vec{B}}{B^2} - \frac{\nabla p_a \times \vec{B}}{q_a n_a B^2} \quad (2.42)$$

When Eq. (2.42) is substituted into Eq. (2.41) the  $\vec{E} \times \vec{B}$  terms cancel and the cross product with  $\vec{B}$  yields

$$\vec{u}_{a,\perp}^{(1)} = \frac{m_a}{q_a B^2} \sum_{b \neq a} \nu_{ab} \left( \frac{\nabla p_b}{q_b n_b} - \frac{\nabla p_a}{q_a n_a} \right) \quad (2.43)$$

The zeroth order fluid velocity includes the  $\vec{E} \times \vec{B}$ -drift perpendicular to the electric and magnetic field and the diamagnetic drift perpendicular to the pressure gradient and the magnetic field. Note that the subscript  $\perp$  means perpendicular to the magnetic field line and not necessarily the flux surface as opposed to the radial direction. In the current approach radial particle transport is driven only by pressure gradients. Associated to the obtained fluid velocities are corresponding currents carried by the charged particles

$$\vec{j}_{\perp}^{(0)} = \sum_a q_a n_a \vec{u}_{a,\perp}^{(0)} = -\frac{\nabla p \times \vec{B}}{B^2} \Leftrightarrow \nabla p_{\perp} = \vec{j}^{(0)} \times \vec{B} \quad (2.44)$$

$$\vec{j}^{(1)} = \sum_a q_a n_a \vec{u}_{a,\perp}^{(1)} = 0 \quad (2.45)$$

The magnetohydrodynamics (MHD) equilibrium condition is thus satisfied for the lowest order currents. The first order current is ambipolar as would be expected.

Using the gaseous state equation  $p = nk_B T$  the first order velocity (c.f. Eq. (2.43)) leads to the classical particle flux  $\vec{\Gamma}_a$

$$\vec{\Gamma}_a = D_{CL}^a \left[ -\nabla n_a + n_a q_{ab} \left( L_n^b + L_T (1 - q_{ba}) \right) \right] \quad (2.46)$$

with  $q_{ab} = q_a/q_b$  being the charge ratio,  $D_{CL}$  the classical diffusion coefficient,  $L_n = \frac{n}{\nabla n}$  and  $L_T = \frac{T}{\nabla T}$  the pressure and temperature gradient length respectively. Equation (2.46) has the form of a diffusive and convective ansatz

$$\vec{\Gamma} = -D \nabla n + \vec{v} n \quad (2.47)$$

with diffusion coefficient

$$D_{CL}^a = \frac{m_a k_B T}{q_a^2 B^2} \sum_{b \neq a} \nu_{ab} = \frac{r_{g,a}^2}{2} \nu_a \quad (2.48)$$

and drift velocity

$$\vec{v}_{CL}^a = D_{CL}^a q_{ab} \left( L_n^b + L_T (1 - q_{ba}) \right) \quad (2.49)$$

where  $\nu_{ab}$  is the collision frequency of particles of species  $a$  with particles of species  $b$  (c.f. Eq. (2.36)). A more sophisticated expansion of the perturbed Maxwellian takes the gradients of  $n$  and  $T$  on the scale of the gyroradius into account ( $f \approx f_0 + \frac{\partial f}{\partial x}|_{x=0} r_g$ ). The following result is obtained[59]:

$$\vec{F}_{ab,\perp} = -m_a n_a \nu_{ab} \left( \frac{\nabla p_b}{q_b n_b} - \frac{\nabla p_a}{q_a n_a} - \frac{3}{2} k_b \nabla T \left( \frac{m_{ab}}{q_b m_b} - \frac{m_{ab}}{q_a m_a} \right) \right) \times \frac{\vec{B}}{B^2} \quad (2.50)$$



The first two terms are again the friction force due to pressure gradients, while the last term is known as thermal force. The final flux then is

$$\vec{\Gamma}_{CL}^a = -D_{CL}^a \nabla n_a + D_{CL}^a \sum_{b \neq a} q_{ab} \left( L_n^b - L_T \left[ \frac{3}{2} \frac{m_{ab}}{m_b} - 1 - q_{ba} \left( \frac{3m_{ab}}{2m_a} - 1 \right) \right] \right) n_a \quad (2.51)$$

Equation (2.51) simplifies for heavy impurities with nuclear charge  $Z$  in pure hydrogen plasmas  $H$ , where electron-ion collision can be neglected

$$\vec{\Gamma}_{CL}^Z = \frac{r_{g,Z} \nu_{Z,H}}{2} \left( -\nabla n_Z + n_Z q_Z \left( \underbrace{L_n^H}_{\text{inward}} - \underbrace{\frac{1}{2} L_T}_{\text{outward}} \right) \right) \quad (2.52)$$

The density gradient length of hydrogen leads to an inward flux of impurities, counteracted by the so-called temperature screening, which is driven by the impurity temperature gradient length. The temperature screening is the reason why central ion heating is applied. Steeper ion temperature gradients in the core avoid impurity accumulation in the plasma center. The classical flux, given in Eq. (2.52), leads to an undesired peaking of the impurity equilibrium profile.

$$\frac{n_Z(r)}{n_Z(0)} = \left( \frac{n_H(r)}{n_H(0)} \right)^Z \left( \frac{T(r)}{T(0)} \right)^{-Z/2} \quad (2.53)$$

## 2.2.2 Neoclassical Transport

In contrast to classical transport with a constant and straight magnetic field, torus symmetry is assumed for neoclassical transport. The term 'neoclassical' summarizes all effects stemming from the toroidal geometry. The bending of the straight cylinder geometry into a torus leads to an inverse dependence of the toroidal magnetic field on the major radius  $R$ . Neoclassical transport coefficients resemble closely the classical results – exhibiting a diffusive and convective term. Neoclassical diffusion coefficients are enhanced by a geometrical factor and the transport includes additional effects like mirror forces, curvature and  $\nabla B$  drifts. The neoclassical drift coefficient terms also cause temperature screening as well as inward drifts due to density gradients growing with  $Z$ . Figure 2.4 shows the toroidal geometry with characteristics of the magnetic field in an appropriate set of coordinates. The cause of classical transport – apart from drifts – are perpendicular friction forces. In contrast neoclassical fluxes are either driven by parallel friction (Pfisch-Schlüter) or by bouncing in trapped particle orbits (Banana). Due to the neoclassical average on closed flux surfaces a coupling of perpendicular and parallel velocities occurs and their evolution can no longer be treated independently (c.f Subsec. 2.2.2.2). The necessary average limits the validity of neoclassical theory to core plasma regions, where magnetic flux surfaces are closed. Additional effects in neoclassical theory are linked to trapped particles, for example the bootstrap current and the Ware pinch[62; 63]. Some important quantities routinely used in neoclassical calculations are presented in the following list:

- Minor radius  $r_0 = a$  (in Fig. 2.4)

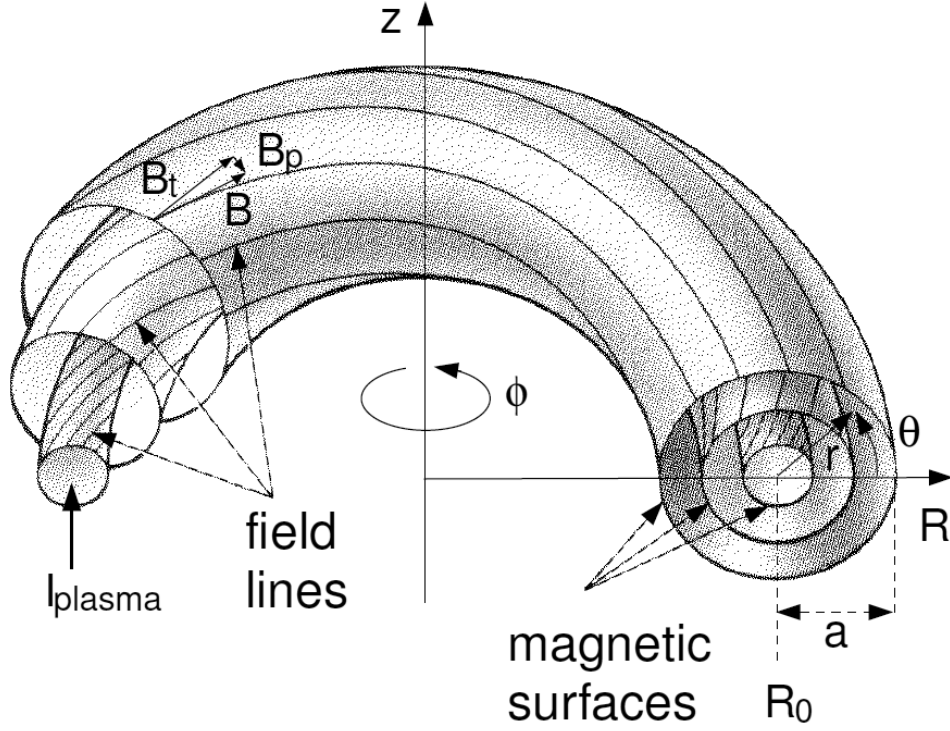


**Figure 2.4:** Magnetic field structure in tokamak configuration with nested flux surfaces and helical field lines. Pitch angle is largely exaggerated[62, p.25].

- Major radius  $R_0$
- Toroidal and poloidal magnetic field  $B_t, B_p$
- Inverse aspect ration  $\varepsilon$  -  $\varepsilon = \frac{r_0}{R_0}$
- Safety factor  $q$  -  $q = \frac{\text{\#Toroidal turns}}{\text{\#Poloidal turns}} \approx \frac{rB_t}{RB_p}$ , for  $\varepsilon \ll 1$
- Poloidal (Toroidal) flux density  $\Psi(\phi)$  - In a tokamak  $|\nabla\Psi| = RB_p$
- Total collision frequency  $\nu_a$  for species  $a$  -  $\nu_a = \sum_{b \neq a} \nu_{ab}$
- Core Collisionality  $\nu_a^* - \nu_a^* = \frac{\nu_a}{\nu_B \varepsilon}$
- Transit frequency  $\nu_T - \nu_T = \frac{v_a}{qR_0}$
- Bounce frequency  $\nu_B - \nu_B = \nu_T \sqrt{\varepsilon}$

In the preceding list the safety factor is the ratio of toroidal turns around the torus and poloidal turns around the magnetic axis necessary to close the field line back on itself. The safety factor is also a measure of the ratio of the toroidal and poloidal magnetic field. The transit frequency gives the inverse time a charged particle needs to make a full pass around the torus on a magnetic field line, the bounce frequency is the inverse time a trapped particle needs to complete a full banana orbit (c.f. Subsec. 2.2.2.3) and

the collisionality is a measure of the fraction of a banana orbit, which a particle can complete before collisions interrupt its trajectory.

A magnetic flux surface is characterized by  $\Psi = \text{const.}$  Density and temperature on a flux surface are nearly constant, because the parallel transport is much faster than the perpendicular transport. Gradients on the flux surfaces are counteracted and smoothed out by parallel fluxes and can be neglected in a first approach. Hence averaging over the flux surface reduces the transport problem to one, radial dimension. The flux surface average of an arbitrary scalar quantity  $Q$  is given by[59]

$$\langle Q \rangle = \frac{1}{\Delta V} \int_{\Delta V} Q dV = \left( \frac{\partial V}{\partial \Psi} \right)^{-1} \int_{\partial V} \frac{G}{|\nabla \Psi|} dS \quad \& \quad \int Q dV = \int_0^\Psi \frac{\partial V}{\partial \Psi} \langle Q \rangle d\Psi \quad (2.54)$$

where  $S$  is the surface and  $\Psi$  is the poloidal flux density. Flux surface averaged quantities are commonly given in various normalized flux surface coordinates  $\varrho_i$ . Examples for flux surface coordinates are the poloidal ( $\Psi$ ) and toroidal ( $\phi$ ) flux and flux surface volume ( $V$ ) coordinates:

$$\varrho_{pol} = \sqrt{\frac{\Psi(\vec{r}) - \Psi_{Ax}}{\Psi_{Sep} - \Psi_{Ax}}}, \quad \varrho_{tor} = \sqrt{\frac{\phi(\vec{r}) - \phi_{Ax}}{\phi_{Sep} - \phi_{Ax}}}, \quad \varrho_{Vol} = \sqrt{\frac{V(\vec{r}) - V_{Ax}}{V_{Sep} - V_{Ax}}} \quad (2.55)$$

where the subscripts  $Sep$  and  $Ax$  indicate the value of the quantity taken at the separatrix and the magnetic axis respectively. The above flux surface coordinates are explained in more detail in [64]. In the following calculations the NEOART flux label  $r$  is used[10].  $r$  is defined by the radius of a cylinder with a volume equal to the enclosed volume of a flux surface  $\Psi$ .

$$r = \sqrt{\frac{V_\Psi}{2\pi^2 R}} \quad (2.56)$$

In neoclassical transport theory three collisionality regimes are distinguished. Each shows different transport properties and relies on different mechanisms driving it. After giving the neoclassical correction for classical transport coefficients, the different neoclassical regimes are introduced and the transport mechanisms are explained shortly. Table 2.1 gives the validity regions and the necessary scale ordering of the neoclassical regimes.

Regime	Mean free path	Scale ordering	Validity
Banana	long	$\lambda_D \ll \varrho \ll L_H < \lambda_{MFP}$	$\nu_a^* \ll 1$
Plateau	intermediate	$\lambda_D \ll \varrho \ll \lambda_{MFP} \lesssim L_H$	$1 < \nu_a^* < \varepsilon^{-3/2}$
Pfirsch-Schlüter	short	$\lambda_D \ll \varrho \ll \lambda_{MFP} \ll L_H$	$\varepsilon^{-3/2} \ll \nu_a^*$

**Table 2.1:** Scale ordering for the neoclassical transport regimes

### 2.2.2.1 Correction for Classical Transport

To investigate neoclassical transport we start with the observation that multiplying the momentum balance Eq. (2.32) with the major radius  $R$  and the unit vector in the toroidal direction  $\vec{e}_t$  results in the toroidal angular momentum balance equation in a tokamak. Higher order terms are discarded like in Eq. (2.40).

$$q_a n_a R \vec{e}_t (\vec{u}_a \times \vec{B}) = -q_a n_a u_{a,\psi} R B_p = -q_a \Gamma_{a,\psi} |\nabla \Psi| \quad (2.57)$$

where  $\Gamma_{a,\psi}$  and  $u_{a,\psi}$  are the particle flux density and the fluid velocity perpendicular to the magnetic flux surface respectively. Terms in Eq. (2.32) stemming from a scalar quantity (pressure, electric field due to static potential, etc.) cancel due toroidal symmetry. Inertial terms are of second order and viscosity does not change the average toroidal momentum on a flux surface, i.e.  $\langle \vec{e}_t R \nabla \vec{H}_a \rangle = 0$ . The remaining parts are the induced electric fields  $\vec{E}_{i,t}$  (current drive) and the parallel friction forces  $\vec{F}_{a,t}$ . Introducing the notation  $\langle \Gamma_a^\psi \rangle = \langle \Gamma_{a,\psi} |\nabla \Psi| \rangle$  and using the fact that  $\langle \Gamma_a^r \rangle = \langle \Gamma_a^\psi \rangle (dr/d\Psi)$ , we get

$$\langle \Gamma_a^r \rangle = \frac{dr}{d\Psi} \left( n_a \langle R E_{i,t} \rangle + \frac{1}{q_a} \langle R F_{a,t} \rangle \right) \quad (2.58)$$

where  $R$  is the major radius coordinate. The perpendicular component of Eq. (2.58) can be deduced using the relation

$$\vec{e}_t = \frac{\vec{B}_t}{B} \vec{e}_\parallel - \frac{\vec{B}_p}{B} \vec{e}_\perp \quad (2.59)$$

The inverse proportionality of the friction force to the magnetic field strength  $B$  finally yields the classical particle flux perpendicular to the magnetic flux surface. It is corrected with a geometrical prefactor.  $D_{CL}^a$  has to be replaced by  $\langle D_{CL}^a |\nabla \Psi|^2 \rangle$  and the standard gradients are to be  $\frac{d}{dr}[1]$ . The classical diffusion coefficient in toroidal geometry then is

$$\langle D_{CL}^a |\nabla \Psi|^2 \rangle = \left( \frac{dr}{d\Psi} \right)^2 \left\langle \frac{R^2 B_p^2}{B^2} \right\rangle D_{CL} \quad (2.60)$$

The perpendicular induced electric field leads to a classical pinch velocity  $\vec{v}_{CL,pinch} = -\frac{E_\perp}{B} \vec{e}_r = -\frac{E_t B_p}{B^2} \vec{e}_r$ . The classical pinch velocity is however much smaller than all other drifts and can be neglected. Neoclassical transport is however largely dominating the classical transport in most scenarios.

### 2.2.2.2 Pfirsch-Schlüter Regime

Transport in the neoclassical Pfirsch-Schlüter regime is due to parallel friction forces. In high collisionality scenarios the stress anisotropy will be kept small by collisional randomization of velocities. Since the first order perpendicular flow velocities  $\vec{u}_{a,\perp}$  are not divergence free, parallel flows build up to cancel pressure gradients. The approach is demonstrated for the diamagnetic drift velocity (c.f. second term in Eq. (2.40)). Using Eq. (2.42) and the fact of constant density and pressure on flux surfaces in lowest order, we get

$$\vec{u}_{a,\perp}^{(0)} = \frac{1}{q_a n_a} \frac{\partial p_a}{\partial \Psi} \frac{\nabla \Psi \times \vec{B}}{B^2} \quad (2.61)$$

with a non-vanishing divergence of the last multiplicand

$$\nabla \cdot \vec{u}_{a,\perp}^{(0)} = -2\vec{u}_{a,\perp}^{(0)} \cdot \frac{\nabla B}{B} \quad (2.62)$$

The magnetic field gradient pushes ions in the  $\vec{B} \times \nabla B$  and electrons in the opposite direction, thus separating the charges. The parallel flows ensure both the canceling of charge separation otherwise leading to a strong  $\vec{E} \times \vec{B}$ -outward drift and  $\nabla \cdot \vec{u}_a^{(0)} = 0$ .

$$\vec{u}_{a,\parallel}^{(0)} = \frac{RB_t}{q_a n_a} \frac{\partial p_a}{\partial \Psi} \left( \frac{1}{B} - \frac{B}{\langle B^2 \rangle} \right) \vec{e}_{\parallel} + C_a \vec{B} \quad (2.63)$$

The last term can be added to obtain a general solution. It gives the Banana-Plateau contribution determined later on in a different approach. An advantageous form with  $\langle \vec{B} \vec{u}_{a,\parallel}^{(0)} \rangle = 0$  is obtained by using

$$C_a = \frac{\hat{u}_a}{\langle B^2 \rangle} \quad (2.64)$$

Assuming a shifted Maxwellian background the previously shown expansion scheme applies and the form of the friction force in Eq. (2.35) is valid. Two distinct contributions to radial transport originating from parallel friction can be found.

$$\begin{aligned} \langle \Gamma_{a,NEO}^r \rangle &= \left( \frac{dr}{d\Psi} \right) \frac{1}{q_a} \left\langle \frac{RB_t F_{a,\parallel}}{B} \right\rangle \\ &\approx \left( \frac{dr}{d\Psi} \right)^2 (RB_t)^2 \left[ \left\langle \frac{1}{B^2} \right\rangle - \frac{1}{\langle B^2 \rangle} \right] \frac{m_a n_a}{q_a} \sum_{b \neq a} \nu_{ab} \left( \frac{1}{q_b n_b} \frac{\partial p_b}{\partial r} - \frac{1}{q_a n_a} \frac{\partial p_a}{\partial r} \right) \\ &\quad + \left( \frac{dr}{d\Psi} \right) \frac{(RB_t)}{\langle B^2 \rangle} \frac{m_a n_a}{q_a} \sum_{b \neq a} \nu_{ab} (\hat{u}_b - \hat{u}_a) \end{aligned} \quad (2.65)$$

The first term in Eq. (2.65) relates to Pfirsch-Schlüter transport, the second to Banana-plateau transport. Only considering the Pfirsch-Schlüter part one ends up with

$$D_{PS}^a = \left( \frac{dr}{d\Psi} \right)^2 (RB_t)^2 \left\langle \frac{1}{B^2} - \frac{1}{\langle B^2 \rangle} \right\rangle - \frac{m_a k_B T_a}{q_a^2} \sum_{b \neq a} \nu_{ab} \quad (2.66)$$

In a tokamak with small inverse aspect ratio  $\varepsilon$  some approximations to Eq. (2.66) apply

$$\begin{aligned} \left( \frac{dr}{d\Psi} \right)^2 (RB_t)^2 &\approx q/\varepsilon, \\ \frac{1}{\langle B^2 \rangle} &\approx \frac{1 - \varepsilon^2/2}{B_0^2}, \\ \left\langle \frac{1}{B^2} \right\rangle &\approx \frac{1 + 3\varepsilon^2/2}{B_0^2} \end{aligned} \quad (2.67)$$

where  $B_0$  is the magnetic field on the magnetic axis. In this approximation of small inverse aspect ratio the Pfirsch-Schlüter diffusion coefficient is a

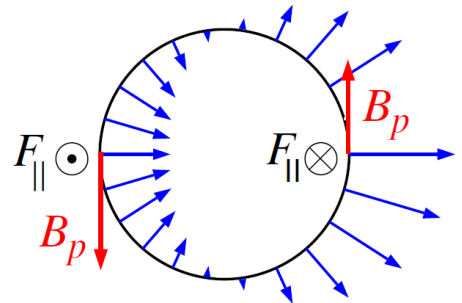


**Figure 2.5:** PS flux pattern in cylindrical geometry[62].

factor  $2q^2$  larger than the classical one.

$$D_{PS}^a = 2q^2 D_{CL}^a \quad (2.68)$$

Due to the proportionality of the parallel flow velocity  $u_{a,\parallel}$  to the cosine of the poloidal angle  $\vartheta$  the Pfirsch-Schlüter fluxes are always directed outward as shown in Fig. 2.5.

The introduction of higher moments into the calculations makes these less simple. However, higher moments, like the heat flux, are needed to see familiar additional effects like temperature screening. This is further developed in [61]. The structure of the previous results is still valid for these more exact calculations.

### 2.2.2.3 Banana Regime

Banana transport dominates the particle fluxes for low collisionality. In the banana regime particles travel large distances along the magnetic field lines. Being subject to the mirror force<sup>1</sup> some particles eventually stop and then are reflected. The trapped particles have closed trajectories like the one shown in Fig. 2.6. The so-called bounce condition can be derived from energy conservation<sup>2</sup> and is simplified by the small inverse aspect ratio approximation<sup>3</sup>.

$$\left| \frac{v_{\parallel}}{v_{\perp}} \right| \leq \sqrt{\frac{B_{max} - B_{min}}{B_{min}}} \approx \sqrt{\frac{1 + \varepsilon}{1 - \varepsilon} - 1} = \sqrt{\frac{2\varepsilon}{1 - \varepsilon}} \approx \sqrt{2\varepsilon} \quad (2.69)$$

The banana transport can be evaluated from the momentum balance (c.f. Eq. (2.65)). Here, an approach from a random walk point of view is taken instead. Bouncing particles exhibit macroscopic excursion from their original flux surface (c.f. Fig. 2.6) caused by the particle drifts. To determine the banana width  $w_b$ , the drift-velocity  $\vec{v}_D$  is calculated.

$$\begin{aligned} \vec{v}_{D,a} &= \frac{m_a}{q_a B^3} \left( v_{\parallel}^2 + \frac{1}{2} v_{\perp}^2 \right) \vec{B} \times \nabla B \\ &\approx \frac{m_a}{2q_a R B} v_{\perp}^2 = \varrho \frac{v_{\perp}}{2R} \end{aligned} \quad (2.70)$$

Curvature drift ( $\vec{v}_{\parallel}$ ) was ultimately neglected. The direction of the excursion depends on the electric charge, the sign of the z-coordinate<sup>4</sup> and the direction of the magnetic field. The electron drift velocity is directed outwards above and inwards below the magnetic axis.

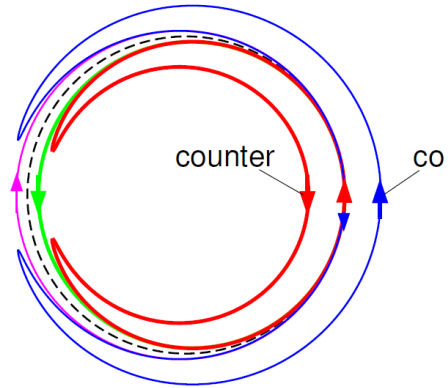


**Figure 2.6:** Banana orbit with drift induced excursion from the magnetic surface[62].

1 The mirror force is caused by  $\nabla B > 0$ . Conservation of the adiabatic invariant magnetic moment  $\mu$  of the gyrating particle leads to transfer of parallel to perpendicular momentum.

2  $E = \frac{1}{2} m v_{\parallel}^2 + \mu B$  with  $\mu = \frac{m v_{\perp}^2}{2B}$

3  $B_{min} \approx B_0/(1 - \varepsilon)$  and  $B_{max} \approx B_0/(1 + \varepsilon)$

4 The z-coordinate is zero at the height of the magnetic axis.

The bounce time  $\tau_B$  is approximately given by

$$\tau_B \approx \frac{2\pi q R}{v_{\parallel}} \quad (2.71)$$

leading to a banana width of

$$w_b = v_D \tau_B \approx \varrho \frac{2\pi q R}{2R} \frac{v_{\perp}}{v_{\parallel}} = \varrho \frac{\pi q}{\sqrt{2\varepsilon}} \approx \varrho \frac{q}{\sqrt{\varepsilon}} \quad (2.72)$$

The banana width is the characteristic length of the random walk process leading to diffusion. To determine the characteristic time, i.e. the collision time, the approach in the original Hazeltine-Hinton paper on neoclassical transport is followed[65, p.256]. The classical collision time refers to a change in pitch angle of  $\pi/2$ , whereas here only changes of the order of  $\sqrt{\varepsilon}$  are acceptable in order to preserve the particle trapping.

$$\nu_{eff,a} = \frac{\nu_a}{\Delta\alpha^2} \approx \frac{\nu_a}{\varepsilon} \quad (2.73)$$

Only collisions of trapped particles are considered, because the maximum displacement of passing particles  $\varrho$  is much smaller than  $q\varrho/\sqrt{\varepsilon}$ . The fraction of trapped particles  $f_{t,a}$  is given by

$$f_{t,a} = \frac{n_{t,a}}{n_a} = \frac{1}{4\pi} \int_0^{2\pi} d\varphi \int_{-\sqrt{2\varepsilon}}^{\sqrt{2\varepsilon}} \cos\vartheta d\vartheta \approx \sqrt{2\varepsilon} \quad (2.74)$$

Combining Eqs. (2.72-2.74) we get a diffusion coefficient for the banana regime.

$$D_{BP}^a = f_{t,a} \nu_{eff,a} w_b^2 \approx \frac{q^2}{\varepsilon^{3/2}} D_{CL}^a \quad (2.75)$$

### Ware Pinch

Until now the external toroidal electrical field used to generate the plasma current was never considered. Ions (electrons) moving in co-current direction are (de-)accelerated by the electric field while in the counter-current direction the situation is reversed. The conservation of the canonical toroidal angular momentum reads

$$\begin{aligned} p_{\phi} &= m_a R v_{\phi,a} + q_a R A_{\phi} \\ &= m_a R v_{\phi,a} + q_a \Psi = \text{const} \end{aligned} \quad (2.76)$$

where  $A_{\phi}$  is the toroidal vector potential,  $v_{\phi,a}$  is the toroidal velocity of species  $a$  and  $\Psi$  is the magnetic flux. Taking the time derivative one obtains[65]

$$\begin{aligned} \frac{d\Psi}{dt} &= \frac{\partial\Psi}{\partial t} + \vec{v}_{\Psi} \cdot \nabla\Psi \\ &= -R E_t^{ext} + v_{\Psi} R B_p = -\frac{m_a}{q_a} \frac{d(R v_{\phi})}{dt} \end{aligned} \quad (2.77)$$

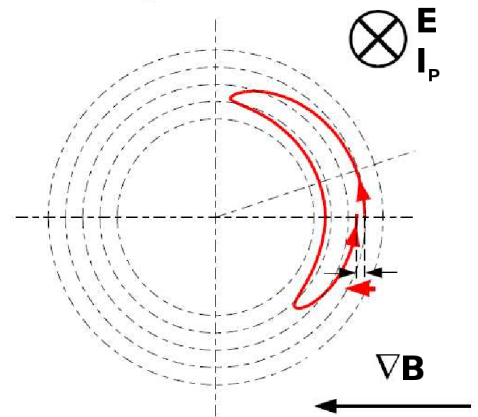


**Figure 2.7:** Ware pinch[62].

where  $E_t$  is the toroidal electric field,  $v_\phi$  is the toroidal particle velocity and  $v_\psi$  is the flux surface velocity. The topology of the magnetic field does not change significantly in time. This implicates  $\frac{d\psi}{dt} = 0$  and results in the radial velocity  $v_\psi$ .

$$v_\psi = \frac{E_t^{ext}}{B_p} \quad (2.78)$$

$v_\psi$  is radially directed inward and equal for all particle species. Further investigation leads to the expression[1]

$$\langle \Gamma_{Ware,a}^r \rangle = \kappa_{Ware} n_a f_{t,a} \left\langle \frac{E_t^{ext}}{B_p} \right\rangle \quad (2.79)$$

where  $\kappa_{Ware}$  is a factor dependent on collisionality. The dependence on  $\nu_a^*$  corrects for the fact that at high collisionalities only a small part of the banana orbit can be completed before a collision.  $\kappa_{Ware}$  is close to unity at low collisionality and vanishes at high collisionality. For main ion species, which have low collisionality, the Ware-pinch velocity is about  $B/B_P \approx 100$  times larger than the classical pinch velocity. For impurities with higher collisionalities the classical pinches usually dominate. It is pointed out that only trapped particles are subject to the Ware-pinch. Passing particles just gain toroidal momentum at the same rate at which  $\psi$  changes locally without movement of the orbit.

#### 2.2.2.4 Plateau Regime

For intermediate collisionality collisions can be frequent enough to prevent particles from completing banana orbits. Still gyrocenter motion is significant for particles with  $v_\parallel < v_0$ , where  $v_0$  is a limiting velocity[65, p.257]. The collision frequency for collision, which scatter particles such that the condition no longer applies is given by the same argument as in Eq. (2.73).

$$\nu_{v_0,a} = \left( \frac{v_{th}}{v_0} \right)^2 \nu_a \quad (2.80)$$

Particles will suffer collisions before they complete the half-banana above or below the midplane if  $\nu_{v_0,a} > v_\parallel/qR$ . This incomplete orbits come with an uncompensated drift motion representing a random-walk with step-size  $v_D^r/\nu_{v_0,a}$ , where  $v_D^r$  is the radial projection of the drift velocity. Adding the fact that only a fraction  $v_0/v_{th}$  of all particles contribute, introducing the trapped particle transit frequency  $\omega_T = \frac{v_{th}}{qR}$  and exploiting the fact that  $v_0/qR = \nu_{v_0,a}$ [65], we ultimately get

$$D_P^a = \nu_{v_0,a} \frac{v_0}{v_{th}} \left( \frac{v_D}{\nu_{v_0,a}} \right)^2 = \frac{v_D}{\omega_T} \quad (2.81)$$

The diffusion coefficient in the plateau regime is independent from the collision frequency  $\nu_a$ . However, the plateau regime does not occur in real fusion devices. The inequalities the collisionality has to obey cannot be strictly satisfied for typical inverse aspect ratios. Nevertheless, the plateau regime gives an explanation for a relatively mild flattening of the  $D$  over  $\nu^*$  plot at the transition from the Banana to Pfirsch-Schlüter regime.



### 2.2.2.5 Total Neoclassical Radial Fluxes

All neoclassical radial flux equations have a similar structure. This allows a very simple form of the total radial neoclassical particle flux stemming from the collisions of particle species  $a$  with species  $b$ .

$$\Gamma_a^r = \sum_{x=CL,PS,B,P} \sum_{b \neq a} D_x^{ab} \left( -\nabla n_a + n_a \underbrace{\frac{q_a}{q_b} \left( \frac{\nabla n_b}{n_b} + H_x^{ab} \frac{\nabla T}{T} \right)}_{v_x^{ab}} \right) \quad (2.82)$$

where  $H_x^{ab}$  are the collisionality dependent temperature gradient factors and  $D_x^{ab}$  and  $v_x^{ab}$  are the diffusion and convection coefficients. The evaluation of neoclassical transport coefficients is cumbersome and usually done by numerical codes like NEOART[10].

### 2.2.2.6 Limitations of Neoclassical Transport Theory

Standard neoclassical transport theory is depending on the conditions and assumptions, which do not apply in some cases. The developed standard theory is not valid under several circumstances:

- Near the magnetic axis the assumption  $w_B \ll \varrho$  breaks down
- For strong gradients  $w_B \ll L_x$  for  $x = n, T$  breaks down
- In High-Z impurity plasmas with strong rotation ( $v_{Mach} \gg 1$ ) the assumption of constant density on flux surfaces breaks down

### 2.2.3 Anomalous Transport

Neoclassical transport is not able to explain the radial transport coefficients derived from experimental measurements. The measured transport coefficients are orders of magnitude larger than predicted by neoclassical theory. The missing phenomena are summarized as anomalous transport and are supposed to be of turbulent nature. A possible explanation for anomalous transport are micro-instabilities. Local fluctuations in density, temperature and the electrostatic potential lead to fluctuating  $\vec{E} \times \vec{B}$ -drifts, so-called drift waves. The Ion Temperature Gradient (ITG) mode, the Electron Temperature Gradient (ETG) mode and the Trapped Electron Mode (TEM) are the precursors of the corresponding, dominant instabilities. The instabilities occur in different

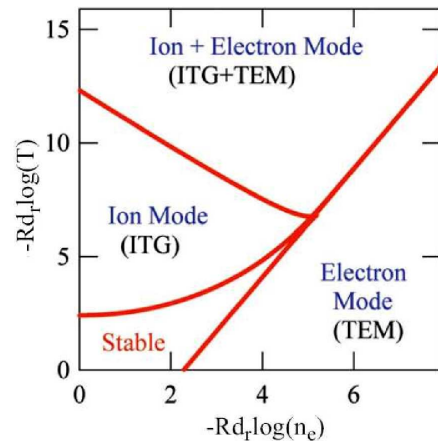


**Figure 2.8:** Stability diagram of ITG and TEM[62].

The instabilities occur in different

regimes in the form of single or mixed instabilities. Characteristic quantities, which determine the regimes are the normalized (logarithmic) gradients

$$\frac{R}{L_n} = -R \frac{d}{dr} \log [n] = -R \frac{\nabla n}{n} \quad \& \quad \frac{R}{L_T} = -R \frac{d}{dr} \log [T] = -R \frac{\nabla T}{T} \quad (2.83)$$

Figure 2.8 shows the regimes and the parameter space of their validity. One particular important property of anomalous transport is that it cannot be parameterized in the standard diffusive and convective ansatz[66; 67]. An overview of tokamak transport processes, including turbulent transport can be found in [33].

## 2.3 Reactions

In plasmas a variety of different physical and chemical reactions can occur depending on the particle species present in the plasma, the plasma parameters such as temperature and density, and the wall interface (material, geometry, etc.). This section only covers reactions included in the presented EIRENE simulation. The sources of the atomic data are specified and the reaction models are shortly introduced.

### 2.3.1 Plasma-Particle Interaction

The plasma-particle interactions in EIRENE are of differing nature. There are reactions which act on particles of fixed particle species like thermalization collisions. These reactions change the particle properties (velocity, energy, etc.), but leave the particle species (element, charge state, etc. ) unchanged. And there are the species transforming reactions like electron-impact ionization. They change the particle properties and the species index. Both kinds of reactions are present in the following simulations.

#### 2.3.1.1 Inelastic Collisions

The current particle-plasma reactions classify as species transforming reactions, because the EIRENE setup only includes electron impact reactions of the simulated trace impurity tungsten. All other possible reactions are neglected. A general review on ionization data and numerical methods can be found in [68]. The rate coefficients supplied to EIRENE are from the ADAS database. Information on the Atomic Database in Applied Science (ADAS) can be found in [69] and a more particular article describing impurity light emission and ionization is [70].

#### Electron Impact Reaction

Currently there are only electron impact reactions of tungsten, more precisely electron impact ionization (c.f. Eq. (2.84)) and radiative recombinations (c.f. Eq. (2.85)), included in our EIRENE simulations. The reactions are generally described by the

following two reaction equations.



Dealing with rather low densities of order  $10^{19} - 10^{21} \text{m}^{-3}$  in fusion plasmas corona equilibrium is assumed. Only radiative recombinations contribute to the recombination process and produced photons escape the optically thin plasma without interacting. In corona equilibrium electron impact reactions are sufficient for the evaluation of the charge state distribution of tungsten properly. The rate coefficients in principle do not depend on the electron density, because collision induced recombination is neglected. The average charge state is solely determined by the plasma temperature.

### Electron Impact Data

The rate coefficients for ionization were taken from Loch[71]. The data results from CADW direct ionization, CADW excitation and configuration average branching ratio calculations. The ionization rate coefficients do not depend on the electron density<sup>1</sup>. The CADW data was assembled from ADAS adf23 files. The original recombination data was calculated by Post with an average ion model (ADPAK)[72; 73]. It was enhanced by Pütterich, who matched the coefficients with prefactors to experimental results[74]. The rate coefficient for recombination is now weakly dependent on electron density. The rate coefficients currently in use are subject to major uncertainties and the actual value can vary by a factor of about two within the error bars. The accuracy increases with the degree of ionization, because ever littler electrons have to be calculated in the quantum mechanics simulations.

The rate coefficient  $S$  determines the reaction rate  $\nu$  and the mean free time  $\tau$  between such reactions.

$$\tau = \frac{1}{\nu} = \frac{1}{n_e S} \quad (2.86)$$

with the rate coefficient  $S$  given by

$$S = \langle v \sigma(v) \rangle \quad (2.87)$$

where  $\sigma$  is the cross-section of the reaction under consideration and  $v$  is the relative velocity of the particles. The angular brackets denote the average over the relative velocity distribution function, which is a Maxwellian with the species weighted temperature  $T_{ab} = \frac{m_b T_a + m_a T_b}{m_a + m_b}$  and mass  $m_{ab} = \frac{m_a m_b}{m_a + m_b}$ [75]. Further information on the evaluation of ionization/recombination cross-sections and rate coefficients can be found in [38; 68; 70]. The ionization energies were taken from the adf00 branch of the ADAS database[69]. The same remarks on accuracy apply as mentioned above.

---

<sup>1</sup> A weak dependence could however be introduced despite the neglect of collision-induced recombination, because the electron density influences the average excitation state the reacting particle will be in.

### 2.3.1.2 Elastic Collisions

Plasma-particle collisions are those plasma reactions, which do not alter the particle species but change particle properties. This interaction is due to collisions of two or more particles and is described in Sec. 2.2. For the sake of comprehensiveness some of the most important examples of a possible description are presented.

#### Boltzmann Equation

The general description of particle collisions and their effect on the evolution of an ensemble of particles is described by the Boltzmann equation.

$$C[f] = L[f] \quad (2.88)$$

where  $C[f]$  is the collision operator, also denoted  $\partial_t f|_{coll.}$ , and the Liouville operator  $L$  is given by

$$L = p^\alpha \frac{\partial}{\partial x^\alpha} \Gamma_{\beta\gamma}^\alpha p^\beta p^\gamma \frac{\partial}{\partial p^\alpha} \approx \underbrace{\partial_t + \vec{v} \cdot \nabla_r + \frac{\vec{F}}{m} \nabla_v}_{non-relativistic} = L_{NR} \quad (2.89)$$

Several approximations with different assumptions and validity regimes exist. In general all approaches start from the equations above, but the resulting collision operator varies substantially. The interaction between multiple particles is described by the collision operator on the right-hand side of Eq. (2.20). The collision operator can take various forms depending on the assumptions and approximations, which apply to the collision regime scrutinized. Some of the common examples shall be shortly presented.

#### BGK-Approximation

The BGK<sup>1</sup>-approximation is one of the most simple approaches to the Boltzmann equation. An equilibration time  $\tau$  is introduced.  $\tau$  gives the timescale on which a disturbed Maxwell distribution  $\tilde{f}$  relaxes to the equilibrium Maxwell distribution  $f$ .

$$C[f] = \frac{\tilde{f} - f}{\tau} \quad (2.90)$$

This type of approximation is used in an EIRENE update for thermalization described in Subsec. 3.3.1.6.

#### Stoßzahlansatz

The Stoßzahlansatz of Boltzmann is also known as the molecular chaos assumption. It assumes totally uncorrelated particles before a collision. The collisions are assumed to be only two-body interactions. The collision operator is obeying the common conservation laws and uses the cross-section  $\sigma$  as an interaction strength parameter.

$$C[f] = \iint \sigma(\vec{v} - \vec{v}', \vec{q}) \left[ f(\vec{x}, \vec{p} + \vec{q}, t) f(\vec{x}, \vec{p}' - \vec{q}, t) - f(\vec{x}, \vec{p}, t) f(\vec{x}, \vec{p}', t) \right] d^3 p d^3 q \quad (2.91)$$

### Vlasov Equation

Some inconsistencies<sup>1</sup> and divergences in kinetic terms in the pair collision treatment lead to the Vlasov equation. Instead of using the two-body collisions Vlasov introduced self-consistent fields  $\vec{E}$  and  $\vec{B}$  to describe the long-range Coulomb interaction. This procedure describes rather multiple small-angle scattering behavior than large-angle scattering as with the Stoßzahlansatz. The interaction is described by the Vlasov equation

$$\frac{\partial f_a}{\partial t} + \vec{v} \cdot \nabla_x f_a + \frac{q_a}{m_a} (\vec{E} + \vec{v} \times \vec{B}) \cdot \nabla_v f_a = 0 \quad (2.92)$$

for  $a = e$  or  $a = i$  and Maxwell equations

$$\begin{aligned} \nabla \times \vec{B} &= \mu_0 \vec{j}, & \nabla \cdot \vec{B} &= 0 \\ \nabla \times \vec{E} &= -\partial_t \vec{B}, & \nabla \cdot \vec{E} &= \frac{\varrho_q}{\varepsilon_0} \end{aligned} \quad (2.93)$$

with the charge distribution  $\varrho_q$  and the current distribution  $\vec{j}$

$$\varrho_q = e \int (f_i - f_e) d^3p, \quad \vec{j} = e \int \vec{v} (f_i - f_e) d^3p \quad (2.94)$$

A more sophisticated version including the interaction with average fields and two- or/and three-body collisions is introduced in [61, p.110].

### Fokker-Planck Equation

The Fokker-Planck equation is another possible approach to describe the long-range effects of the Coulomb interaction. It describes the process of the small-angle scattering in Coulomb collisions by convection and diffusion in velocity space. A drift and a diffusion coefficient are introduced. They can be parametrized by the Rosenbluth potentials. Details are described in Sec. 2.2 and references therein.

## 2.3.2 Plasma-Wall Interactions

### 2.3.2.1 Sputtering

Sputtering was already extensively described. We refer the reader to Subsec. 2.1 and references therein.

### 2.3.2.2 Reflection & Absorption

Fast particle reflection at walls in EIRENE is governed by the model presented in the article by Eckstein[76]. The basic idea is the introduction of reflection coefficients for particles, energy and momentum dependent on the reduced energy  $\varepsilon$  as defined in Eq.

---

<sup>1</sup> The Coulomb force is a long-range force. A fact that is not considered by the Stoßzahlansatz (e.g. Oscillations in electron plasmas).

(2.5). The reflection coefficients are parametrized by

$$R_{N/E} = \frac{A_1 \ln [A_2 \varepsilon + e]}{1 + A_3 \varepsilon^{A_4} + A_5 \varepsilon^{A_6}} + \underbrace{A_7 \ln \left[ \frac{A_8}{\varepsilon} \right]}_{\text{for } \varepsilon > 40 \text{ eV}} \quad (2.95)$$

for differing species of incident ions and surface material. For self-bombardment one has

$$R_{N/E} = \frac{A_1 \ln [A_2 \varepsilon + e]}{1 + A_3 \varepsilon^{A_4} + A_5 \varepsilon^{A_6}} \left( \left( 1 - \frac{A_7}{\varepsilon} \right)^{A_8} \right)^{A_9} \quad (2.96)$$

The difference for self-bombardment is the acceleration of ions to the surface due to the surface-binding energy and resulting forces. In EIRENE the implemented model is based on reflection coefficients calculated with the TRIM code described in [55; 77–79]. TRIM is a Monte-Carlo code kinetically simulating incident ions and the resulting collision cascade in the surface material. The reflection coefficients for particle reflection  $R_N$ , energy reflection  $R_E$  and momentum reflection  $R_p$  are reduced information defined by

$$\begin{aligned} R_N(E_0, \theta_0) &= \int_0^{E_0} \int_0^\pi \int_0^{2\pi} dE d\theta d\phi \sin[\theta] f(E, \theta, \phi | E_0, \theta_0) \\ R_E(E_0, \theta_0) &= \int_0^{E_0} \int_0^\pi \int_0^{2\pi} dE d\theta d\phi \sin[\theta] E f(E, \theta, \phi | E_0, \theta_0) = R_N \frac{\overline{E}_{ref}}{E_0} \\ R_p(E_0, \theta_0) &= \frac{1}{p_{0,\parallel}} \int_0^{E_0} \int_0^\pi \int_0^{2\pi} dE d\theta d\phi \sin[\theta] p_{0,\parallel} f(E, \theta, \phi | E_0, \theta_0) = R_N \frac{\overline{M}_{ref,\parallel}}{M_{0,\parallel}} = R_N \frac{\overline{v}_{ref,\parallel}}{E_{0,\parallel}} \end{aligned} \quad (2.97)$$

The reflection coefficients for energy and momentum are stored as fixed, so-called quantiles (0.1, 0.3, 0.5, 0.7, 0.9) and their associated energies or momenta respectively. The quantiles define the associated energies by

$$Q_i = P \{ E < E_i \} \quad (2.98)$$

and momentum by

$$Q_j^i = P \{ \cos[\theta] < \cos[\theta_j^i | E_i] \} \quad (2.99)$$

and

$$Q_k^{i,j} = P \{ \cos[\phi] < \cos[\phi_k^{i,j} | E_i, \theta_j] \} \quad (2.100)$$

From this quantities the reflection coefficients are reconstructed. More precisely the reflection Monte-Carlo routines sample the state variables for reflected particles directly from theses quantities. The available target-projectile combinations can be found in [55]. For non-existing combina-

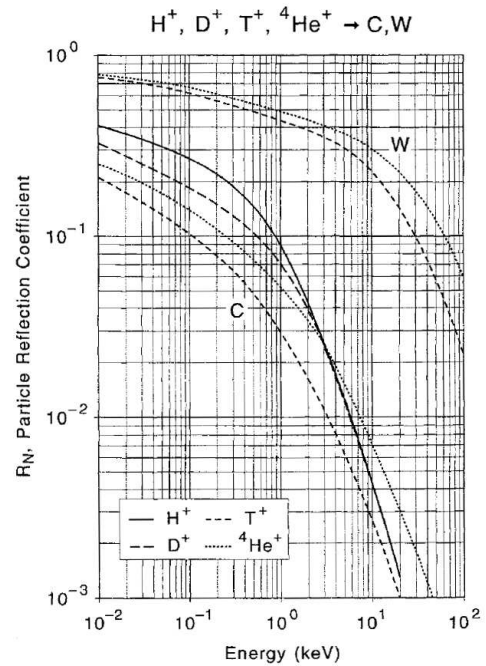


**Figure 2.9:** Reflection coefficient for main fuel species on tungsten and carbon[76].

tions a scaling exists. This EIRENE specific scaling is explained in Sec. 3.2.6.2 in detail. EIRENE also includes a thermal particle reflection model. In this model a reflected particle is assigned properties from different user-selected distributions, for example is a cosine velocity distribution with a surface temperature Maxwellian energy distribution.

# CHAPTER 3

---

## Numerics

---

This chapter describes some state-of-the-art numerical codes that are available for plasma simulations. All codes employed in this work, especially the EIRENE code, are described in greater detail. Restrictions applying to used programs as well as important numerical effects are pointed out and explained.

The first section introduces state-of-the-art numerical tools and describes the approximations, which apply to the some codes like EIRENE. The last paragraph summarizes approximations used in this work – implicitly in the EIRENE code and explicitly in the setup of EIRENE.

The second section describes the original state of EIRENE 2010 and Seebacher’s recently incorporated Trace-Ion Module (TIM)[6] at the beginning of this thesis. Following a short introduction to the philosophy of Monte-Carlo code EIRENE, an overview of the general program flow and its modifications due to the TIM is given. The previously introduced theoretical models of particle production (source), transport and reactions are described with respect to the implementation in EIRENE.

Finally the third section deals with new models and new features introduced and integrated in EIRENE in the course of the thesis. Code and the EIRENE setup preparations are presented. New routines were included in EIRENE, such as a prompt redeposition scheme, and necessary preparation steps to run EIRENE, like the grid and background generation, were taken care of. The chapter is closed with the description of supplemental numerical tools.

### 3.1 Motivation of Choice

In order to select a numerical tool to work with, an examination of the available state-of-the-art methods for transport simulations in tokamaks as well as their limitations and their applied assumptions/approximations is undertaken. This provides the possibility to make the most suitable choice for a given task and to get to know the restrictions applying to this choice. It is very important to bear these restriction in mind during the setup preparations and the analysis of the results. Otherwise false deductions and misleading conclusions could be made. The following discussion leads to the conclusion



why EIRENE could be chosen as the appropriate numerical tool and what advantages and disadvantages this choice brings. The actual validation is postponed to Chapter 4.

### 3.1.1 Available numerical tools

At present there is a variety of available state-of-the-art numerical tools to calculate transport in plasmas or to even simulate the entire evolution of a plasma for given boundary conditions. The code packages can be divided into two major groups, the so-called fluid codes and the kinetic codes.

Fluid codes, like B2.5[7] or EMC3[80–82] used at IPP, UEDGE used at DIII-D and EDGE2D used at JET, rely on the solution of fluid equations, which describe the evolution of different moments of the one-particle distribution function. The most important advantage of the fluid approach is speed. Fluid codes are much faster than the kinetic description, because they do not have to solve the equation of motion for lots of single particle trajectories. They have to solve a the fluid moment balance equations (c.f. Appendix A.6) on a given grid for all different species. The species specific equations are coupled by sink and source terms. The fluid approach ultimately leads to a system of coupled equation, which has to be solved self-consistently. However the fluid codes are only applicable under conditions listed in the following[83, p.65,94].

1. The distribution function  $f$  is taken to be a (shifted) Maxwellian.
2. The characteristic length scales of the fluid moments,  $L_X = X/\nabla X$  with  $X = T_e, T_i, n_e$  or  $n_i$ , have to be much larger than perturbations and the intrinsic length scales, given by the mean free path  $\lambda$ , the Debye length  $\lambda_D$  or the gyroradius  $\varrho$  –  $\mathcal{L}_x \gg \lambda, \lambda_D, \varrho$ .
3. The collisionality  $\nu^*$  must be large enough to ensure frequent collisions in order to establish a fluid. The properties of the single particles are coupled together and the following inequalities for the ion and electron collision times  $\tau_{i/e}$  and the hydrodynamic time scale  $\tau_H$  apply –  $\tau_H \gg \tau_e \gg \tau_i$ .

Given the above conditions the plasma can be assumed to be in local equilibrium. The fluid moments then describe the state of the system completely. The need of a Maxwellian distribution is equivalent to postulate thermalized particles. The length scale arguments provide that background quantities like  $n_e$  vary only weakly on characteristic, kinetic length scales ( $\lambda, \lambda_D, \varrho$ ). This enables a (linear) expansion of the background quantities and keeps the acting forces small. Sufficiently large collisionality finally ensures that particle velocity orientations are kept random and that parallel and perpendicular energies equilibrate<sup>1</sup>. Consequently a local thermal quasi-equilibrium is guaranteed.

If the conditions are not respected the assumption of a local quasi-equilibrium breaks down. Fluid moments only are no longer an appropriate description of the full system. Non-fluid effects, like supra-thermal particles, are then also determining the state of the system. The averaging of the fluid moment description would smooth out some impor-

---

<sup>1</sup> Gyro-averaging is valid for the fluid description[61; 83].

tant kinetic effects. Apart from the collapse of the fluid model, some effects<sup>1</sup> also call for the need of a more complete knowledge of a single particle's state. This information is completely lost during the fluid averaging process and can only be corrected for by an approximated model. The second numerical approach used by kinetic codes is therefore a (full) kinetic description of single particles and is in principle more sound.

The full kinetic description can be used without intrinsic need for restrictions on any kind of scales or a scale ordering. However, the major drawback is the computationally intense calculations necessary to solve many single particle<sup>2</sup> equations and store the trajectories. Most kinetic codes determine the one-particle distribution function by simulation of individual particles and subsequent averaging processes. The procedure is usually computationally more expensive than the fluid approach, because a large number of particle trajectories (50k-10M) is needed for sufficient statistics and accuracy.

Therefore many codes introduce some basic assumptions and restrict the validity of the calculations to a certain parameter space in order to simplify the applied models, thereby facilitating the calculations and reducing the computational time. An example for such a simplification is the gyro-averaged drift-approximation used in EIRENE and DIVIMP or the trace approximation used in the framework of this thesis (c.f. Subsec. 3.2.1).

There is a variety of kinetic codes with different approaches to the problem. Prominent code genres include Particle In Cell (PiC), Finite Volume and Particle-Tracing codes. Present state-of-the-art examples of particle tracing, kinetic codes are EIRENE[4], DIVIMP[84; 85], ERO[49], IMPGYRO[86; 87] and ASCOT[88]. The EIRENE code is used in this work and described below in Sec. 3.2. DIVIMP (DIVertor IMPurity), developed by P. Stangeby, is a two dimensional, gyro-averaged and field-aligned Monte-Carlo code for ions and neutrals in divertor geometry. Classical diffusion along the magnetic field lines in velocity space and anomalous diffusion across magnetic field lines in real space is taken into account by DIVIMP. Ionization and recombination processes as well as thermalization with the background and thermal force effects are included. Plasma-wall interaction routines for sputtering and particle reflection exist. The transport kernel of the ASCOT code is related to DIVIMP. It additionally incorporates the  $\vec{E} \times \vec{B}$ ,  $\nabla \vec{B}$ , curvature, polarization and gyroviscosity drifts. Thermalization is described by Coulomb collisions with background particles. The code is also written in straight field line coordinates to avoid numerical drifts due to field line curvature.

ERO and IMPGYRO are distinct from these codes as they take into account the fully resolved ion motion. No gyro-averaging is applied. However, this comes at the cost of computational time. ERO limits this need by restricting the computational domain to a small fraction of the device geometry[49].

A full description of the plasma evolution commonly includes both kind of codes, fluid and kinetic. They are combined in packages like SOLPS 5.0 (B2.5 & EIRENE'99) and EMC3-EIRENE at IPP, UEDGE-EIRENE/DEGAS at DIII-D or EDGE2D-EIRENE at JET to profit from the advantages explained above of both codes. In the coupled simulation scheme the fluid code calculates the evolution of the dominant species, while the kinetic code takes care of neutrals, (trace-)impurities or short-lived ions taking into account possible non-fluid effects. In most cases the kinetic code also simulates the plasma-wall interaction. The iterative coupling between the codes is commonly implemented by exchange of source and sink terms for particles, energy and momentum.

---

1 An example of such an effect the fact that the incident angle distribution for sputtering projectiles is strongly centered around normal incidence. This largely modifies the yield.

2 The term 'particle' may sometimes describe non-material quantities like a certain amount of heat[81] or an ensemble of particles[4] in the context of Monte-Carlo transport simulations.

We decided to use the gyro-averaged, kinetic Monte-Carlo code EIRENE. EIRENE will be described in detail in the next section.

## 3.2 EIRENE

The kinetic transport code EIRENE is a three dimensional Monte-Carlo code, relying on a guiding center approximation[4]. EIRENE was initially developed as a Monte-Carlo transport code for neutrals and is commonly used as such in a variety of program packages such as SOLPS[7]. Later a Simple Follow Ion Model (SFIM) to trace charged particles was integrated into EIRENE.

The Trace-Ion Module (TIM) of J. Seebacher recently introduced a more sophisticated tracing model for ions. Now EIRENE includes (neo-)classical effects such as drifts and Fokker-Planck thermalization, accounting for thermal and frictional forces. However, due to missing spatial diffusion, thus an implicit assumption of a  $\varrho \approx 0$ , the validity of the neoclassical transport description is restricted to the banana regime. This limitation was overcome in this thesis by the implementation of a perpendicular diffusion routine, see Subsec. 3.3.1.4.

Apart from transport EIRENE includes various models for particle generation, particle- and plasma-wall interaction and plasma-particle interactions. These include physical and chemical reactions like ionization and recombination. Before describing the EIRENE specific routines a short presentation of the approximations applied to all our simulations and the general idea of Monte-Carlo simulations is given in the next two subsections.

### 3.2.1 Applied Approximations

In the framework of this thesis two important approximations are used. The current version of EIRENE is not yet coupled to B2.5. In lack of a coupling to a fluid code no iteration of the background calculations, taking into account the EIRENE results, are carried out. We assume that the tungsten impurity handled by EIRENE on a fixed plasma background would not influence or change the plasma background substantially. This approximation is called the trace approximation. The use of the trace approximation is supported by experimental data. Only little tungsten is present in the SOL, the region we are simulating. Neither radiation cooling, self-collisions, plasma dilution, nor any other kind of coupling effect should have a substantial impact on the background plasma. Radiation cooling in the core could be an issue for tungsten simulations[39]. The inner core ( $\varrho_{pol} < 0.2$ ) is, however, not included in our simulations.

The second approximation, the guiding center approximation, is EIRENE inherent. EIRENE follows only the gyrocenter motion, taking advantage of the gyro-averaged description of ions in a plasma. The following relations apply:

$$L_B \gg \varrho \tag{3.1}$$

$$L_X \gg \varrho \quad \text{with} \quad X = n_e, n_i, T_e, T_i \tag{3.2}$$

$$\tau_H \gg \frac{2\pi}{\omega_c} \tag{3.3}$$

where  $\tau_H$  is the characteristic fluid time for the fluid processes. We will check the validity of these relations in Subsec. 4.1.1.

### 3.2.2 Monte-Carlo Principles

Monte-Carlo methods rely on the principle of averaging the behavior of many single events that follow an evolution based on a probabilistic decision-processes. From a mathematical point of view Monte-Carlo transport simulations are series of Markovian chains. The basic equation for Monte-Carlo transport calculations is

$$\partial_t f_i + \vec{v} \cdot \nabla_r f_i + \nu_i(\vec{r}, \vec{v}) f_i = \int C(\vec{r}; \vec{v}', i' \rightarrow \vec{v}, i) |\vec{v}' - \vec{V}'| f_i d^3 v' + Q_i(\vec{r}, \vec{v}, t) \quad (3.4)$$

where  $C(\vec{r}; \vec{v}', i' \rightarrow \vec{v}, i)$  is the collision kernel. It gives the number of particles of species  $i$  with velocity  $\vec{v}$  which emerge from collisions of particles  $i'$  with velocity  $\vec{v}'$ .  $Q_i$  is the (primary) source of particles  $i$  with velocity  $\vec{v}$  and  $\nu_i$  is the total collision frequency giving the number of collisions for particles  $i$  with velocity  $\vec{v}$  during a unity time interval. A more detailed description of Monte-Carlo transport calculations is given in Appendix A.5 and in [89]. We now turn to the implementation of these principles in EIRENE.

### 3.2.3 Introduction & Program Flow

The program flow of EIRENE is quite clearly structured and simple on the conceptual side. Figure A.7 in Appendix A.4 shows the principal program flowchart of the code, divided into three main parts. The start-up routines read the input from various sources like physical databases, geometry files, plasma background data and user control input. EIRENE precalculates many quantities, like e.g. the reaction rates, and stores them in arrays. This avoids overhead and speeds up the calculations. The second part of the code is the transport kernel, carrying out all Monte-Carlo transport calculations (c.f. Subsec. 3.2.5). The final part of the code produces numerical and graphical output. EIRENE produces particle trajectory plots, tallies<sup>1</sup> of various physical quantities and fluid moments, source distributions and diagnostic signals like line integrated signals for direct comparison with experimental measurements. Despite being a kinetic code EIRENE does not provide the complete one-particle distribution function, but is restricted to moments of it.

The transport kernel of EIRENE is depicted in Fig. A.8 in Appendix A.4. It consists of two loops – the outer loop for different stratas<sup>2</sup>, the inner loop for single particles released by the stratum. EIRENE results are thus available stratum-separated (stratified) as well as in total.

Two different types of transport for a single particle – charged and non-charged – are described in Subsec. 3.2.5. EIRENE first samples the particle from a source with given parameters, then traces it and finally executes collisions or reactions. In the remainder

<sup>1</sup> A 'tally' is an array of a physical quantity.

<sup>2</sup> 'Strata' is the EIRENE term for a source entity and related data.

of this section this life cycle of a particle is followed in order to describe the simulation process of the particles in EIRENE.

### 3.2.4 Sources

Source distributions and properties critically determine the profiles and the effects of the simulated particles on the plasma. We again point out that EIRENE-particles may represent an ensemble of physical particles with a particle weight larger than one. The particle properties (kinetic energy, velocity, etc.) are determined either from user selected distribution functions, linked to sources defined in Block 7 of the EIRENE input, or by conservation laws and probability densities in case of reaction based sources.

For user-specified, preimposed sources in EIRENE simulations, a stratified source scheme is used. The primary source distribution is decomposed into individual sources – the so-called stratas. Each single source is independently simulated and the results are linearly superposed at the end of the calculations. No cross-interactions are taken into account in the non-time-dependent mode of EIRENE, which is used through this work. EIRENE has four different kinds of preimposed source types:

1. Point sources - Located at a user-specified point inside the computational mesh.
2. Line sources - Attributed to a user-specified line inside the computational mesh.
3. Surface sources - Attributed to an additional or a so called 'non-default-standard'<sup>1</sup> surface with different spatial distributions.
4. Volume sources - Attributed to a given volume/cell.

All sources have to be supplied with a relative source strength in Ampère or a dependence on background parameters like e.g. temperature of and influxes on the target. Distribution laws for energy and velocity have to be selected. Point and line sources always impose particle influxes without any underlying physical process in EIRENE, whereas surface and volume sources can be attributed to physical processes leading to particle production.

#### Plasma Reactions

An example of a physical process constituting a volume particle source is ionization of background plasma species. EIRENE provides the possibility to define reactions of background plasma particles, which are not explicitly followed by EIRENE. The particles used in these reactions are sampled from the background plasma. These 'bulk' reactions are specified in the reaction card section (Block 4) in the EIRENE input.

#### Sputtering

An example for a surface source fueled by a physical mechanism is sputtering. The properties of the sputter model are set in the surface model section (Block 6) of the EIRENE input. For impinging particles EIRENE calculates the sputtering yield and the

---

<sup>1</sup> A non-default-standard surface is part of the vessel boundary geometry in EIRENE.

reflection probability. According to the results, EIRENE generates or modifies particles. Only the Eckstein model (c.f Chapter 2) is used in this thesis and the most recent Eckstein model available is applied. In case no Eckstein sputtering data at all is available a simple parameterization model is implemented[52]. Physical and chemical sputtering are treated separately. Following the sputtering calculations<sup>1</sup> a prompt redeposition routine (c.f. Subsec. 3.3.1.2) is called. EIRENE only traces one sputtered EIRENE-particle per sputtering event even though the yield may exceed one. The sputtering yield is accounted for by appointing an appropriate weight to the sputtered particle. Sputtered particles are checked for prompt redeposition and are discarded immediately if they are redeposited. A compilation of available sputter models can be found in Subsec. 3.3.1.1.

### 3.2.5 Transport

The transport section introduces the concepts solving the transport equation. As EIRENE was initially developed for neutral transport simulations we start with 'Neutral Transport' and then describe the 'Ion Transport' implemented by the Simple Follow Ion Model (SFIM) and the Trace-Ion Model (TIM).

#### 3.2.5.1 Neutral Transport

Given a particle EIRENE samples the free flight path  $L$  from an exponential distribution with the mean free path  $\lambda(\vec{r}, \vec{v}) = \frac{\vec{v}}{\nu(\vec{r}, \vec{v})}$  determined by the particle velocity  $\vec{v}$  and the total collision frequency  $\nu$ . The inverse cumulative distribution function  $F(L)$  is used to sample the free flight length  $L$ .

$$F(L) = 1 - \exp \left[ - \int_0^L \frac{\nu(\vec{r}, \vec{v})}{\vec{v}} dl \right] \quad (3.5)$$

The actual calculation of  $L$  is done by solving

$$\int_0^L \frac{\nu(\vec{r}, \vec{v})}{\vec{v}} dl = \ln [R] \quad (3.6)$$

where  $R$  is a random number on  $[0,1]$ .

EIRENE computes the distance to a variety of possible events – collision with a geometrical surface, a time surface<sup>2</sup> or a grid cell boundary. Given that all distances are larger than  $L$  the particle is advanced  $L$  along  $\vec{v}$  and then undergoes a collision event from the reactions (Block 4). Otherwise the particle is stopped or surface collision routines are called (c.f. Subsec. 3.2.6.2). In case of a grid cell boundary collision the tracking is continued after adapting the  $\nu$  value, which is assumed constant on a grid cell. If the

---

<sup>1</sup> Debye sheath acceleration and modification of the ratio  $E_{\perp}/E_{\parallel}$  is accounted for.

<sup>2</sup> Time is considered as a coordinate and can be bound in EIRENE input Block 13.

weight of a particle is smaller than a user-specified weight limit, the particle may be stopped by EIRENE and the simulation loop is started with a new particle[90].

### 3.2.5.2 Ion Transport

#### Simple Follow Ion Model (SFIM)

Ion transport is complicated by the presence of a magnetic field and requires a more sophisticated treatment. The Simple Follow Ion Model in EIRENE does exactly the same as the neutral tracing routine, except for two additional procedures. First, the particle trajectory is determined by the magnetic field line, which is assumed fixed on the entire grid cell. The actual velocity is simplified in a parallel velocity  $\vec{v}_{\parallel}$  of the gyrocenter motion and a perpendicular velocity of the gyration. A gyrophase angle – hence the direction of the perpendicular velocity – is sampled if a full velocity vector is needed, e.g. in the sheath acceleration or the sputtering routine. Second, a thermalization routine in the Langer approximation is included in order to describe energy equilibration. The collision frequency  $\nu_{\Delta E}$  is fixed.

$$\nu_{\Delta E} = \sum_{i=ions} 8.8 \cdot 10^{-2} n_i T_i^{3/2} \quad (3.7)$$

where  $n_i$  is given in  $m^{-3}$  and  $T_i$  in  $eV$ . This process is not treated as a collision in the reaction sense (Block 4), but rather carried out directly in the transport kernel. It does not interrupt the tracing routine and therefore is called a pseudo-collision. The old thermalization model represents an exponential decay of the kinetic energy difference between the background plasma and the traced particle, assuming  $E_{kin} = 3/2T$ . No isotropization is implemented ( $v_{\parallel}/v_{\perp} = const.$ ). A BGK-thermalization process has been implemented as part of this work in order to improve thermalization and to account for isotropization in the SFIM. It is described below in Sec. 3.3. The BGK-approximation replaces the Langer approximation. A BGK-thermalization event is also treated as a pseudo-collision. The SFIM has been and is most frequently used in the static approximation for very short-lived ions. Ions are stationary (spatial) in the static approximation.

#### Trace Ion Module (TIM)

The TIM is based on the structure of the former SFIM. The improved ion model was built from the model of the former transport code DORIS by D. Reiser at FZJ[8; 9]. The main difference between the SFIM and the TIM is an improved description of the guiding center motion. The TIM introduces an additional time step, we call TIM-time step, in order to follow the magnetic field line. Electromagnetic fields are no longer assumed be constant on an entire cell (direction and strength). Each TIM-time step the parallel velocity is recalculated, including the mirror force effect and corrected with the  $\vec{E} \times \vec{B}$ ,  $\nabla B$  and the curvature drift velocity. Field variations inside a cell are now accounted for by applying a finite element interpolation scheme. The particle is displaced linearly in the direction of the velocity vector. An update to the TIM, created during the work on this thesis and described in Subsec. 3.3.1.4, is the introduction of an additional perpendicular velocity. This velocity describes radial diffusion with a constant, user-supplied diffusion coefficient  $D$ . A second main difference between SFIM and TIM is the replacement of the crude thermalization model of the SFIM by a full Fokker-Planck description in velocity space. Again the thermalization is considered as a pseudo-collision. The Fokker-Planck model describes temperature equilibration and velocity isotropization. It also includes

the description of thermal forces. The TIM is described extensively and tested in [6]. The separate TIM input file enables the user to scale drift and mirror force effects with a prefactor, to set a radial diffusion coefficient and make various adjustments to TIM parameters. The TIM-time step, collision operator flags (average D, 13 moments-correction, included species for collisions) and thresholds additionally to some other model flags can be set[5]. Some problems with the TIM transport remain. We refer to Subsecs. 3.3.1.5 and 4.1.1.

### Future Ion Transport

A future additional method to solve the Fokker-Planck collision operator is currently developed at Forschungszentrum Jülich. Swarm Monte-Carlo techniques will be used. Many binary collisions of followed particles with ions sampled from the background plasma are simulated in pseudo-collisions. It has to be determined whether this technique produces comparably accurate results using similar computational resources.

Aside from generation and transport of particles there is one last ingredient for a complete description – particle reactions in EIRENE. EIRENE features a rather complete and easily modifiable set of reaction types.

## 3.2.6 Reactions

### 3.2.6.1 Plasma-Particle Interactions

EIRENE can include a multitude of plasma-particle interactions, either chemical or physical. Two reaction types are distinguished. A first type are inelastic reactions. For these the user has to supply the particle species and reaction rates, cross sections, etc.. A second type of reactions are elastic reactions like thermalization. The focus is set on the employed electron impact reactions (ionization and recombination) of tungsten and the thermalization of simulated particles.

### Electron Impact Reactions

As explained in Subsec. 3.2.5 EIRENE decides on the occurrence of particle reactions with respect to the accumulated free flight length. If a reaction occurs, EIRENE decides, via random number decisions, which reaction the particle is actually subject to. In the presented work only electron impact ionization and radiative recombination are included<sup>1</sup>. The interval  $I = [0,1]$  is split in two parts with  $A = [0,x]$  and  $B = ]x,1]$ , where  $x$  is defined by

$$x = \frac{p_{ion}}{p_{ion} + p_{rec}} \quad (3.8)$$

A random number  $R$  is samples from  $I$ . For  $R \in A$  the particle is ionized, while  $R \in B$  implies a recombination. The probabilities are evaluated at the start-up of EIRENE, depending on the plasma background parameters and the supplied data for the reaction rates.

In a reaction the particle species is set according to the reaction card in Block 4 in

---

<sup>1</sup> Both reactions are referred to as electron-impact (EI) reaction in EIRENE.



the EIRENE input. The particle properties ( $E$ ,  $v_{\parallel}/v_{\perp}$ , etc.) are sampled according to the type of collision event and conservation laws. The energy and momentum exchange between particle species as well as the particle sources are stored. Multiple possible reactions are taken care of by splitting the interval  $I$  further into smaller subintervals. Even excitation processes can thus be treated properly.

### Fokker-Planck Interaction (TIM)

Apart from collisions in the sense of input Block 4, there is a pseudo-collisions in the tracing routine. The Fokker-Planck operator describes the effect of elastic Coulomb collisions with background particles, causing thermalization and thermal and frictional forces[8; 9]. The present EIRENE solves the kinetic equation in the Fokker-Planck form, Eq. (2.20). EIRENE uses stochastic equivalence of Eq. (2.20) to Langevin methods, which are solvable by Monte-Carlo methods. The drift motion and the stochastic motion, represented by the collision operator, are split as explained in [6, p.46]. The collision term used in the TIM to describe thermalization is given by

$$\partial_t f|_{col} = -\partial_{v^{\mu}} (K^{\mu} f) + \frac{1}{2} \partial_{v^{\nu} v^{\mu}}^2 (D^{\nu\mu} f) \quad (3.9)$$

where  $D^{\nu\mu}$  is the diffusion tensor

$$D^{\nu\mu} = g^{\gamma\mu} g^{\nu\eta} \left( \partial_{v^{\mu} v^{\eta}}^2 \Psi - \Gamma_{\mu\eta}^j \partial_{v^j} \Psi \right) \quad (3.10)$$

and  $K^{\mu}$  is the drift vector

$$K^{\mu} = g^{\mu\nu} \partial_v^{\nu} \Phi - \frac{1}{2} \Gamma_{\gamma\nu}^{\mu} D^{\nu\mu} \quad (3.11)$$

with the Rosenbluth potentials  $\Psi$  and  $\Phi$ [9] and the Christoffel symbol of second kind  $\Gamma$ . The diffusion and drift coefficients in guiding center coordinates are derived in [6, p.34]. They are summarized here.

$$K^1 = \mu L^{ab}, \quad K^2 = \mu L^{ab} \partial_{v_{\perp}} \Phi + \frac{1}{2} L^{ab} \frac{1}{v_{\perp}^2} \partial_{v_{\perp}} \Psi \quad (3.12)$$

$$D^{11} = L^{ab} \partial_{v_{\parallel}}^2 \Psi, \quad D^{12} = D^{21} = L^{ab} \partial_{v_{\parallel} v_{\perp}}^2 \Psi, \quad D^{22} = L^{ab} \partial_{v_{\perp}}^2 \Psi \quad (3.13)$$

where

$$L_{ab} = \frac{n_B q_B^2 q_a^2 \ln \Lambda_{aB}}{4\pi \epsilon_0^2 m_a^2} \quad (3.14)$$

The implications made by and tests of this collision operator can be found in [6, p.35-38 & 59-74]. It is shown that the collision operator leads to a proper temperature equilibration, temperature isotropization and Maxwellianization in the case of carbon simulations.

### 3.2.6.2 Plasma-Wall Interactions (PWI)

Plasma-wall interactions are organized sequentially in EIRENE. An impinging particle is first subject to sheath acceleration. EIRENE takes into account the in-/decrease of the kinetic energy as well as a change in  $v_{\parallel}/v_{\perp}$ . The sheath acceleration leads to incident

angles closer to normal incidence than without the change in  $v_{\parallel}/v_{\perp}$ . EIRENE then calculates the sputtering yield (physical & chemical) and stores the sputtered particle for later tracing. The impinging particle is tested for absorption and a variety of different reflection models on different surface types (transparent, semi-transparent, reflecting) can be applied afterwards. Finally the parameters of a reflected particle are sampled from user-specified distributions. The tracing then continues in the transport routines with the weight-adapted particle.

### Sputtering

Sputtering is one of the most important PWI in tungsten devices. Sputtering processes in EIRENE were covered already in Subsec. 3.2.4.

### Reflection & Absorption

Reflection and absorption are distinct processes in EIRENE. The absorption is tested by the comparison of a user-specified absorption probability (EIRENE input Block 3 & 6) to a random number.

Reflection is divided into two different kinds of reflections – thermal reemission or fast particle reflection. Both models can separately apply to each individual particle species (EIRENE input Block 4). Thermal reemission ‘reflects’ the particle from the incidence point with a ‘temperature’ (kinetic energy) sampled from a Maxwellian and with a cosine velocity distribution around the surface normal. The temperature is either taken from the surface itself or from the plasma in front of it. The reflection probability is user-specified in the input Block 6.

The employed fast particle reflection model is the most ‘recent’ model from Eckstein and Heifetz (1986) with more recently updated TRIM data[55]. The reflection probability and the parameters of the reflected particle are sampled according to reflection coefficients described in Chapter 2. For fast particle reflection the projectile-target combinations shown in Tab. 3.1 are available[55].

Target	Projectile
<b>Be</b>	D, Be, Ne
<b>C</b>	H, D, T, He, Be, B, C, Ne, Al, Si, Cr, Fe, Cu, Mo, W
<b>Fe</b>	H, D, T, He, C, Si
<b>Cu</b>	H, C, Si
<b>Mo</b>	H, D, T, He, C, Cr, Mo
<b>W</b>	H, D, T, He, C, W

**Table 3.1:** Sample of target-projectile combinations included in EIRENE reflection model[55].

Coefficient scaling is applied for unknown projectile-target combinations. The Thomas-Fermi energy  $E_{TF}$  – a natural parameter in reflection and physical sputtering relying on cross-sections and nuclear stopping power – is used to search for the closest existing dataset.

$$E_{TF} = 30.74 \frac{m_a + m_b}{m_b} q_a q_b \left( q_a^{2/3} + q_b^{2/3} \right)^{1/2} \quad (3.15)$$

The quantities are given for the projectile  $a$  and the target material  $b$ . The TRIM-dataset with the ratio  $E_{TF}^{a,b}/E_{TF}^{set} = \frac{1}{f_{red}}$  closest to one is taken to obtain reflection coefficients.

EIRENE rescales the incident energy according to

$$\hat{E} = E f_{red} \quad (3.16)$$

carries out the reflection for the selected dataset and rescales the energy of the reflected particle back. In general this procedure is quite robust for unknown projectile-target combinations unless the mass differences between the actual combination and the used dataset combination is very large. The scaling then might produce unsuitable extrapolations. With tungsten being the simulated impurity in the presented thesis, it was necessary to include new TRIM-data for several tungsten based combinations to avoid extrapolation errors.

### 3.3 EIRENE Updates

This section describes the new routines developed during this thesis, which improve EIRENE's capability to handle tungsten as impurity species. Necessary preparations in order to perform EIRENE simulations, such as providing the plasma background, are presented. All presented routines and preparation procedures were developed in the course of this thesis, even if formulated in a passive voice.

#### 3.3.1 Upgrades & New Routines

Simulating tungsten ions as impurity for the first time in EIRENE, we reconsidered several models and assumptions usually applied in the EIRENE code. Several necessary improvements and updates were found pending. With tungsten, sputtering – most important self-sputtering – is one of the main sources of the impurity content in the plasma. Therefore the most accurate model available should be employed to ensure that particle sources, as starting point of any simulation, are properly described. A phenomenon related to tungsten sputtering is prompt redeposition, effectively reducing the sputtering yield by up to 90%. The sputter model was updated from the Eckstein 1993 to the 2007 data given in [54]. EIRENE now includes state-of-the-art sputtering yields, respecting an angular dependence. In addition a prompt redeposition scheme for sputtered particles was introduced. This routine corrects for prompt redeposition with respect to local plasma parameters and local geometry.

Up to now the PROUSR-coupling (c.f. Subsec. 3.3.2.3) used to supply the plasma background to EIRENE did not include the possibility to specify the electric field of the plasma by a potential. All the electric field components had to be supplied instead. An update to the coupling routines lifted this restriction and enables EIRENE to calculate a two dimensional electric field in the poloidal plane from an external potential by means of finite element interpolation.

The major drawback of the TIM is the lack of finite gyroradius effects and thus spatial diffusion. Therefore the most dominant transport mechanism – anomalous transport usually described by a diffusion coefficient – could not be incorporated in simulations until now. The disability to simulate spatial, and thus anomalous diffusion renders EIRENE largely unsuitable for predictive ends or experiment validation in realistic plasma sce-

narios. Therefore a simple mock-up model for perpendicular diffusion was created to have EIRENE ready for realistic plasma simulations. Due to the geometry handling in EIRENE and the use of the track-length estimator it is not yet fully clear whether this model is fully operational. Another module simulating perpendicular diffusion is currently in development at FZJ.

The original EIRENE 2010 version already has high demands on computational resources, because the ion-tracing – forcing the introduction of a TIM-time step – make calculations costly. Both, the new prompt redeposition and the diffusion routines increase the consumption of computational resources further. As EIRENE 2010 was not parallelized with the TIM included, a renewed parallelization of EIRENE was necessary. The parallel EIRENE was adapted to the inclusion of the TIM. The adaption was done along with many minor bug fixes, which became necessary in the setup of EIRENE at IPP.

A update to the SFIM was the creation of a simple BGK-thermalization routine within EIRENE. The update now guarantees the isotropization of the velocity during thermalization.

### 3.3.1.1 Sputtering

The sputtering parameter database was updated and the code was adapted. The more recent fit parameters from 2007, presented in Subsec. 2.1.1, are now incorporated in EIRENE. The most recent model is applied whenever fit parameters are available. An automatic fall-back to older models or a scaling law is implemented[4; 52]. The new sputter model was tested. The code validation also provides an estimation of the effects of the performed update.

#### Validation

The sputtering yield calculated by EIRENE in a given, fixed geometry, shown in Fig. 3.1, with mono-energetic, neutral atoms as impinging particles was compared to the theoretical sputtering yield, directly calculated with Eqs. (2.7-2.8). Neutral atoms were taken as impinging particles in order to exclude sheath acceleration effects. The numerical results are in accordance with theoretical expectations. A minor deviation at small incident angles was traced back to round off errors in a cosine expression, which is error-prone at small angles. Figure 3.2 shows the ratio of the old and new sputtering yields (Eckstein 2007 and Eckstein 1993). The effect of the update on the energy dependence is visible at 0 angle. Its effect on the angular dependence is also evident. Especially the self-sputtering yield of tungsten is enhanced for oblique angles at low energies. The maximum increase of the sputtering yield is a factor of 8.5.

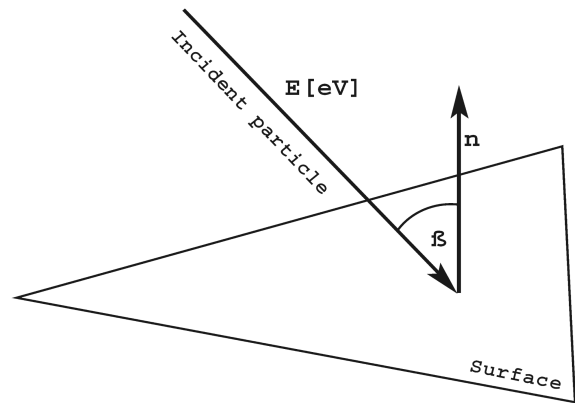


**Figure 3.1:** Test geometry.

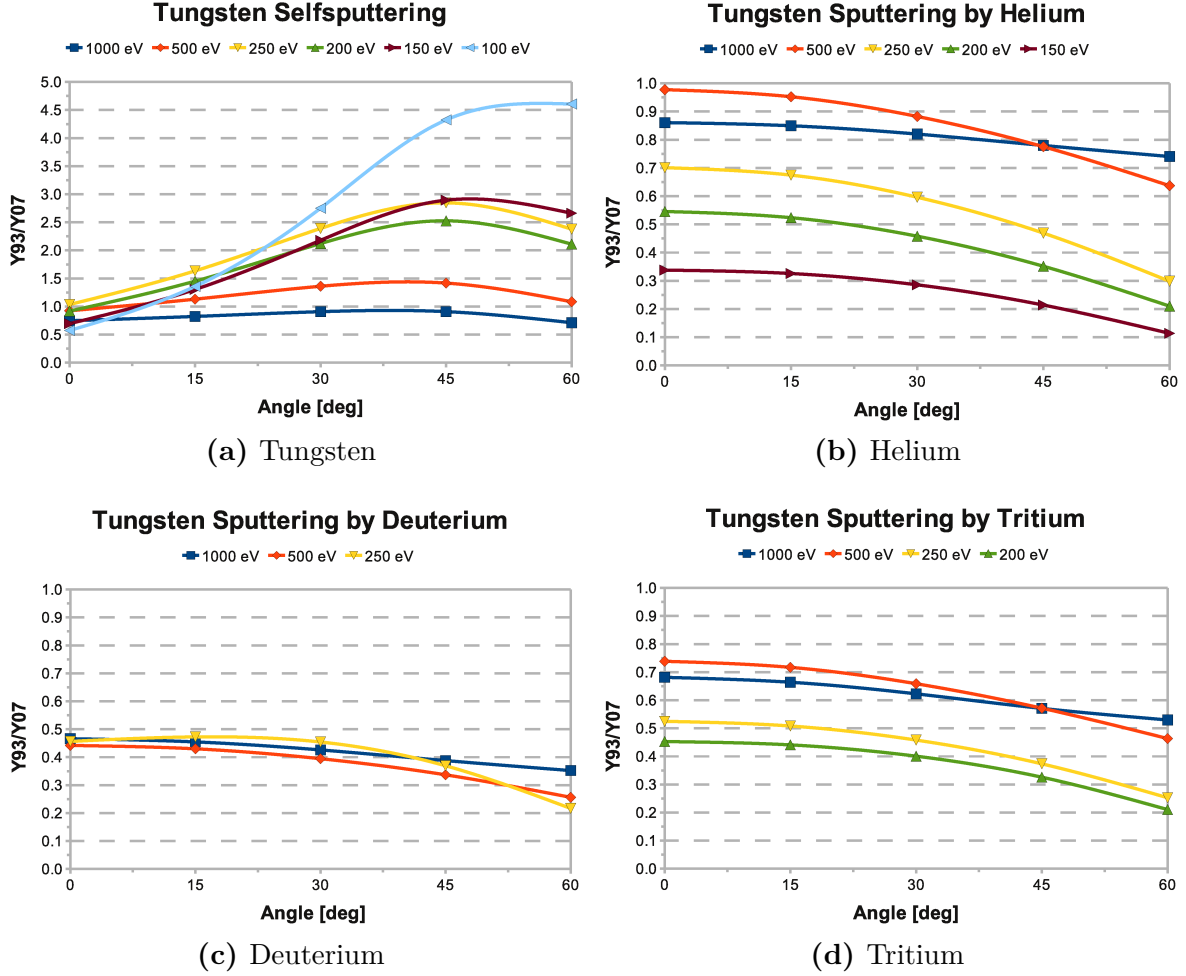


**Figure 3.2:** Ratio of the angular dependence between the sputtering yield of the '93 and the '07 model by Eckstein for different projectiles.

### 3.3.1.2 Prompt Redeposition

Prompt redeposition can have an important impact on net tungsten erosion. Especially in discharges with high edge densities, exceeding  $5 \times 10^{19} m^{-3}$ , in front of the target it critically determines the effective sputtering yield. Gross sputtering yields can be reduced by several orders of magnitude. It is thus desirable to take into account the suppression of sputtering by prompt redeposition in EIRENE. Until now EIRENE determined the sputtering yield and stored a sputtered particle for further tracing. The new prompt redeposition routine tests for redeposition beforehand and discards the sputtered particle if it would be redeposited.

At first the ionization length  $L$  is sampled from an exponential distribution with a mean free path to ionization  $\lambda$ .  $\lambda$  is calculated according to plasma parameters in front of

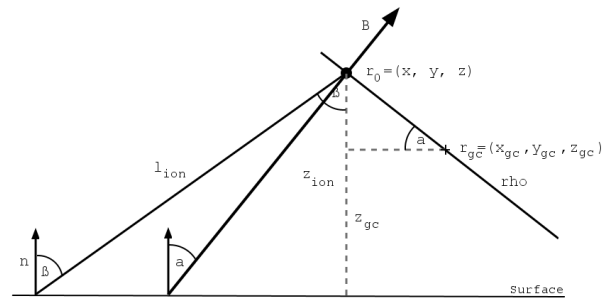


**Figure 3.3:** Geometry of the prompt redeposition routine setup.

the considered surface. In the current implementation the reaction rate, determining  $\lambda$ , is the sum of the reaction rates of all possible inelastic reactions, not only ionizations. Our current EIRENE setup includes only electron impact reactions. Hence, for neutral tungsten  $\lambda$  is determined by the reaction rate of the first ionization<sup>1</sup>.

$$l = -\lambda \lg [R] \cos [\text{Arc} (\vec{n}_S, \vec{v}_{SPT})] \quad (3.17)$$

where  $R$  is a uniformly distributed random number on the interval  $[0,1]$ . The cosine accounts for the fact that only the perpendicular motion along the surface normal  $\vec{n}_s$  with velocity  $\vec{v}_{SPT}$  is relevant for prompt redeposition. After retrieving  $L$  the position of the gyrocenter  $\vec{r}_{gc} = \vec{r}_0 + \vec{\varrho}$  is calculated by adding the position vector of the ionization event  $\vec{r}_0 = \hat{v}_{SPT} l_{ion}$  and the gyroradius  $\vec{\varrho} = \frac{v_{\perp}}{\omega_c} \hat{v}_{SPT} \times \hat{b}$  (c.f. Fig. 3.3). Comparison of the projection of  $\vec{r}_{gc}$  onto the surface normal ( $z_{gc}$ ) with the gyroradius  $\varrho$  decides about whether or not the particle is redeposited. If  $z_{gc}$  is smaller than  $\varrho$  the sputtered particle will hit the surface during its first gyration and is assumed to be redeposited. If not, the particle tracing is resumed. The implicit assumption of a magnetic field parallel to the surface is made by comparing  $\varrho$  and not its projection on the surface normal to  $z_{gc}$ . It is justified by the fact that the magnetic field hits the target usually at oblique angles in fusion devices.

The sputtered and redeposited particle fluxes that were simulated with the new routine on a given background for a fixed projectile influx compare well to results of the analytical model described in Subsec. 2.1.1.3. A result of such a comparison is shown in Tab. 3.2.

<b>EIRENE:</b> $P_{mean} = \frac{\lambda_{MEP}}{r_g} = 2.54$		#/Fluxes	Fractions
<b>Events</b>	<i>Sputtered</i>	32484	<b>62%</b>
	<i>Redeposited</i>	20216	<b>38%</b>
<b>Fluxes</b>	<i>Sputtered</i>	7.85E-2 A	<b>59%</b>
	<i>Redeposited</i>	5.38E-2 A	<b>41%</b>
<b>Analytical model:</b> $P_{fix} = 2.55$			
	<i>Redeposited</i>		<b>37%</b>

**Table 3.2:** Comparison of redeposited and sputtered fractions calculated with the analytical model[58] and simulated with the updated EIRENE (events and associated fluxes).

The current redeposition model incorporates some limitations. Otherwise an unnecessary complex implementation would have been needed to fit the procedure into the code framework. The following effects are not taken into account:

- Any change of the plasma parameters – spatial or timely – during the first gyration is neglected. No geometrical check for the boundaries of the surfaces or the grid cell is executed. Due to usually small gyroradii of tungsten ( 5mm) and comparably bigger cell sizes ( 30mm) the effects should be negligible.
- Vertical motion along the magnetic field line during the first gyration is neglected. This leads to an overestimation of the prompt redeposition. With regard to usually oblique angles of incidence of magnetic field lines this effect should be small.

<sup>1</sup> Care must be taken in future runs with different reaction cards in EIRENE.

- Acceleration in the sheath ( $l_{Debye} \approx 2,5mm$ ) is not accounted for. This effect should be taken care of in future updates as it might increase the yield substantially.
- Further ionization during the first gyration is neglected leading to an overestimation of redeposition. The effect of multiple ionization events should be small enough to be negligible in fusion plasmas.
- Sputtering by the impact of the redeposited particles is neglected leading to an underestimation of the net sputtering yield. It should be included in future updates as it might lead to sputter cascades, especially in combination with sheath acceleration effects.

### 3.3.1.3 Electric Potential

The TIM provides the possibility to include ion drift motion like the  $\vec{E} \times \vec{B}$  drift. However, to be able to calculate the drift contribution to impurity transport one has to supply the most appropriate electric field available. Unfortunately the generation and the structure of the electric field in fusion plasmas is still not fully understood and there are no simple analytical models. The electric field has to be supplied by external measures – either experimental measurements or numerical simulations. Up to now the PROUSR-coupling routines of S. Wiesen[4, p.185] were employed to supply the Cartesian electric field components directly. However, B2.5 calculates the electric potential instead of the electric field. The PROUSR-coupling routines were modified in order to be able to read and process both an electric potential or explicit Cartesian electric field components. In case of a user-specified electric potential the electric field is derived from the potential in EIRENE. The potential is linearly interpolated to cell corners and subsequently the derivatives with respect to the Cartesian coordinates  $R$  and  $z$  are calculated. The interpolation and the determination of the derivatives are performed by finite element methods written by J. Seebacher. Finally, the electric field is stored in an array.

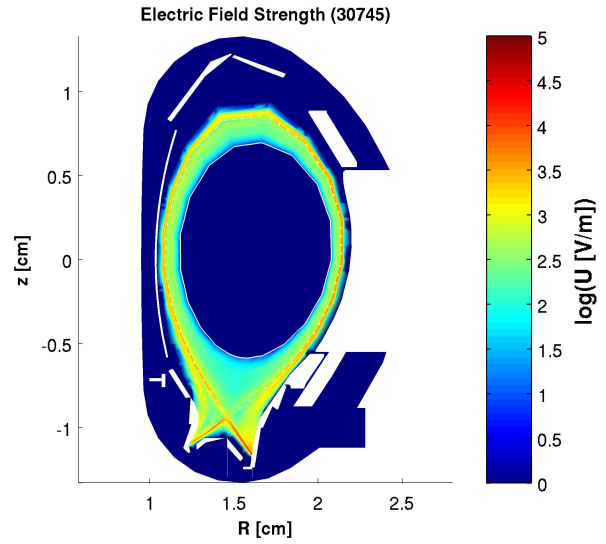


**Figure 3.4:** Electric field calculated from a potential for SOLPS simulation #31199.

### 3.3.1.4 Perpendicular Diffusion

One of the major drawbacks of the TIM is the lack of spatial diffusion in the Fokker-Planck operator. Banana transport is the only neoclassical transport that EIRENE simulates, because the gyroradius is effectively approximated to be of zero length for all transport effects (c.f. Chapter 2.2). This eliminates classical, Pfirsch-Schlüter and anomalous transport in EIRENE simulations so far. Reasonable benchmarking with

other codes, which mainly describe transport with a spatial diffusion coefficients, was thus very difficult. Experimental data is also dominated by anomalous transport effects and a code validation with the original EIRENE 2010 against the experiment is unlikely to be successful.

In order to overcome this enormous limitation and to make EIRENE fully operational for ion-tracing a very simple mock-up model for spatial diffusion has been created. Due to the complicated geometry handling in EIRENE the diffusion was introduced as an additional pseudo-drift velocity. However, this might lead to a conflict with the use and the definition of the employed track-length estimator. This issue is not yet finally settled and will be left unanswered for the time being as the general proof of the track-length estimator is also pending.

In order to implement spatial diffusion in EIRENE the existing drift routines were used as a mean to generate spatial displacement. Using the fixed or precalculated TIM-time step the displacement length in radial direction is calculated such that it result in a given diffusion coefficient in a random-walk picture. The diffusion coefficient is user-specified in the TIM input file in units of  $cm^2/s$ . The random-walk diffusion coefficient  $D$  can be transformed to

$$\Delta x = \sqrt{D \Delta t} \quad (3.18)$$

where  $\Delta x$  is the radial displacement and  $\Delta t$  is the TIM-timestep. The radial direction is determined by sampling a random vector  $\vec{v}_r$  in three dimensional space and subsequently taking the cross-product with the magnetic field vector. The result  $\vec{v}_D = \vec{v}_r \times \vec{B}$  is normalized to unit length  $\hat{v}_D$ . The actual displacement length  $\Delta x'$  is sampled from an exponential distribution with mean  $\Delta x$ . It is used to compute an effective diffusion velocity  $\vec{v}'_D$  resulting in a displacement of  $\Delta x'$  during the TIM time step  $\Delta t$ .

$$\vec{v}'_D = \frac{\Delta x'}{\Delta t} \hat{v}_D = -\frac{\Delta x}{\Delta t} \lg[R] \hat{v}_D = \sqrt{\frac{D}{\Delta t}} \lg[R] \hat{v}_D \quad (3.19)$$

$\vec{v}'_D$  is added to the standard TIM drift velocity if it is larger than a numerical precision limit of  $10^{-32}$  m/s. A total tungsten density for a simulation with pure diffusion is shown in Fig. 3.5. The source region of the released tungsten is indicated by an arrow at the outer target near the strike-point.

Please note the fact that the current implementation of the perpendicular diffusion is a preliminary mock-up model. It is not yet sufficiently tested and/or benchmarked nor is the soundness of the approach proven theoretically. However, the code works as intended with benchmarks pending. The current routine is very expansive regarding computational time. It increases the need approximately twofold. Amongst other reasons this lead to the necessity to renew the parallel computation ability of EIRENE.

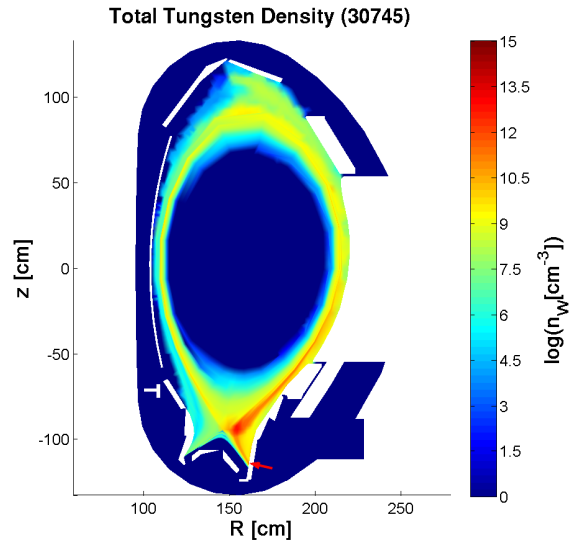


**Figure 3.5:** Tungsten diffusion profile for a localized tungsten source with  $D = 1 m/s^2$ .



### 3.3.1.5 Renewed Parallelization of EIRENE

The EIRENE version including the TIM is confronted with several challenges regarding the necessary computational time for simulations. The structure of the TIM, with a recalculation of the velocity after every TIM-time step, makes it easy to introduce additional features like radial diffusion, but prevents efficient computation. As a non-field aligned transport code EIRENE suffers from an inherent numerical outward drift for ions, which can only be kept small by the use of costly, small TIM-time steps. Additionally in our simulation long-living tungsten ions can consume large amounts of computational time improving the statistics only in parts of the grid, where the specific ions species exists. Even a limitation of the simulated physical time to 10 ms by the introduction of a time surface (input Block 13) is only reducing the strain on computational requirements. Hence the ability of former EIRENE versions of parallel calculations have to be restored. This subsection first shortly discusses the numerical drift effects and the related accuracy issues to demonstrate the importance of small TIM-time steps. Then the results of our renewal of the parallelization of EIRENE are presented.

#### Numerical Drift

Numerical drifts are an inherent feature of non-field aligned grids in ion-tracing. These can be largely suppressed – not mitigated completely – by an appropriately small TIM-time step depending on field line geometries like curvature. Time steps as little as  $10^{-12}$  s have to be used to get results that match the results of field aligned geometry code<sup>1</sup>. Another important consideration in the choice of the TIM-time step is the computational time at hand. Currently the non-parallelized version of EIRENE restricts the time step to  $10^{-7}$  s to ensure 'sufficient' statistics in a simulation running for six days. A crude estimate of the numerical outward drift is derived in the following. The linear displacement  $\Delta l$  during a fixed TIM-time step  $\Delta t$  for a given kinetic energy  $E$  of a particle of mass  $m$  is

$$\Delta l = v \Delta t = \sqrt{\frac{2E}{m}} \Delta t \approx 1023.6 \times \sqrt{E [\text{eV}]} \Delta t \quad (3.20)$$

The local curvature of the magnetic field is given by the curvature radius  $R_B$

$$R_B = \frac{1}{|(\vec{b} \cdot \vec{\nabla}) \cdot \vec{b}|} \quad (3.21)$$

where  $\vec{b}$  is the normalized magnetic field vector. The curvature leads to an artificial radial displacement  $\Delta r$  from the magnetic field line of

$$\Delta r = R_B (\sec [\alpha] - 1) \quad \text{with} \quad \alpha = \arctan \left[ \frac{\Delta l}{R_B} \right] \quad (3.22)$$

Expanding the arc tangent and the cosine to first order one gets  $\Delta r \propto \Delta t^2$ . The quadratic proportionality explains the critical dependence of the numerical drift on the timestep size. Table 3.3 shows a sample of numerical drift displacements.

---

1 Private Communication with Detlev Reiter at Forschungszentrum Jülich

$T_i$ [eV]	$\Delta r$ [mm]	$\Delta l$ [mm]
10	0.001	0.324
100	0.010	1.024
1,000	0.105	3.236

**Table 3.3:** A sample of numerical drift induced radial displacements for a TIM-timestep of  $10^{-7}$  s at kinetic energies of 10, 100 and 1000 eV for tungsten particles with an assumed curvature radius of 0.5 m (AUG minor radius).

### Parallelization

In principle EIRENE is ideally fitted to be processed in parallel – each process follows particle trajectories on the previously distributed plasma background independently. No computational expansive intermediate interchange of calculation results of individual processes is necessary. The individual processes finish independently after having consumed a preset computational time or having reached a preset particle generation number limit. The results of all processes are gathered and merged at the end of the calculations. The old EIRENE version without the TIM was fully parallelized. However, parallel computation was not yet working in the original EIRENE 2010 version, which includes the TIM. We adapted the parallel computation routines and parallel EIRENE 2010 is now available. The speed-up by parallelization was tested with respect to the time consumed by a single, simulated particles. The test was carried out on the Linux Cluster of IPP. The results are given in Tab. 3.4. However, the preset computational time of 600 s is very short and the overhead of the initialization is still manifest in these results.

# CPU	Comp. Time [s]	# Particles	Time/Particle [s]
1	740	5	148
8	1500	43	35
16	1700	79	21
64	2500	458	5

**Table 3.4:** Computational speed-up of parallelized EIRENE.

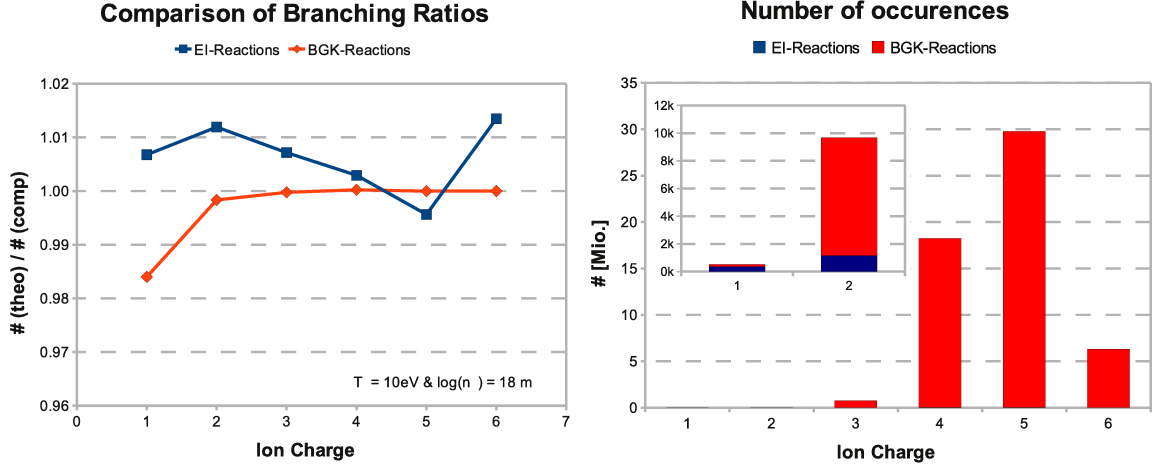
#### 3.3.1.6 BGK-thermalization

For ions traveling in a background plasma it is important to describe the Coulomb interaction of the test particles with the background plasma leading eventually to thermalization. To get rid of the limitations of the Langer approximation (c.f. Subsec. 3.2.5.2), we introduced a thermalization routine in BGK-approximation into EIRENE. The BGK-approach approximates the Boltzmann collision term by

$$\frac{\partial f_a}{\partial t}|_{coll} \approx \frac{f_a^1}{\tau} \quad (3.23)$$

Thermalization of two plasma components without relative drift can be describes by[91, p.36]

$$\frac{dT_a}{dt} = \sum_b \bar{\nu}_\varepsilon^{a|b} (T_b - T_a) \quad (3.24)$$



(a) Branching ratios of electron-impact and BGK-thermalization events

(b) Absolute numbers of electron-impact and BGK-events

**Figure 3.6:** Validation of the BGK-thermalization model. EI are electron impact reactions included in the current EIRENE runs, whereas BGK are thermalization routine calls.

with the frequency

$$\bar{\nu}_e^{a|b} = 1.8 \cdot 10^{-19} \frac{Z_a^2 Z_b^2 n_b \lambda_{ab} (m_a m_b)^{1/2}}{(m_a T_b + m_b T_a)^{3/2}} \quad (3.25)$$

Full thermalization is assumed after the first BGK-collision occurred. The collision time is computed from an exponential distribution with mean collision frequency  $\nu$ . Thermalization is achieved by sampling new velocities  $v_x$ ,  $v_y$ ,  $v_z$  from the background Maxwellian, thus changing the ratio  $v_{\parallel}/v_{\perp}$  and eventually obeying temperature isotropization.

The implementation was tested numerically. Theoretical expectations of the branching ratio for a given background density and temperature were met (c.f. Fig. 3.6). The background parameters taken for the test were  $n_e = 10^{12} \text{ cm}^{-3}$  and  $T_e = 10 \text{ eV}$  in a toroidal magnetic field of  $B_t = 1 \text{ T}$  ( $B_{r/z} = 10^{-15} \text{ T}$ ). Figure 3.6a shows the branching ratio for certain ionization stages and Fig. 3.6 shows the absolute number of events. The deviations of the branching ratio for lower ionization stages can be explained by insufficient statistics and the probabilistic scatter of a Monte-Carlo process for sampling the reaction type. Thermalization and isotropization were in fact achieved. The mean kinetic energy of test-ions was 10 eV and was distributed 1/3 to 2/3 on parallel and perpendicular kinetic energy on average. A remaining discrepancy is found in the BGK-collision frequency, which is about half of the theoretically expected value as shown in Fig. 3.7. This is not yet understood and further examination is necessary.

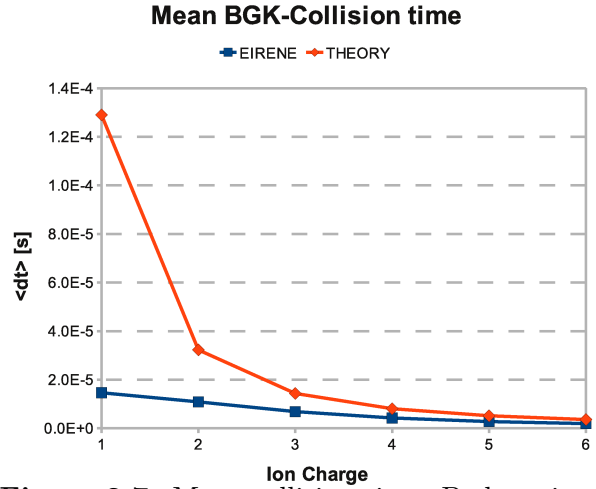


**Figure 3.7:** Mean collision time. Bad statistics (c.f. Fig. 3.6b) at low charge states lead to overestimated deviations.

### 3.3.1.7 Bug Fixes

Several bugs and inefficiencies were encountered while working on the code. These were corrected or improved in close collaboration with the team at Forschungszentrum Jülich – especially Detlev Reiter and Petra Börner – and with Josef Seebacher from the University of Innsbruck. The problems included segmentation faults due to pointer errors, insufficient numerical precision for particle tracing in geometry routines, geometry and particle tracing problems and some more errors such as the  $\nabla B$ -drift velocity pointing in the wrong direction.

## 3.3.2 EIRENE Preparations

This section describes the necessary input for EIRENE simulations and presents how the input data was produced – starting with the grid geometry, passing to the magnetic field calculations and finally arrives at the description of the plasma background generation.

### 3.3.2.1 Mesh Generation

Mesh generation is done automatically by two modules of the EIRENE package (TRIA and TRIAGEOM). TRIA takes an existing SOLPS-grid and additional user-supplied information on the geometry of limiting structures and on the coupling interface from input Block 2, 4 and 14. TRIA triangulates the SOLPS-grid and merges the boundaries with the vessel structure according to the input parameters. TRIAGEOM then extends the grid to the vessel structures, merging the two grids at the SOLPS-grid boundary. Figure 3.8 shows an example of such a combined grid. The result of this procedure is an unordered, triangular grid. Three ASCII-files contain all geometrical information needed by EIRENE.

EIRENE input data is to be given as cell centered values. The values are valid all over the cell volume in the old EIRENE version without the TIM. In the new EIRENE version including the TIM the triangles are grid elements in a finite element scheme and EIRENE is enabled to use sophisticated Finite Element Methods (FEM) to interpolate the plasma parameters to specific coordinates. The TIM uses plasma parameters given on the triangle corners. Cell centered values are converted to corner centered values by distance-weighted averaging over neighboring cells automatically by EIRENE. FEM-interpolation enhances accuracy considerably and is necessary for B-field interpolation in ion-tracing for example. The FEM-interpolation is used only to determine more accurate electro-magnetic fields. Other background plasma parameters like density or temperature are still valid on whole grid cells. For ion-tracing the most important issue is the following of magnetic-field lines. Therefore these have to be carefully retrieved from experimental or numerical simulation data.

### 3.3.2.2 B-field Generation

The magnetic equilibrium supplied to EIRENE is generated from routine magnetic measurements at ASDEX Upgrade stored in the shotfile system. From this shotfile data the program CLISTE reconstructs the magnetic equilibrium[92; 93]. The magnetic flux function  $\Psi(R, Z)$  of the reconstructed equilibrium is saved in a shotfile. B-field calculations are carried out by a modified ReWrite-Shot(RWS) program. RWS takes a magnetic equilibrium data set  $\Psi$  from CLISTE and calculates the magnetic field for random coordinates inside the equilibrium domain from the flux distribution. In the present work an equilibrium in the \*.geq format was taken as the basis for the magnetic field calculations with RWS. The magnetic signals taken for the B-field reconstruction were measured in the AUG shots specified in Tab. 3.5. The poloidal magnetic field strength  $B_p$  calculated with the magnetic equilibrium of AUG reference shot #23029 is shown in Fig. 3.8.

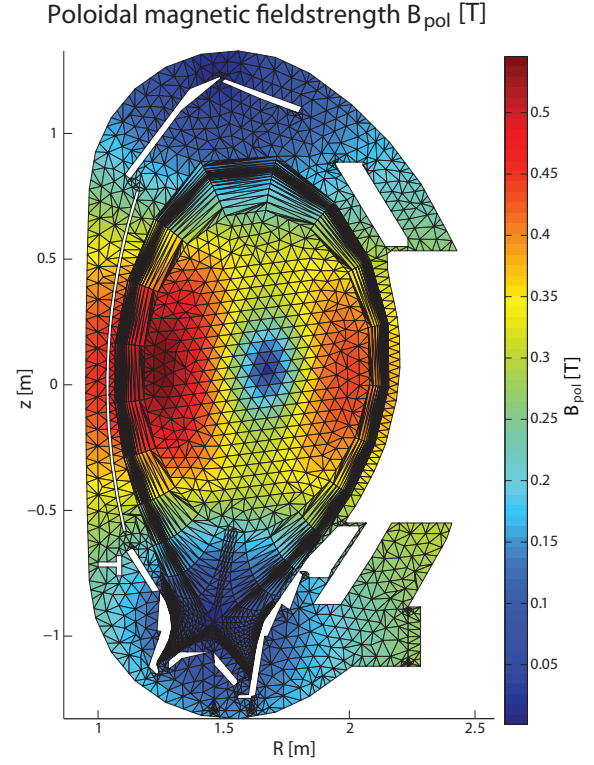


**Figure 3.8:** Poloidal magnetic field strength for the AUG reference shot #23029.

Generator	SOLPS#	Shot#	Shot Time
CLISTE	#30745	#23029	2.5 s
CLISTE	#31199	#23029	2.5 s
CLISTE	#31273	#21372	4.2 s
CLISTE	#31274	#21372	4.2 s

**Table 3.5:** References data for magnetic equilibria reconstruction. SOLPS simulation indices, AUG shot numbers, and the shotfile-based equilibrium times are given.

#### RW-Shot

'ReWrite-Shot' is a small program reformatting several shotfile related information files like magnetic equilibrium files \*.qeg. The original RW-Shot program routinely used in IPP<sup>1</sup> was modified for this thesis. The modified RWS program now does two things to supply the magnetic field. It calculates the toroidal magnetic field from the toroidal magnetic field at the magnetic axis  $B_{t,0}$  and the major radius of the magnetic axis  $R_0$ .

$$B_t(R) = B_{t,0} \frac{R_0}{R} \quad (3.26)$$

<sup>1</sup> Contact: Christian.Konz@ipp.mpg.de

In order to determine the poloidal magnetic field the poloidal magnetic flux  $\Psi$ , given on a fixed regular grid, is first interpolated by spline interpolation to the new irregular EIRENE grid. Then the magnetic field is calculated with the following equations[63]

$$\begin{aligned} B_Z^p &= \frac{1}{2\pi R} \frac{\partial \Psi}{\partial R} \\ B_R^p &= -\frac{1}{2\pi R} \frac{\partial \Psi}{\partial Z} \end{aligned} \quad (3.27)$$

Some care has to be taken in order to avoid confusion with different types of definitions regarding the poloidal flux (factor  $2\pi$ ). To simulate impurity transport in a realistic fusion setup not only the magnetic field has to be supplied to EIRENE, but a background plasma has to be specified too.

### 3.3.2.3 Plasma Background Generation

Using EIRENE in stand-alone mode one has to supply a (fixed) plasma background via the PROUSR-coupling[4, p.185], which is controlled in input Block 5. The plasma backgrounds, used in this thesis, are calculated by SOLPS 5.0. Table 3.6 gives an overview of major plasma characteristics. A sample of important plasma properties is shown in Figs. A.3-A.6 in Appendix A.3. The construction of a plasma background for the present EIRENE version can be split into three different steps, which are now automatically performed by a number of matlab routines created for this work.

SOLPS#	AUG#	Species	Description	$n_{e, \text{Sep}}$
30475	23029	D, T, He, C	L-Mode, el.Pot., no Drifts	$7.8 \times 10^{18} \text{ m}^{-3}$
31199	23029	D, T, He, C	L-Mode, el.Pot., Drifts	$9.5 \times 10^{18} \text{ m}^{-3}$
31273	21372	D, T, He, C	H-Mode, el.Pot., no Drifts	$2.7 \times 10^{19} \text{ m}^{-3}$
31274	21372	D, T, He, C	H-Mode, el.Pot., no Drifts	$3.2 \times 10^{19} \text{ m}^{-3}$

**Table 3.6:** Characteristic features of the different background plasmas, including the SOLPS index in the MDSPLUS database, the AUG shotnumber and details of the simulated discharges.

### SOLPS Grid - MDSPLUS Data

First the SOLPS (Version 5.0) plasma parameters are read from the MDSPLUS-database[94] via a matlab interface routinely used at IPP. The SOLPS data is uniquely identified by SOLPS catalog index numbers – not to be confused with experimental AUG shot numbers. The plasma parameters are subsequently mapped from the rectangular SOLPS mesh to the triangular EIRENE mesh retrieving the necessary information from the SOLPS datatree. Some caution has to be paid to the exact definitions of the individual arrays in the SOLPS datatree as there might be differences for SOLPS and the present EIRENE version. One of these examples is that SOLPS gives all data in SI-units – except for temperature, which is in [eV] – whereas EIRENE uses *cm* instead of *m* and counts fluxes in *A*.

### Construction of Drift Velocities

Drift velocities have to be treated separately. SOLPS gives flows with respect to the magnetic field geometry, while EIRENE is solely depending on toroidal coordinates  $(R, z, \varphi)$ . Table 3.7 gives the definitions of the SOLPS fluxes. Exact reference to the definitions can only be found in the SOLPS code itself and is somewhat difficult to retrieve. The SOLPS manual is not too specific about definitions<sup>1</sup>. Fluxes are converted to EIRENE definitions by projection of the given SOLPS quantities onto the magnetic field lines or the corresponding normal vector. At this stage of the background preparations the SOLPS grid part is complete, but the extended grid has to be assigned appropriate plasma parameters too.

SOLPS structure	Alignment to	
	Flux surface	B-Field
udia(:, :, 0, NPSLI)	parallel to flux surface	perpendicular to B-field
udia(:, :, 1, NPSLI)	perpendicular to flux surface	perpendicular to B-field
ua(:, :, NPLSI)	parallel to flux surface	parallel to B-field

**Table 3.7:** Definitions of SOLPS fluxes

### Extended Grid - Extrapolation

The extended part of the EIRENE grid – not included in the SOLPS grid – can be divided into two different parts. One consists of remote parts of the vessel. No direct (linear) connection to the main plasma exists, e.g. below the baffle dome or behind the heat shield. In these parts the background plasma parameters, except for the magnetic field, are set to the default EIRENE vacuum parameters of  $n_{e/i} = 100 \text{ cm}^{-3}$  and  $T_{e/i} = 20 \text{ meV}$ . The drift velocities are set to zero. In vacuum regions EIRENE suppresses all reactions intrinsically per default. In the second part of the exterior grid, with lines of sight to the SOLPS part, each triangle adopts the plasma parameters of the closest SOLPS-cell. Two further options are available in our setup procedures. The plasma parameters on the second part of the extended grid can either be set to the EIRENE vacuum conditions or equal to the average of the four SOLPS-cell closest by. The inclusion of a decay length in the SOL plasma was neglected to keep the preparations simple.

Simulations of the extreme cases of closest cell extrapolation and vacuum conditions were performed to estimate the impact of the extrapolation scheme. Figure 3.9 shows two identical cases – with the extended grid being set to vacuum conditions (1) or closest cell values (2). The accumulation of tungsten at  $\varrho_p \approx 1.03$  is smeared out for case (2) as would be expected from additional collisions in the far SOL. These collisions also lead to a slightly lower impurity content with a reduced maximum density of case (2) in comparison to the vacuum case (1). Sputtering was not included in these tests.

---

<sup>1</sup> Contact:David.Coster@ipp.mpg.de

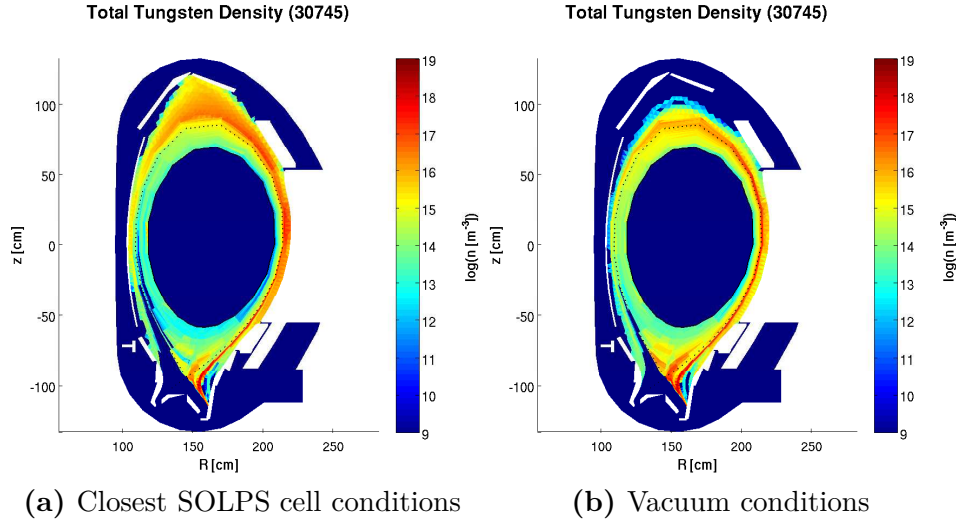


**Figure 3.9:** Comparison of two simulation with different extended grid assumptions for the plasma parameter extrapolation.

## 3.4 Other Numerical Codes

### NEOART

NEOART is a code designed to calculate the neoclassical transport coefficients (c.f. Chapter 2.2) using a diffusive and convective ansatz. It relies on an externally supplied magnetic geometry, read from a shotfile, and user specified profiles of electron density, electron/ion temperature and impurity density. The code is included in the STRAHL code package and is described in [1; 10; 11] and references therein.

### SOLPS 5.0

The SOLPS package used at IPP for the background calculations is version 5.0. SOLPS consists of the fluid code B2.5 and the EIRENE neutral transport code (FZJ-Vers. 1999, improved at IPP) or alternatively a simpler, faster neutral fluid model in B2.5. The B2.5 code basically solves the fluid moment equations including various source and sink terms for plasma reactions and the Poisson equation for the electric potential as well as supplying additional modules for diagnostic and comparison purposes (line integrated signals,...). SOLPS is extensively described in [95; 96]. The basic equations describing the moment evolution are the Braginskii equations given in Appendix A.6.





# CHAPTER 4

---

## Results

---

This chapter presents the results of our numerical simulations. The simulations were performed with the modified EIRENE 2010 version, which included our own upgrades (c.f. Sec. 3.3). The first section examines the applicability and validity of the approximations made in our EIRENE simulations. The approximations were introduced in subsection 3.2.1. Additionally some properties such as the thermalization of tungsten ions are scrutinized. A scan of important parameters like the TIM-time step was performed in order to estimate their impact on the simulations. An optimal parameter set with respect to computational requirements and numerical results is presented. The second section deals with a code benchmark of the TIM transport against NEOART results. The radial fluxes registered by EIRENE are compared to the expected radial fluxes of the banana transport regime. Transport coefficients produced by NEOART and EIRENE density profiles were used to determine the banana fluxes. Finally the simulation results are presented in the third section and the core penetration probability of tungsten is determined for different limiter and divertor source locations. L- and H-Mode plasma background calculated by SOLPS 5.0 were used in the simulations (c.f. Subsec. 3.3.2.3). A sample of important plasma parameters of these backgrounds is shown in Appendix A.3.

### 4.1 Code Tests

In this work a standard simulation case is defined with the input settings given in Tab. A.1 in Appendix A.1. The input parameters are briefly explained in the Appendix. The settings are an optimized choice, which resulted from a sensitivity scan of input parameters presented in Subsec. 4.1.3. The detailed meaning of these input parameters can be found in the code manuals[4; 5].

We like to point out some important facts that apply to all simulations in this thesis. EIRENE was set-up in the pseudo 3D-mode with 50 cylindrical slices in the toroidal direction. Three dimensional particle motion and geometry effects, like curvature, are taken into account. The profiles however remain 2D in the poloidal plane. In the framework of TIM calculations all electromagnetic fields are interpolated linearly from the cell-centered values of the background in all calculations. Furthermore, the innermost core boundary, shown in Fig. 4.1, is totally absorbing. It is thus implicitly assumed that

tungsten is not expelled from the inner core region. In Sec. 4.3 it is explained that this assumption is not entirely true for the separatrix. Banana orbits of tungsten cross magnetic flux surfaces multiple times. However, in our simulations the fluxes on the innermost grid boundary were at least about two orders of magnitude lower than the fluxes on the separatrix in all cases and are thus negligible (c.f. Sec. 4.3). To date the major unresolved concern is the TIM-time step, which is too large for accurate ion-tracing due to limited computational resources (c.f. Subsec. 3.3.1.5). Despite the considerable effort we put into the parallelization of EIRENE the same limitation forces us to exclude sputtering and reflection in our standard scenarios. Their impact was tested separately on the same background all sensitivity scans were performed on (#30745-D13<sup>1</sup>).

A fixed source strength of 1 A was specified in all simulations. The simulation results for the tungsten density thus need to be rescaled to whatever source strength one wants to compare with. The density profiles scale linearly with the source strength, because tungsten self-collisions are neglected in the current EIRENE setup. All simulations have been performed with a single divertor or limiter source. Divertor sources are surface sources attributed to SOLPS-grid cell boundaries on the targets<sup>2</sup>, whereas limiter sources are point sources defined on the LFS limiter and the HFS heat shield. All sources generate thermal particles ( $E_{kin} = 25$  meV) with a cosine velocity distribution centered around the surface normal (surface sources) or the inwardly directed major radius vector  $\pm \hat{e}_R$  (point sources). Emerging particles are evenly distributed on the surfaces and in the simulated time interval. The sources coordinates are given in Tab. A.2 in Appendix A.2 and are depicted in Fig. 4.1.

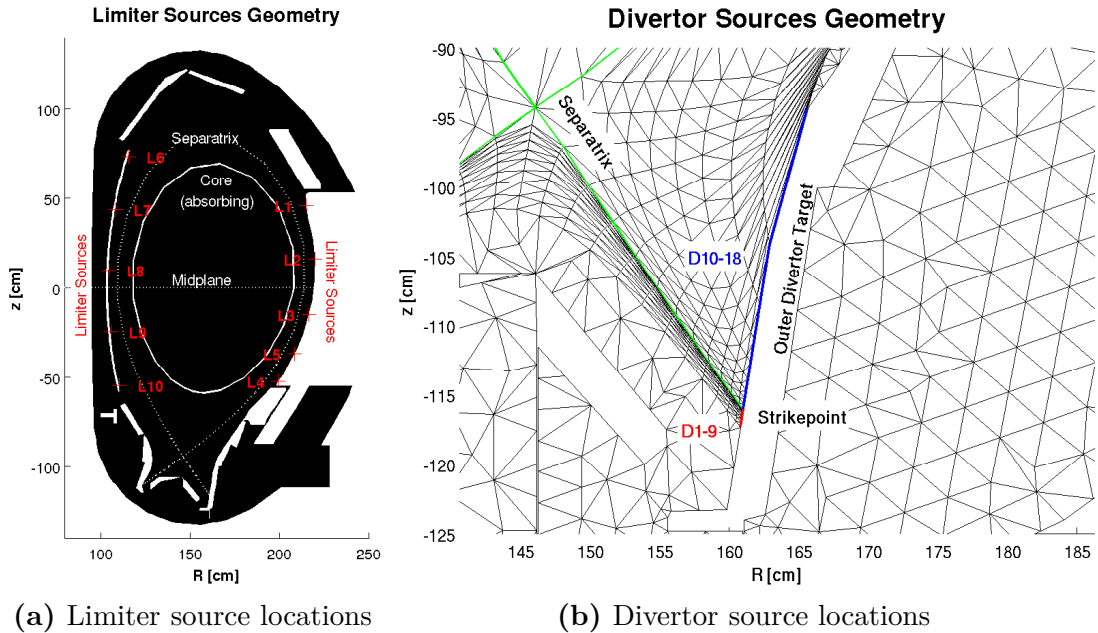


**Figure 4.1:** Source setup for EIRENE simulations. The limiter sources are point sources whereas the divertor sources are surface sources limited by grid cell boundaries (red below and blue above strikepoint).

- 1 The notation introduced here is: #(SOLPS simulation index)-(Source label), where 'D' are divertor and 'L' are limiter sources. Discharge indices in this chapter are always SOLPS indices unless stated otherwise explicitly.
- 2 The divertor source index coincides with the y-coordinate of the SOLPS grid of the according cell.

All sensitivity scans were performed on the L-Mode background #30745-D13. The total tungsten density profile (c.f. Fig. 3.9a) of this case was rather stable. An implication for the use of the divertor source D13 in this scans was the Langmuir probe data of the outer target, shown in Fig. A.1 and Fig. A.2. The data indicates high deuterium influxes of the order of  $3 \times 10^{21} \text{ m}^{-2} \text{ s}^{-2}$  at  $T_e \approx 10 \text{ eV}$  and a power load of  $P \approx 0.1 \text{ MWm}^{-2}$  around the strikepoint and up to  $s \approx 5 \text{ cm}$ . D13 is thus comprised in a target area likely to show considerable impurity production. In addition preliminary EIRENE simulations showed the largest core penetration probabilities and the largest peak densities of tungsten for this specific divertor source. D13 was also chosen in other analysis procedures such as the NEOART benchmark in Sec. 4.2. The H-Mode #31723-D13 was also examined more thoroughly in order to compare L- and H-Mode discharge behavior. Some important plasma parameters of the backgrounds are plotted and characteristic SOLPS parameters are summarized in Appendix A.3.

#### 4.1.1 Applicability of Code

##### Gradient Length and Timescale Assumptions

In this subsection the validity of the assumptions presented in Subsec. 3.2.1 are tested for the divertor source D13 on all four background plasmas given in Tab. 3.5 in Sec. 3.3. The results were rather ambiguous as Eq. (3.2) was not always valid at the separatrix and the SOLPS-grid boundary for reasons that will become clear in the thermalization paragraph below.

The test of the magnetic field gradient length  $L_B$  was successful. Equation 3.1 was valid on the entire grid for all ionization stages in all discharges. However, in simulations with the explicit integration threshold  $v_{\perp}^t = 0.1[5]$  the fluid moment gradient lengths,  $L_n$  and  $L_T$ , were strictly respecting the assumption of Eq. (3.2) only for lower charge stages up to  $Z_W = 5$  on the SOLPS-grid. The ratios were in general much closer to one than for the magnetic field gradient length. Outside the SOLPS-grid, the fluid moment gradients are zero, because of the applied extrapolation of the background (c.f. Subsec. 3.3.2.3). With increasing charge stages Eq. (3.2) holds on ever shrinking parts of the SOLPS-grid for  $T_e$ ,  $T_i$  and  $n_e$ . It starts to fail above  $W^{20+}$  around the LFS separatrix for the L-Mode simulation #30745-D13 with  $v_{\perp}^t = 0.1$  as shown in Fig. 4.3. In the simulations the gyroradius of  $W^{20+}$  varied from  $\varrho \approx 4 \text{ mm}$  to  $\varrho \approx 2 \text{ cm}$  and was probably largely overestimated due to thermalization problems (c.f. Subsec. 4.1.2). For the same background simulated with  $v_{\perp}^t = 1$  Eq. (3.2) was respected on the full grid. Midplane profiles (c.f. Fig. 4.2) of this case are shown in Fig. 4.4.

Equation (3.2) fails already from  $W^{12+}$  on for the H-Mode simulation #31273 with  $v_{\perp}^t = 0.1$ . The calculated gyroradii for this discharge span a range of  $\varrho \approx 1 \text{ cm}$  to  $\varrho \approx 3.5 \text{ cm}$ . A simulation with  $v_{\perp}^t = 1$  did not succeed in completely preventing the

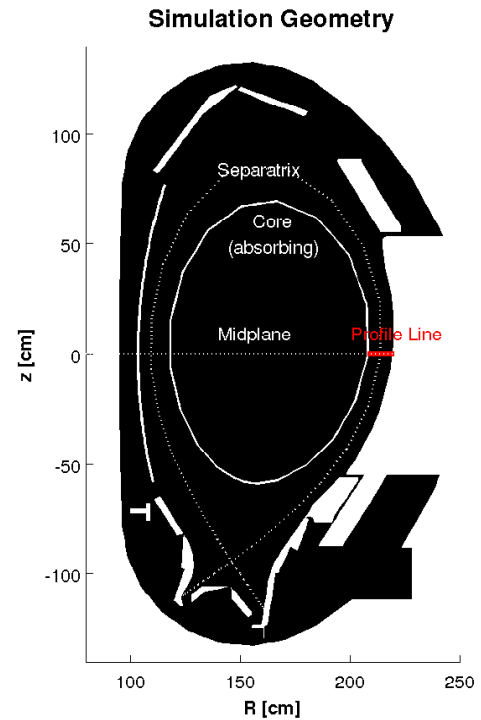


**Figure 4.2:** Midplane profiles are taken along the red line.

violation of the fluid gradient length assumption. However, the regions where the assumption is violated are largely reduced and are mainly restricted to the LFS separatrix. The H-Mode midplane profiles of the  $v_{\perp}^t = 1$  simulation are shown in Fig. 4.5. Higher explicit integration thresholds have not been tested yet.

Although the results are somewhat troubling with respect to the validity of the simulation results, the inconsistency in the scale ordering for H-Mode simulations is likely to be caused by a problem of thermalization in EIRENE. EIRENE overestimates the ion temperature of highly ionized tungsten ( $Z_W > 15$ ) largely as shown in Subsec. 4.1.2. This leads to an overestimate of the gyroradius, which ultimately violates the scale ordering.

The test of the timescale assumption is unnecessary in our current setup, because fluid effects of a changing background are of no concern. The background is fixed during the simulation and Eq. (3.3) is naturally fulfilled. In this subsection we proofed the validity of the gyroaverage approach for the presented L-Mode simulations. The gyroaverage scale assumptions were not completely respected by our H-Mode simulations. The validity of the gyroaverage approach, however, cannot be definitively declined until the thermalization issue of highly ionized tungsten in EIRENE is settled and simulations with higher explicit integration thresholds are tested.

### Trace Approximation

Testing the trace approximation is more difficult, because the current setup of EIRENE does not provide data for radiated power or the impact of the tungsten content on the background plasma. Due to the lack of a coupling to a fluid code, the trace approximation is imposed on us. However, we believe it is justified in the SOL plasma by experimental observations[39]. Our simulations show peak tungsten densities of about  $2.5 \times 10^{17} \text{ m}^{-3}$

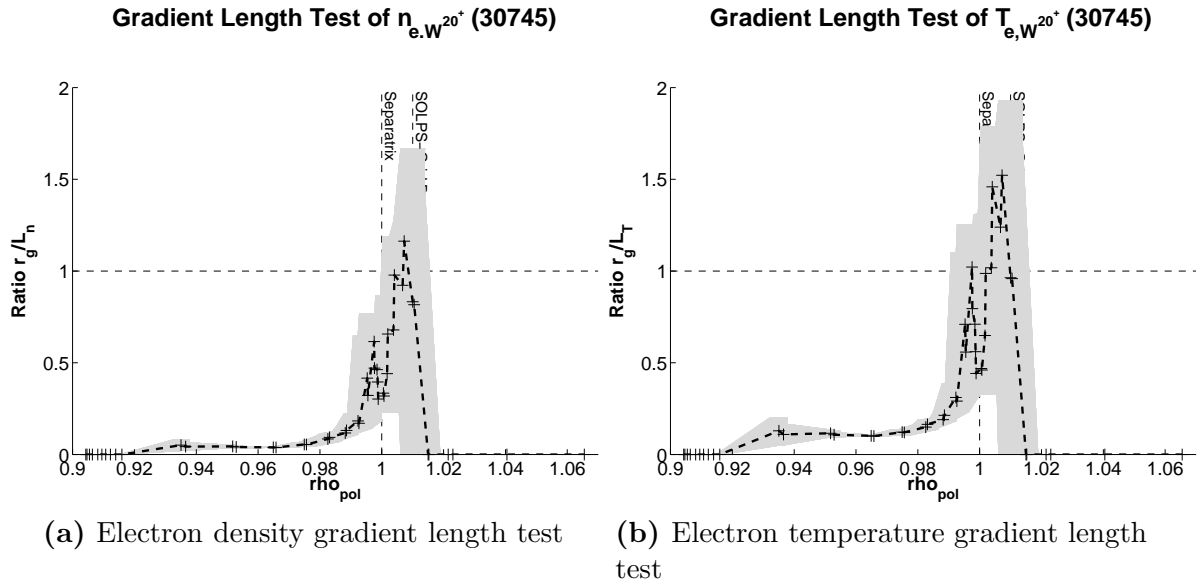


**Figure 4.3:** Gradient lengths test of #30745-D13 for  $W^{20+}$   $v_{\perp}^t = 0.1$ . Crosses are values extracted from the simulation results. The dotted line is a Savitsky-Golay fit with two neighbors and the shaded area shows the one sigma confidence interval for both x- and y-values. The sigma was derived from the averaging of appropriate corner point values (no distance weighting).

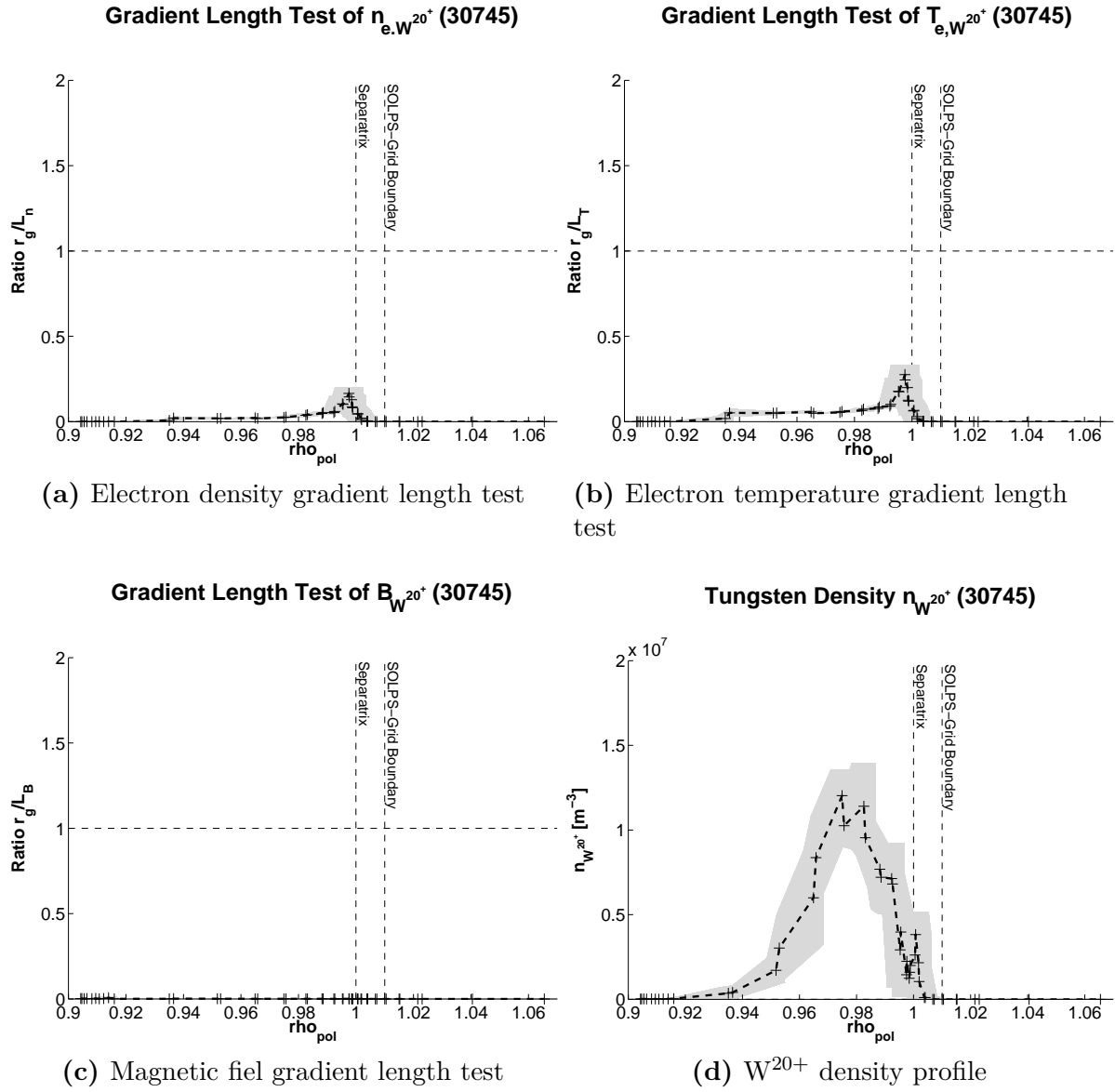


**Figure 4.4:** Old gradient lengths test of #30745-D13 for  $W^{20+}$  with  $v_{\perp}^t = 1$ . Crosses are values extracted from the simulation results. The dotted line is a Savitsky-Golay fit with two neighbors and the shaded area shows the one sigma confidence interval for both x- and y-values. The sigma was derived from the averaging of appropriate corner point values (no distance weighting).

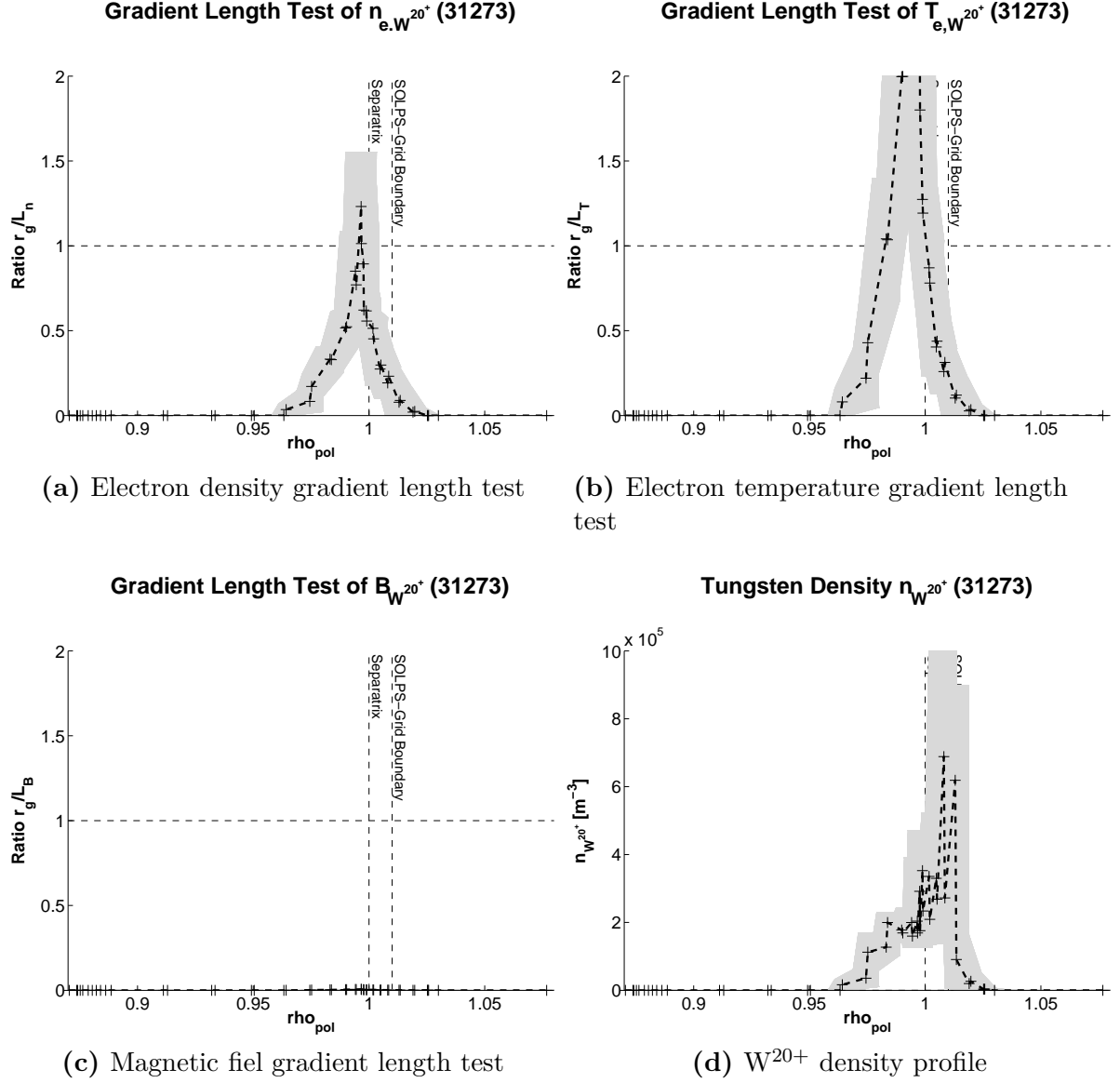


**Figure 4.5:** Gradient lengths test of #31273-D13 for  $W^{20+}$  with  $v_{\perp}^t = 1$ . Crosses are values extracted from the simulation results. The dotted line is a Savitsky-Golay fit with two neighbors and the shaded area shows the one sigma confidence interval for both x- and y-values. The sigma was derived from the averaging of appropriate corner point values (no distance weighting).

(c.f. Fig. 3.9a) for the L-Mode simulations and  $3.5 \times 10^{16} \text{ m}^{-3}$  for the H-Mode simulations for a source strength of  $S = 1 \text{ A}$ .

In order to get a physical tungsten density we estimate a realistic source strength for physical tungsten sputtering at a location near D13. We take the Langmuir probe data at  $s \approx 5 \text{ cm}$  from Figs. A.1 and A.2 in Appendix A.2 and extract the net sputtering yield from Fig. 2.2 in Subsec. 2.1.1.3. For the AUG L-Mode discharge #23039, we get  $T_e \approx 30 \text{ eV}$ ,  $n_e \approx 1 \times 10^{18} \text{ m}^{-3}$  and  $\Gamma_D \approx 3 \times 10^{21} \text{ m}^{-2}\text{s}^{-1}$ . A net sputtering yield of  $Y_{eff} \approx 3 \times 10^{-4}$  then results in a tungsten flux of  $\Gamma_{Sputter}^W \approx 1.44 \times 10^{-4} \text{ Am}^{-2}$ . The AUG H-Mode discharge #21372 provides the parameters  $T_e \approx 10 \text{ eV}$ ,  $n_e \approx 8 \times 10^{19} \text{ m}^{-3}$  and  $\Gamma_D \approx 1.5 \times 10^{22} \text{ m}^{-2}\text{s}^{-1}$ . With  $Y_{eff} \approx 5 \times 10^{-6}$  this leads to a tungsten flux of  $\Gamma_{Sputter}^W \approx 1.2 \times 10^{-4} \text{ Am}^{-2}$ . The source fluxes used in our EIRENE simulation can be derived from the user-specified source strength by  $\Gamma_{EIR} = S/A_{SRC}$ .  $A_{SRC}$  is the source surface given by  $A_{SRC} = 2\pi R_0 d_{SRC}$  (cylindric approximation).  $d_{SRC}$  is the length of the poloidal projection of the source surface, which can be extracted from Tab. A.2 in Appendix A.2.  $d_{SRC}$  varies from 0.3 mm to 10 cm and results in EIRENE source fluxes of  $\Gamma_{EIR} \approx 10 - 3000 \text{ Am}^{-2}$ . A comparison of the EIRENE source fluxes with the source fluxes derived from the Langmuir probe data implicates that all EIRENE tungsten densities throughout this thesis have to be rescaled with a factor ranging from  $10^{-5}$  to  $10^{-7}$ .

Assuming an average rescaling factor of  $10^{-6}$  the physically sound, rescaled peak densities of the EIRENE simulations would be about  $2.5 \times 10^{11} \text{ m}^{-3}$  for L-Mode and  $3.5 \times 10^{10} \text{ m}^{-3}$  for H-Mode simulations. Tungsten densities inside  $\varrho_{pol} < 0.98$  are even lower. The peak densities are at least seven orders of magnitude smaller than  $n_{e, Sep}$  in all SOLPS cases (c.f. Tab. 3.5) and implicate that tungsten really can be treated as a trace impurity in our simulations.

### 4.1.2 Temperatures and Thermalization in EIRENE

Analyzing temperature profiles of EIRENE, it is important to know that EIRENE actually calculates the kinetic energy density – not the temperature – for each test-ion species. The average kinetic energy of a particle  $E_{kin}$  is derived from the energy density by dividing by the density. A ‘pseudo-temperature’ can be defined by assuming a Maxwellian distribution. One gets

$$T_{W^{X+}} = 2/3 E_{W^{X+}, kin} \quad (4.1)$$

Equation (4.1) supposes that the particle species under consideration is in thermal equilibrium, which is in contradiction to the use of EIRENE in order to simulate also non-equilibrium particles/systems correctly. Additionally, with Eq. (4.1) all kinetic energy is taken as unordered, thermal energy rather than directed, kinetic energy. An inclusion of directed motion would require a shifted Maxwellian, which EIRENE cannot provide in the output.

#### EIRENE Thermalization

Thermalization unexpectedly turned out to pose a crucial challenge for our simulations. Minor thermalization issues were expected. A singularity in the Trubnikov-Rosenbluth potentials of the Fokker-Planck collision operator leads to a numerical instability, which had forced a change in the TIM from the original direct Euler-scheme to an implicit in-



tegration method[6]. Without the implicit integration the average temperature of equilibrated carbon ions was about 2 to 4 times higher than the background ion temperature<sup>1</sup>. The surplus of kinetic energy is caused by an unphysical acceleration of the carbon ions by the numerical instability. Proper thermalization of long-living charge states of carbon was achieved with the implicit integration scheme[6].

However, highly ionized ( $Z_W > 10 - 20$ ) tungsten species do not show proper thermalization on the entire grid. Temperatures more than 100 times higher than all background temperatures are observed. Especially the H-Mode simulations show temperatures far to high ( $T_W \lesssim 100$  keV) on considerable fractions of the grid. The unphysical high temperature indicates a numerical problem. In order to test the influence of the known numerical instability, simulations with increased explicit integration thresholds were performed. An increase of the normalized threshold velocity  $v_\perp^t = v_{kin}/v_{th}$  from 0.1 to 1.0 improved the thermalization considerably, but did not lead to full thermalization of long-living species – especially not at the (LFS) separatrix in the H-Mode simulations. The maximum tungsten temperatures were lowered by a factor of about 10.

In the examined simulations (#30745-D13 & #31273-D13 with  $v_\perp^t = 1.0$  and 0.1) the relative, statistical error of the total test-ion energy density ranged from 0-15% in most cells and showed maxima of 40%, mostly cells with negligible tungsten density. The relative error of the total test-ion density ranged from 0-15% in most cells and reached maxima of about 40-50% in LFS and about 50-100% in HFS cells with negligible tungsten density. Even though the errors are quite large and call for larger numbers of simulated particles, their magnitude is well below the thermalization overshoot of a factor of 100 and higher. The same applies to the concept of non-thermalized tungsten particles due to the repeated passage through areas of higher background temperature on banana orbits ( $w_b \approx 1 - 18$  cm).

Three different domains of thermalization behavior were found. To facilitate the presentation of the observations a thermalization deviation factor  $c_D$  is defined.  $c_D$  gives the ratio of a tungsten temperature  $T_{W^{x+}}$ , calculated with Eq. (4.1), to the fixed background ion temperature  $T_i$ . The results are summarized in Tab. 4.1.

#30745-D13		#31273-D13	
$c_D$ -Domain	$Z_W$	$c_D$ -Domain	$Z_W$
1-4	1-5	4-8	1-5
8-14	6-14	8-12	6-10
12-20	15-17	12-20	10-12
>20	>18	>20	>13

**Table 4.1:**  $c_D$  regimes for  $v_\perp^t = 0.1$  simulations.

A sample of thermalization ratios  $c_D$  of the characteristic tungsten ion  $W^{20+}$  is shown in Fig. 4.6 for the L-Mode #30745 and in Fig. 4.7 for the H-Mode #31273. The comparison of the  $v_\perp^t = 0.1$  simulation to the  $v_\perp^t = 1.0$  simulation shows the impact of the implicit integration. The thermalization problems are thus likely to be connected to the known numerical instability. A further increase in  $v_\perp^t$  should be envisaged in future simulations.

---

1 Private Communication with J.Seebacher

### Thermalization Factor of $W^{20+}$ (30745) Thermalization Factor of $W^{20+}$ (30745)

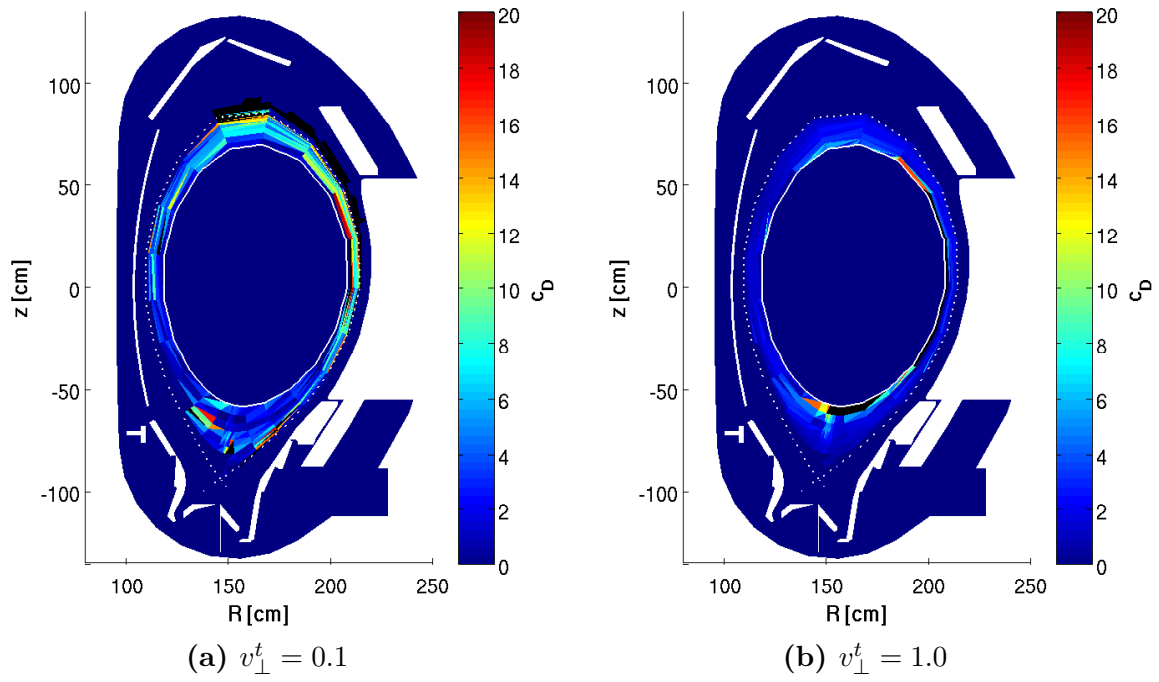


**Figure 4.6:** The thermalization factor  $c_D$  of  $W^{20+}$  is shown for #30745-D13 with different explicit integration thresholds.

### Thermalization Factor of $W^{20+}$ (31273) Thermalization Factor of $W^{20+}$ (31273)

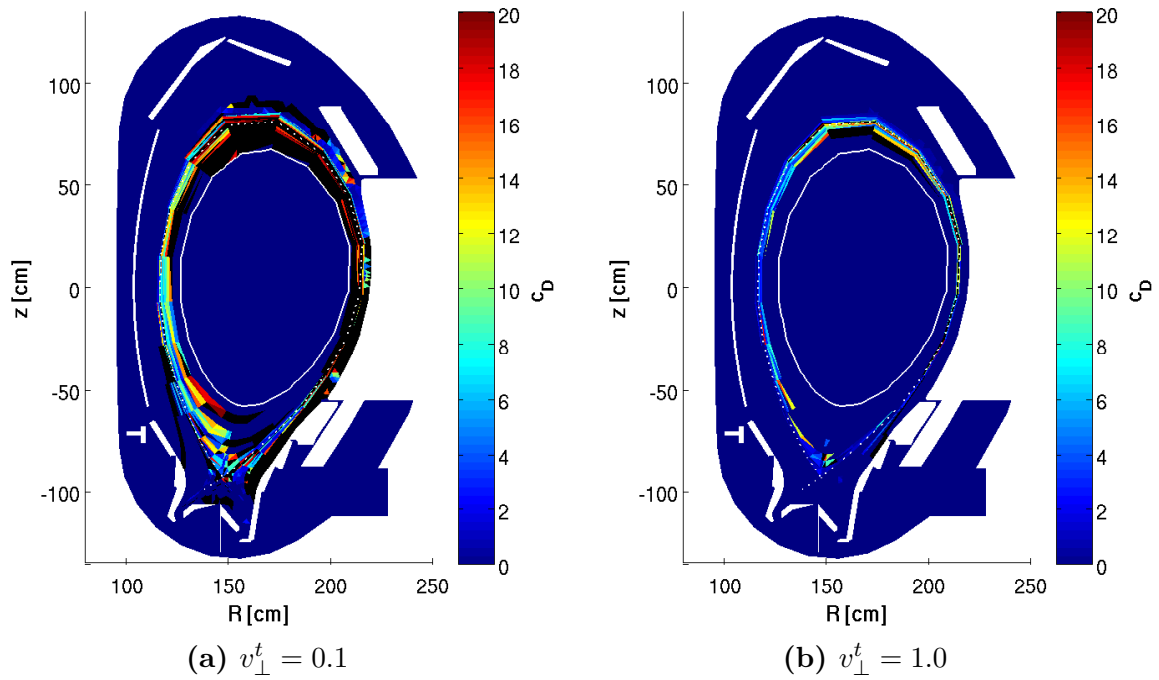


**Figure 4.7:** The thermalization factor  $c_D$  of  $W^{20+}$  is shown for #31273-D13 with different explicit integration thresholds.

### Temperature Correction with Directed Particle Motion by Drag

An additional feature of the temperature profile found in the SOL near the targets is shown in Fig. 4.8. In regions of considerable deuterium flow velocities of  $1000 - 3000$  m/s the tungsten temperatures, derived from the average kinetic energy (c.f. Eq. (4.1)), and hence  $c_D$  was augmented – also for lower charge states. This might be caused by the friction force simulated by the TIM. Fast flowing background ions possibly drag along the tungsten particles. This directed motion effect could also account for some of the magnitude of  $c_D$  near the watershed at the SOLPS boundary, where enhanced tungsten temperatures were observed in low tungsten density cells for intermediate charge states ( $Z_W = 10 - 18$ ) with mediocre thermalization ( $c_D \approx 8 - 12$ ).

The background drag seems to be most significant at the inner target in H-Mode simulations (c.f. Fig. 4.8). The fraction of the background flow velocity to which tungsten particles could be accelerated to by the drag is about 10% of the deuterium flow velocity at the outer target and a up to 30% at the inner target. Higher fractions would overcompensate and result in negative tungsten temperatures in some grid parts.

### Background Temperatures Correction of $W^{6+}$ (31273)

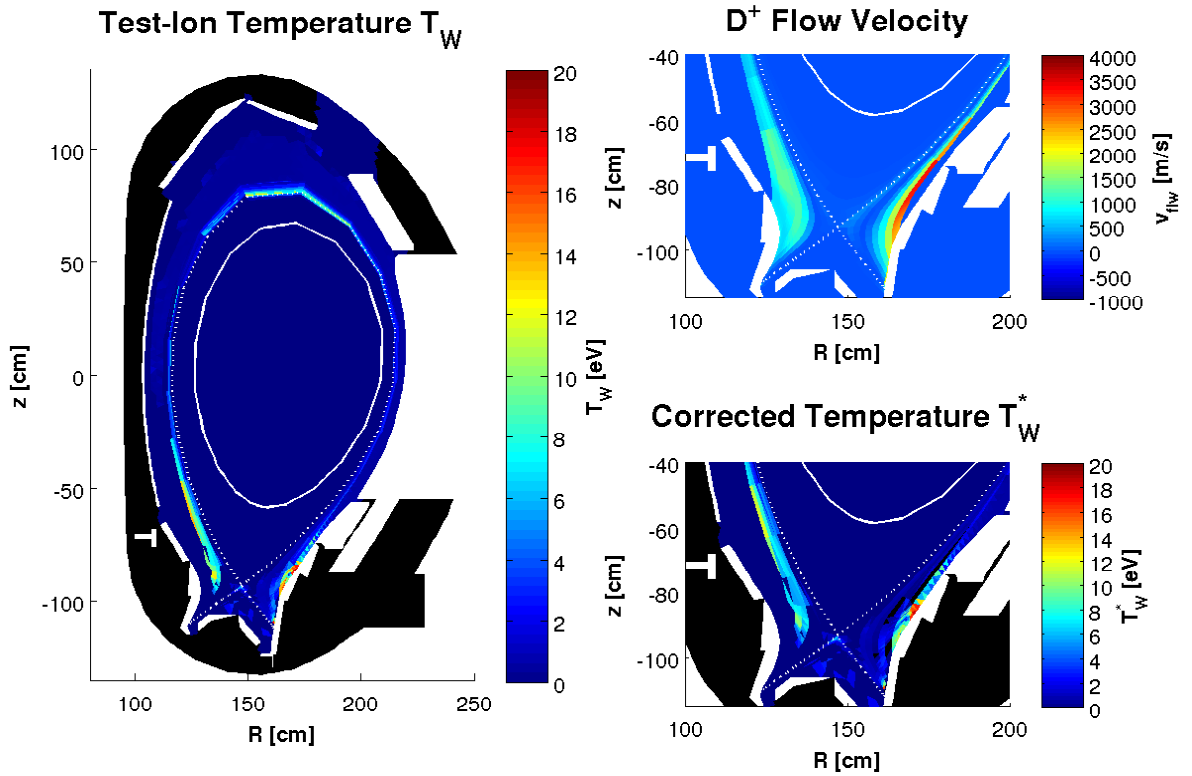


**Figure 4.8:**  $T_W$  of  $W^{6+}$  of #31273-D13 is shown on the left. The right top shows the deuterium flow velocity in the SOL near the divertor. The right bottom shows a corrected tungsten temperature with tungsten moving at 10% of the deuterium flow velocity. Black areas are either excluded from the plot (remote parts) or off scale (divertor).

### 4.1.3 Parameter & Sensitivity Scans

A sensitivity scan for several EIRENE-input parameters was performed. The TIM-time step was tested in the range from  $10^{-5}$  to  $10^{-12}$  s. Values below  $10^{-8}$  s did not succeed in tracing at least more than 1,000 particles in the available six days of computational time. The TIM-time step therefore was chosen to be fixed to  $10^{-7}$  s. Unfortunately the analog EIRENE version only yields approximately 4,000 to 40,000 particles with this TIM-time step. Nonetheless, TIM-time steps a lot smaller would be favorable and are eventually necessary in order to suppress the numerical outward drift (c.f. Subsec. 3.3.1.4).

The second parameter under consideration was the EIRENE time surface interval. The time surface interval sets a limit to the physical time a particle is followed. Particles trajectories are stopped at the end of the interval. The time surface interval was tested in the range of  $10^{-4} - 1$  s. It was then fixed to 20 ms in our simulations, because the tungsten density profile as well as the values for the tungsten peak density did not vary much for larger intervals. The chosen time interval is in the range of ELM frequencies. With respect to future coupled simulations including ELMs this is an important result. The tungsten distribution may not attain an equilibrium state for time intervals well smaller than 20 ms and the ELM frequency might have a critical impact on the inter-ELM tungsten distribution by forcing small physical time interval lengths in EIRENE. Time intervals down to 5 ms resulted in reduced peak densities with stiff profiles. For time intervals of 1 ms and below the tungsten density decreases rapidly.

Moreover, the background temperatures ( $T_e, T_i$ ) and densities ( $n_e, n_i$ ) were increased by a factor of 10 and 100. The resulting midplane profiles are shown in Fig. 4.9. For increased background densities the tungsten density accumulates on the LFS, probably due to more frequent collisions, and increasingly at the SOLPS-grid boundary. Inward of the separatrix the density decays fast to zero. A density accumulation at the midplane is also observed.

A background temperature increase of a factor of 10 smooths out the density profile and reduces the routinely observed peaking at the SOLPS boundary by two orders of magnitude. The tungsten density profile is more symmetric in the poloidal plane due to an increase of density at the HFS. The overall tungsten content is reduced by approximately three orders of magnitude. A further increase of the background temperature leads to negligible tungsten contents of the plasma. Particles seem to collide with the absorbing walls at their first pass of the midplane on the LFS.

The cell size of the external grid parts was also modified to be 10, 4.5 or 3.3 cm (diameter). EIRENE uses the grid only for storage of the tallies. Thus the only impact on the simulations should be the finer magnetic field resolution on the external grid parts.

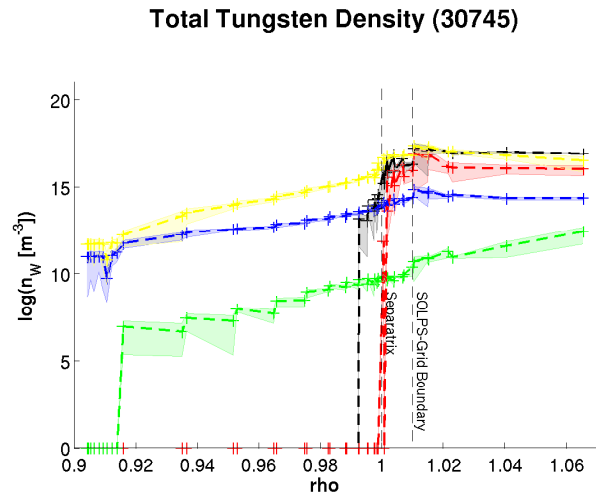


**Figure 4.9:** Midplane profiles of the sensitivity test of background densities and temperatures are shown. The lines are:  $10 \times n$  (black) and  $100 \times n$  (red),  $10 \times T$  (blue),  $100 \times T$  (green) and the standard #30745-D13 case (yellow). Errors in  $\varrho_{pol}$  are disregarded.

No change in the simulation results was observed. Thus, the interpolation routine for electromagnetic fields of EIRENE properly accounts for changes in the magnetic field on grid cells. SOLPS-grid cell sizes cannot be modified by EIRENE.

The impact of different surface model assumptions and the impact of various drift terms, including the recently introduced diffusion mock-up model, were checked qualitatively. The results of the surface model tests are shown in Fig. 4.10. The activation of reflections at the walls (with and without the targets) only leads to a slight increase of the tungsten density at the walls, a factor of 1.5 at the HFS and up to 8 at the LFS, and in the core. Combined sputtering and reflections leads to an increase of the tungsten density by approximately one order of magnitude all over the plasma minor radius. The shape of the density profile remains the same. In simulations with sputtering and reflections most traced particles resulted from sputtering and very few particles were actually released by the source – only three

to ten particles. Therefore the tungsten profiles are somewhat decoupled from the source distribution and are mostly determined by sputtering in the main chamber. More particles in EIRENE simulations would be needed in order to investigate this effect further. Considering the various drift effects, the most important contribution to the profile shape stems from the curvature drift. The  $\vec{E} \times \vec{B}$ -drift effects could not be checked separately as the electric potential was not an EIRENE input at that stage of our work. It is, however, included in all other simulations presented in this thesis. With all drifts deactivated the density is strongly confined to a small area in the LFS-SOL close to the X-point as would be expected from bouncing particles without a radial excursion from the magnetic flux surface. The diffusion mock-up model was tested in combination with all drift effects. It was smoothing the tungsten density peaking mildly and the edge tungsten density increased. A separate validation of the diffusion model as well as a comparison of the effective diffusion coefficient, extracted from EIRENE profiles, with the input value has not yet been performed, because of unexpected compilation problems. The perpendicular diffusion thus was not included in any of the presented simulations.

Additionally the activation of electron collisions and the use of separate diffusion coefficients  $D_i$  instead of the default effective coefficient  $D_{eff}$  in the Fokker-Planck operator were tested. Although the computational time increased, the simulation results did not change. An effective diffusion coefficient was employed and electron collisions were neglected in the Fokker-Planck operator throughout all simulations. The above summary leads to the selection of the standard case parameters as described in Sec. 4.1.

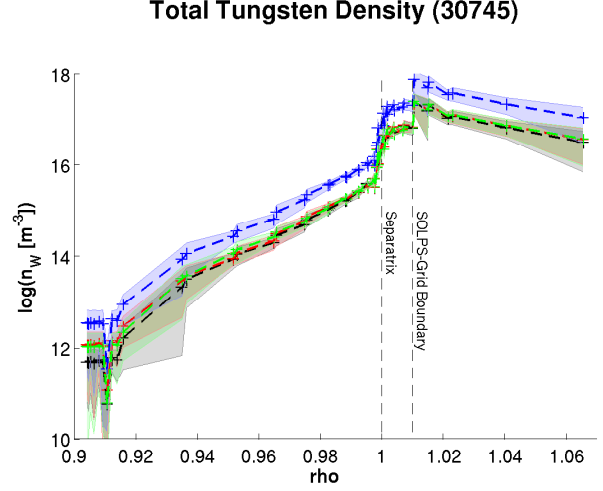


**Figure 4.10:** Midplane profiles of the surface model test are shown. The lines are: reflection at the entire wall (red) / at the wall without the strikezone (green), sputtering and reflection at the entire wall (blue) and the standard #30745-D13 case (black). Errors in  $q_{pol}$  are disregarded.

## 4.2 Benchmark against NEOART

In order to test the transport properties of the Trace-ION Module a benchmark against the well established NEOART code[10] is presented in this section. All NEOART calculations were performed with complete, flux surface averaged SOLPS profiles for deuterium, helium and carbon impurities and the AUG-shotfile based magnetic equilibrium. The TIM includes all necessary ingredients – like drifts, a Fokker-Planck collision operator in velocity space and a zero gyro-radius assumption – to be tested against pure neoclassical banana transport determined by NEOART’s neoclassical transport coefficients. The flux surface average was calculated by summing up background quantities on closed SOLPS flux surfaces and subsequently dividing by the number of grid points of each flux surface. As the profiles, especially the tungsten density profile, are actually not constant on flux surfaces (c.f. Fig. 4.11) the average was performed once for the whole flux surface and once for half a flux surface on the more homogeneous LFS. The LFS grid part also exhibits larger tungsten densities than the HFS part. Hence, the radial tungsten transport in our simulations should be largest on the LFS (c.f. Eq. (2.47)). Given the flux surface averaged plasma profiles NEOART calculates a variety of neoclassical transport parameters, including the banana drift velocity  $v_{dr}^{BP}$ , the banana diffusion coefficient  $D^{BP}$  (c.f. Sec. 2.2) and the effective tungsten charge state  $Z_{W,eff}$ .

A first comparison of EIRENE and NEOART results can be obtained by looking at the variation of the effective charge of tungsten  $Z_{W,eff}$  with  $\rho_{pol}$ . NEOART determines an effective charge by applying the corona equilibrium using ADAS electron impact and radiative recombination data<sup>1</sup>. An effective tungsten charge was derived from EIRENE results by averaging of the tungsten densities for all charge states, weighed with the charge number and normalized to the total tungsten density. Figures 4.12 and 4.13 show the  $Z_{W,eff}$  profile of NEOART and EIRENE. Good agreement is obtained for both L-Mode simulation #30745-D13 ( $v_{\perp}^t = 1.0$  and 0.1). In the H-Mode simulation #31273-D13 the effective tungsten charge

**Total Tungsten Density  $n_W$  on the Separatrix (30745)**

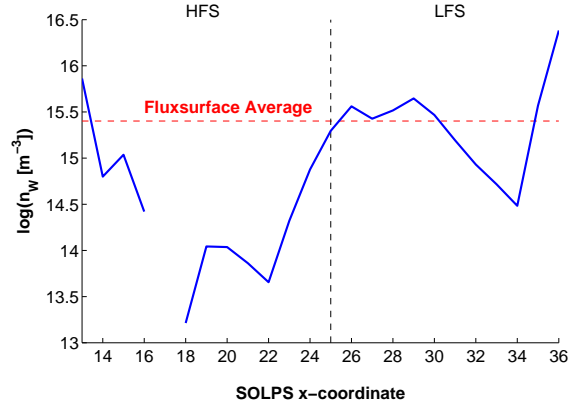


**Figure 4.11:** Total tungsten density profile on separatrix of standard case #30745. The poloidal asymmetry is obvious.

**Effective Tungsten Charge (31273)**

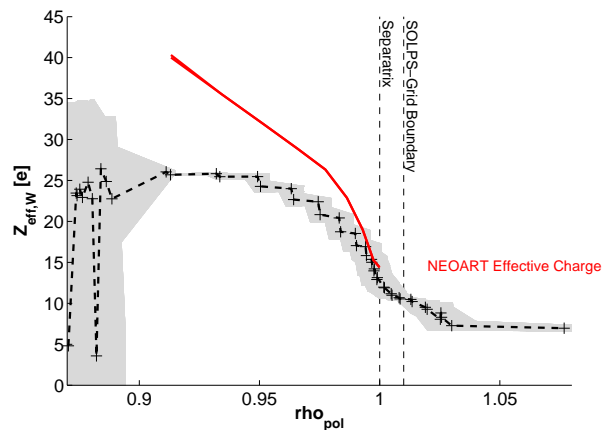


**Figure 4.12:**  $Z_{W,eff}$  calculated by EIRENE (black) and NEOART (red) for #31273-D13 with  $v_{\perp}^t = 0.1$ .

<sup>1</sup> The employed ADAS data was ACD/SCD96 for H, D, T, DT, He, C and ACD/SCD01 for W

was underestimated. The increase in  $v_{\perp}^t$  improved the situation considerably, but the deviation was still large inside  $\varrho_{pol} < 0.96$ .

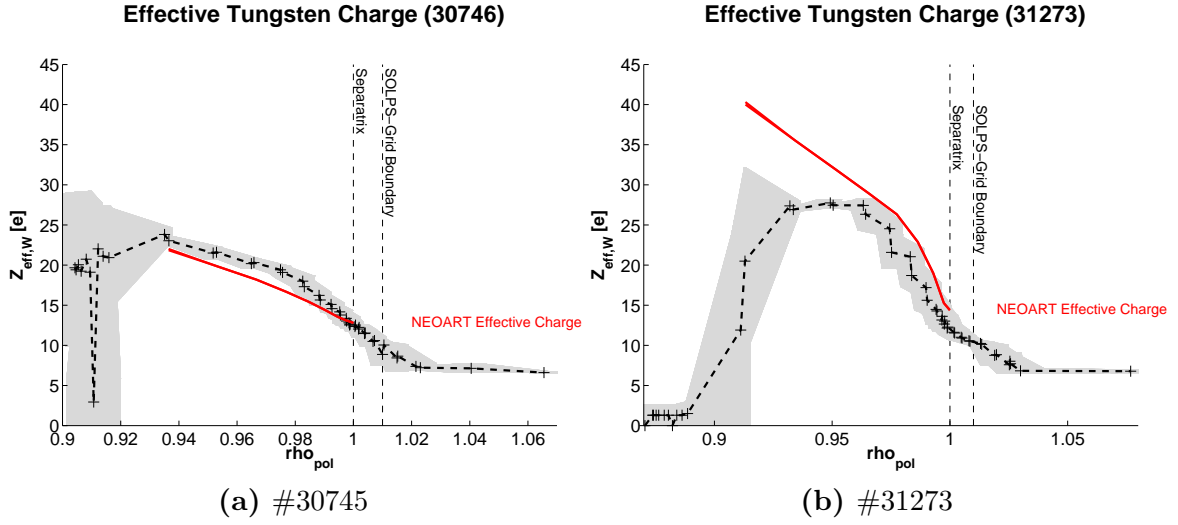


**Figure 4.13:** The effective tungsten charge  $Z_{W,eff}$  calculated by EIRENE (black) and NEOART (red) are in good agreement for L-Mode and deviate for H-Mode simulations inside of  $\varrho_{pol} < 0.96$ . EIRENE simulations with  $v_{\perp}^t = 1.0$  and both NEOART profiles (LFS & Full Flux Surface) are plotted.

A benchmark of EIRENE against NEOART was performed. The parameters of the employed plasma backgrounds can be found in Appendix A.3. The benchmark compared radial tungsten fluxes crossing the closed SOLPS-grid flux surfaces. One set of fluxes was obtained by EIRENE, which counts particle fluxes crossing user-specified grid cell boundaries directly<sup>1</sup>. The other set was obtained by applying the banana transport coefficients from NEOART to the tungsten density and density gradient profile calculated with EIRENE. In all NEOART calculations the trace approximation for tungsten was applied by assuming a constant tungsten density of  $10^1 \text{ m}^{-3}$  all over the plasma<sup>2</sup>. This procedure was done for the four simulations presented above independently. The flux surface averaged tungsten density and density gradient<sup>3</sup> profiles are shown in Fig. 4.14. The density profiles of #30745-D13 look pretty much the same for different ( $v_{\perp}^t$ ) and the same average. They are shifted up in density for a decrease of  $v_{\perp}^t$ . All profiles exhibit a near exponential density decrease towards the core. For the full average the poloidal angle asymmetry leads to negative gradients for low  $v_{\perp}^t$  and a steep decrease for high  $v_{\perp}^t$  at the core boundary. The density profiles of #31273-D13 also show near exponential decrease towards the core with a mild flattening  $\varrho_{pol} = 0.95$  in all cases except for the full-average, high  $v_{\perp}^t$  case. There the flattening is more pronounced and located around  $\varrho_{pol} = 0.98$ .

The results of the NEOART/EIRENE flux calculations are shown in Fig. 4.15 along with the fluxes counted directly by EIRENE. A promising observation in L-Mode simulations

- 
- 1 EIRENE fluxes are always full flux surface average fluxes, because closed flux surfaces are necessary calculate net fluxes excluding multiply crossing particles
  - 2 Tungsten self-collisions are thus neglected in the NEOART runs. The same is true for EIRENE simulations.
  - 3 Gradients are taken with respect to the STRAHL coordinate  $r_{V-Strahl}$  defined in Eq. (2.56).



and for the H-Mode with  $v_{\perp}^t = 1.0$  is that the EIRENE fluxes are roughly of the same order of magnitude as the NEOART fluxes between  $\varrho_{pol} = 1.0$  and  $\varrho_{pol} = 0.99$ . However, an increasing difference is observed further inward for all cases and the difference to the nearly constant EIRENE fluxes is the same for different  $v_{\perp}^t$ , two orders of magnitude for L-Mode cases and three order of magnitude for H-Mode cases. The EIRENE counted fluxes are surprisingly flat when one considers the near exponential tungsten density decrease from the separatrix to the core, shown in Fig. 4.16 in Sec. 4.3. In the H-Mode case #31273-DR13 the net influx even increases from the separatrix to the core. This would indicate a more flat density profile as for the L-Mode, which is not the case (c.f. Fig. 4.14).

Unfortunately the results presented above were obtained only recently. Previous analysis resulted in matching orders of magnitude between the EIRENE and the NEOART fluxes due to a bug in the analysis routines. With the recent discovery of this bug only limited time was available to determine the causes of the discrepancies in the two sets of net fluxes. The next paragraph therefore only summarizes a list of possible errors that should be investigated further.

A possible source of errors is the asymmetry in the plasma profiles with respect to the poloidal angle. The asymmetry is completely neglected in the neoclassical approach of NEOART, which assumes constant values on flux surfaces for all plasma quantities. The incomplete exact alignment of the SOLPS flux surfaces to magnetic flux surfaces, due to the limited resolution of the grid, may also contribute to such asymmetry effects. A currently missing flux surface area correction in EIRENE<sup>1</sup> as well as particles that are displaced due to numerical accuracy issues (c.f. Subsec. 4.3.1), which are not accounted for in EIRENE fluxes, are further sources of errors. A comparison of the flux surface areas given in the EIRENE output and those derived from the magnetic equilibrium data, provided by the libkk-routines of Fuchs[64], resulted in a mismatch of roughly a factor of 2. In the current EIRENE version this is explained by a missing correction for the fact that all cell boundaries are counted twice due to the triangular mesh structure.<sup>2</sup> A remarkable accumulation of tungsten at the SOLPS-grid boundary was observed throughout all simulations. The accumulation might be attributed to numerical errors due to the change in the grid structure from unordered to field aligned grid cells. Possible numerical problems at the SOLPS-grid boundary could be a reason for the fact that the fluxes are well in agreement at the separatrix, where the SOLPS-grid boundary is close by, and far off in the core parts that are well separated from it. However, all presented sources of errors are not likely to result in flat EIRENE net flux profiles and deviations as large as observed. The TIM transport description as well as our evaluation should be thoroughly rechecked. The TIM should be further benchmarked against other codes.<sup>3</sup>

Apart from the transport coefficients NEOART also provides the core collisionality, which is around 2-6 in the H-Mode cases and 2-8 in the L-Mode cases. The collisionality is thus well above the banana and even the Pfirsch-Schlüter limit on the majority of the radial extend of the plasma. Therefore, realistic neoclassical tungsten transport on the em-

---

1 A flux surface area correction to account for the bending of the cylinder to a toroidal configuration is not implemented in EIRENE.

2 In all presented Neoart flux calculations the correction is done manually.

3 An indication of some persitant errors in the code is the fact that Neoart derived net influxes are at least one order of magnitude smaller than influxes counted by EIRENE. The unidirectional influxes do show an exponential decrease towards the core (c.f. Sec. 4.3) in both cases.



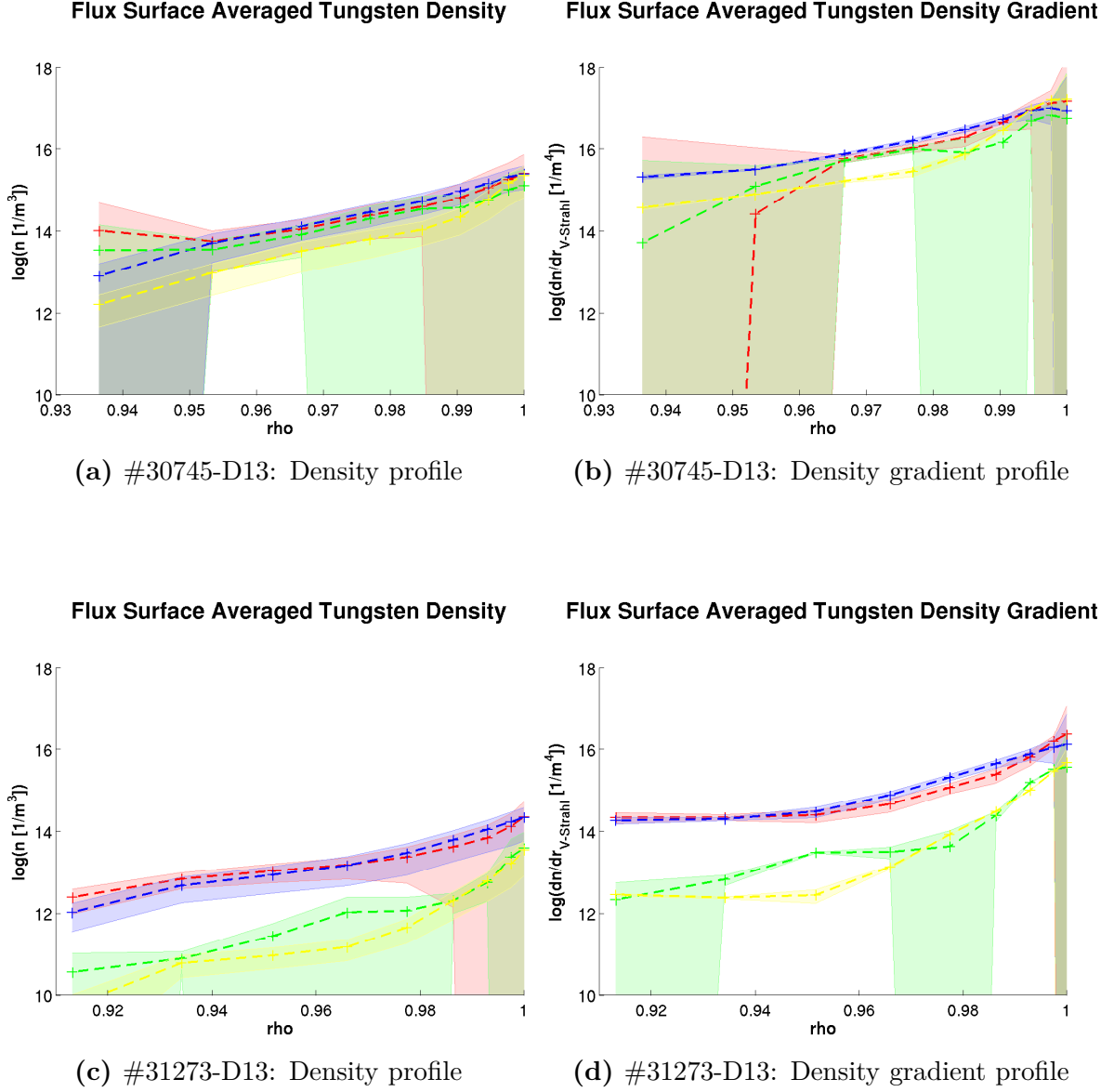


**Figure 4.14:** The flux surface averaged total tungsten profiles of shot #30745-D13 and #31273-D13 are shown. Density gradients are calculated with respect to the radial coordinate  $r_{V-Strahl}$  given in Eq. (2.56) and used in the NEOART and STRAHL codes. The color coding is  $v_{\perp}^t = 0.1$ : LFS-Average (red) / Full (blue) - Average and  $v_{\perp}^t = 1.0$ : - LFS (green) / Full (yellow) - Average. The shaded area gives the standard deviation resulting from the flux surface average of the EIRENE profiles. Errors of  $\rho_{pol}$  are negligible.

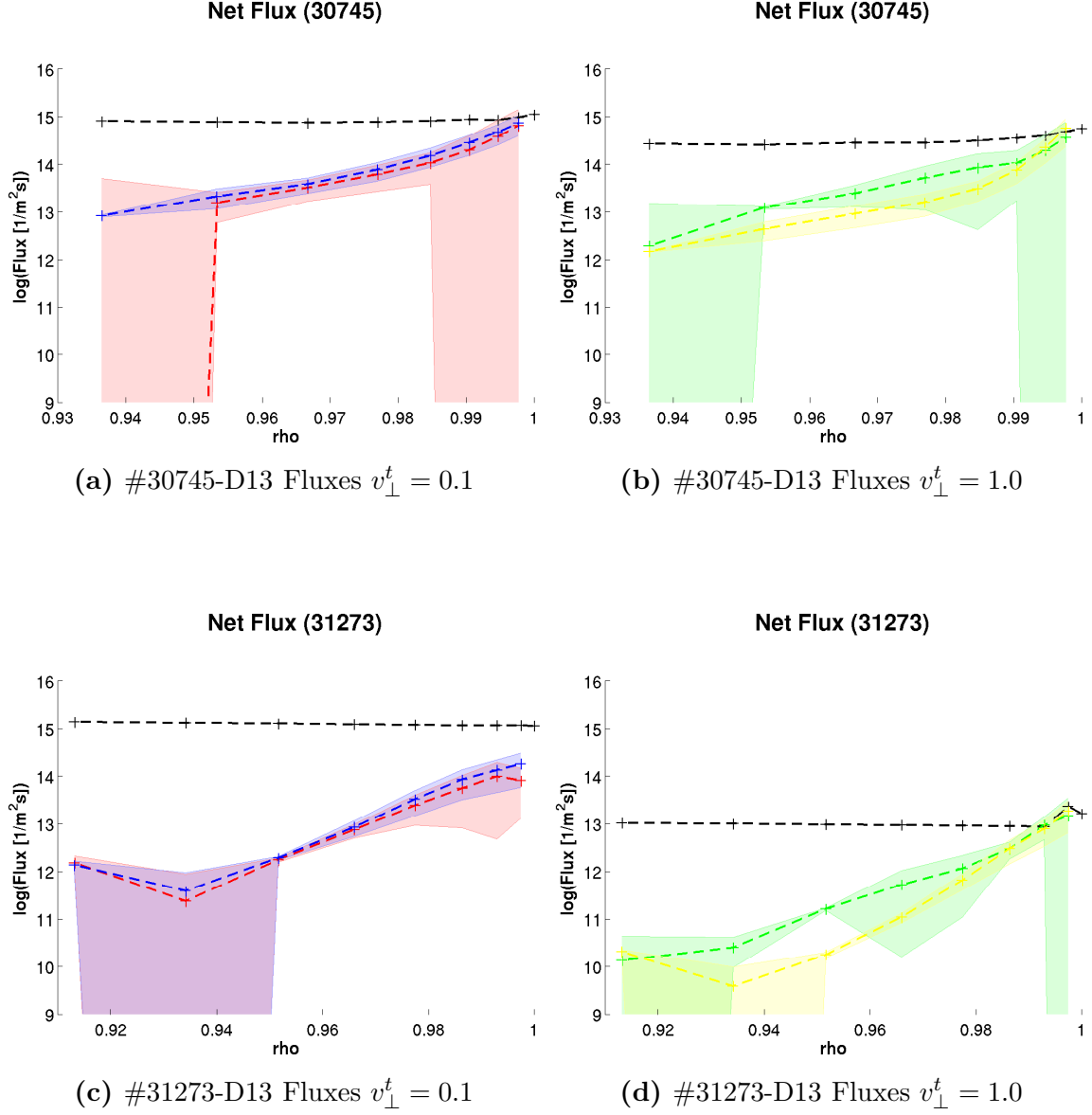


**Figure 4.15:** The net inward fluxes into the core of EIRENE and NEOART results are compared. The color coding is: EIRENE counted flux (black) and fluxes derived from the EIRENE profiles with NEOART coefficients for  $v_{\perp}^t = 0.1$ : LFS-Average (red) / Full (blue) - Average and  $v_{\perp}^t = 1.0$ : - LFS (green) / Full (yellow) - Average. The shaded area gives the standard deviation resulting from the flux surface average of the EIRENE profiles. Errors of  $\varrho_{pol}$  are negligible.

ployed backgrounds is well dominated by Pfirsch-Schlüter transport. Banana transport should even be negligible.

The benchmark of this section demonstrated that EIRENE does not work correctly in order to describe the banana transport in the core region – either in the TIM, flux count and/or geometry routines. The correct order of magnitude of fluxes were reproduced only at the separatrix. Nonetheless, we proceed to the application of the EIRENE code to the problem of tungsten migration in AUG and the determination of the core penetration probability of tungsten released at the vessel walls. The fact that the banana transport fluxes were in good agreement with NEOART calculations at the separatrix might indicate a correct transport description outside the separatrix, which would be most important for core penetration probability calculations.

### 4.3 Profile Calculations & Penetration Probability

The initial starting point of this thesis was the need to determine the core penetration probability of tungsten impurity released at the divertor target plates and the limiting structures of AUG in the main chamber. The core penetration probability is the probability of a released tungsten particle to enter the core plasma, where it can deteriorate the plasma confinement and the plasma properties. The decisive event is defined to be the crossing of the separatrix. A source strength of  $S = 1$  A in all our simulations implies that a flux given in Ampère is equivalent to the probability of a tungsten particle to cross the surface to which the flux is assigned to. The core penetration probability is thus rather given in terms of fluxes than percentages.

It is again pointed out that the current TIM transport only accounts for banana transport effects. Pfirsch-Schlüter or anomalous transport are neglected. The results presented in this section therefore cannot be directly compared to the experimental measurement.

#### 4.3.1 Profiles

A set of different tungsten sources according to Tab. A.2 in Appendix A.2 were simulated. Surface sources on the target as well as point sources at the outer limiter and at the inner heat shield were considered. The limiter source locations are shown in Fig. 4.1 in Sec. 4.1. The standard input parameters given in Tab. A.1 in Sec. 4.1 apply to all simulations henceforth presented. Again, the core boundary was totally absorbing in all simulations and the fluxes over the SOLPS flux surfaces were counted by EIRENE. The EIRENE fluxes were taken as a measure of the penetration of the tungsten impurity into the core plasma. However, it should be noted that there are still some minor issues to be further examined. First, EIRENE does not count particles crossing the cell boundaries in a geometrical correction routine. These routines relocate particles with velocities parallel to and near cell boundaries by small distances<sup>1</sup>. The fraction of such missing fluxes is not yet determined and might be considerable as ions are generally traveling parallel

---

<sup>1</sup> EIRENE tries to force an intersection of the particle trajectory with a cell boundary if there is none to be found due to limited numerical accuracy.

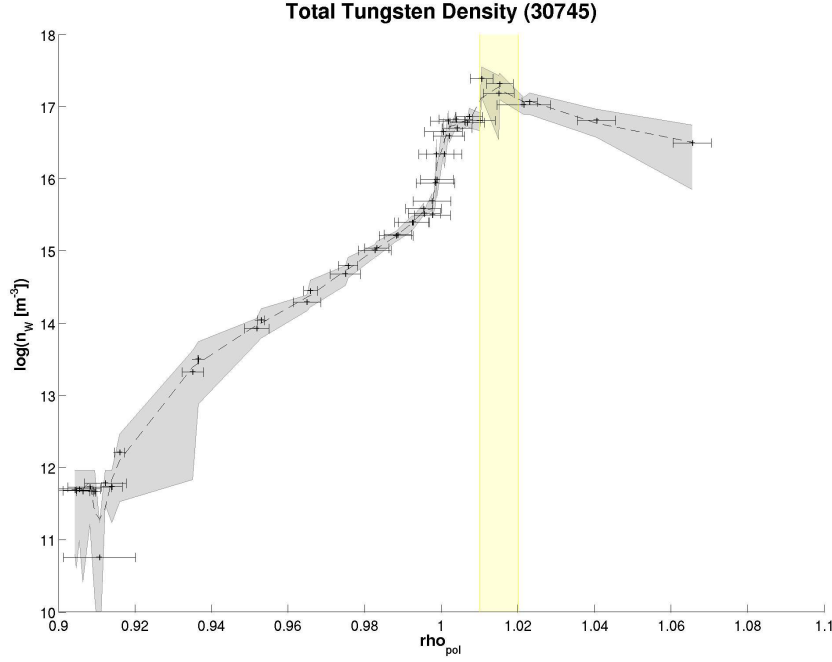


**Figure 4.16:** Midplane total tungsten density profile for #30745-D13 (c.f. Fig. 4.2). The yellow-shaded area indicates the position of the outer SOLPS-grid boundary, which is around 1.01 at the LFS midplane. The grey-shaded area is the one sigma interval for x- and y-values obtained as explained Fig. 4.4.

to the SOLPS-grid cell boundaries, which represent magnetic flux surfaces. Another particularly striking fact is the rare occurrence of negative net influxes over closed flux surfaces. Since there are no sources inside the closed flux surfaces and all reactions in the bulk are not weight-changing this can only be due to numerical errors. No effective net outfluxes should be observed.

The second problem is the procedure of surface correction in EIRENE. The surface for given SOLPS flux surfaces is calculated by EIRENE. It was compared to the result of a cylindrical estimate based on the flux surface volume given by the libkk routines by C. Fuchs[64]. A discrepancy of a factor of approximately 2 was found between simulations and magnetic equilibrium data.

Looking at the simulation results, we observe that a general feature of all simulations was a tungsten density peaking at the SOL SOLPS-grid boundary. A similar accumulation of carbon ions at grid-boundaries in simulation of a MAST plasma was observed by Seebacher in simulations presented at the EPS[97]. The density profiles in the SOL are generally highly asymmetric with respect to the poloidal angle for divertor sources and heat shield sources that are located far from the midplane. The poloidal density asymmetry is not as pronounced in the core region. Another issue for all simulations was a relatively modest thermalization of tungsten at higher charge states (c.f. Subsec. 4.1.2). Unfortunately, we are restricted to simulations with an explicit integration threshold of  $v_{\perp}^t = 0.1$  in this section, due to limited computational resources.

### 4.3.2 Penetration Probability

#### Divertor Sources

First, the divertor sources were analyzed. All SOLPS-cell boundaries with  $y = 0$  or  $y = 48$  were surface sources for separate simulations. The appropriate SOLPS-surface geometry data is given in Tab. A.2 in Appendix A.2. The particle streams<sup>1</sup> through closed SOLPS magnetic flux surfaces counted by EIRENE were subtracted in order to derive the effective net influx, given in A. The EIRENE registered particle streams as well as the net influxes for the two SOLPS simulation sets #30745 (L-Mode) and #31273 (H-Mode) are shown in Fig. 4.17 and Fig. 4.18.

Both cases show a considerable core penetration probability of about 20% starting from the divertor source 4 ( $s \approx -5$  mm) in L-Mode and 5 ( $s \approx -4$  mm) in H-Mode. The penetration probability rises sharply to a 70% level going to the divertor source 6 or 8 respectively. The probability remains at that level up to the divertor sources 9 or 11 respectively. A second sharp increase then leads to a new peak level of 150% or 90% at divertor sources 13 for both L- and H-Mode respectively. The intriguing fact of having a penetration probability greater than 1 in L-Mode is readily explained. Particles can escape and re-enter the core plasma. Single tungsten particles cycling on banana orbit are likely to cross the separatrix several times. Thus, a better quantity of the effect of the impurity transport into the core would be the net influx calculated by subtracting

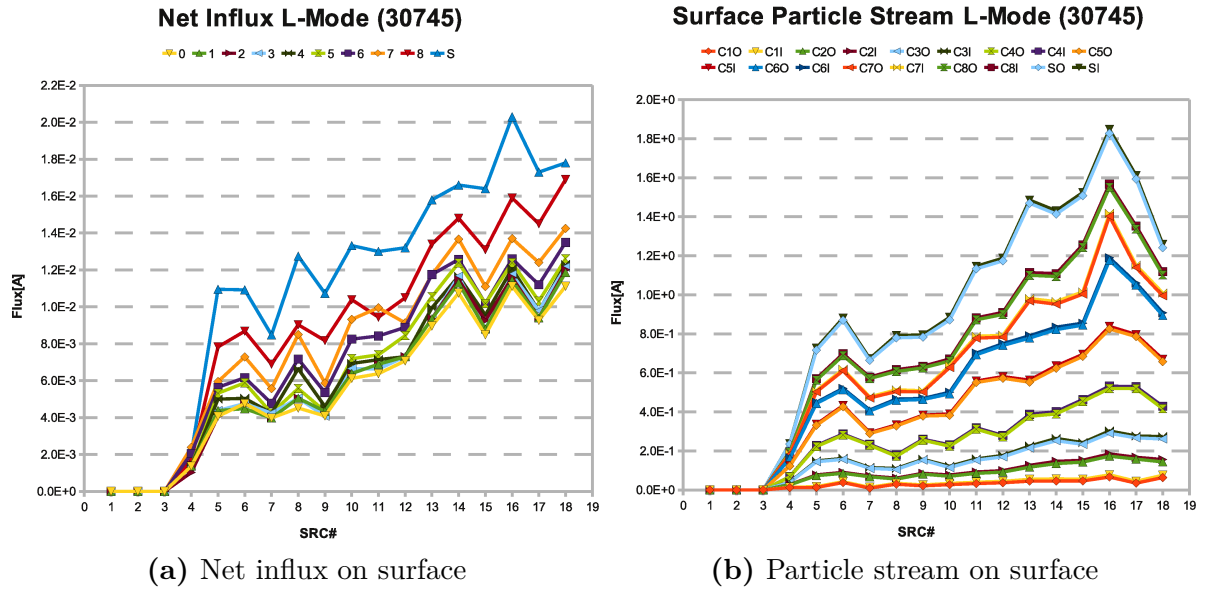


**Figure 4.17:** The net influxes and the particle streams on closed flux surfaces are shown for the standard set #30745. The particle stream and the net influx are not normalized to the surface area and are given in A. We had 10 closed SOLPS flux surfaces, including the core boundary (C) and the separatrix (S). The flux surfaces are numbered from the core boundary outwards (C,1-8,S). The additional label I/O denotes inward or outward directed particle streams respectively.

<sup>1</sup> EIRENE fluxes are given in A and are not normalized to the surface area. They are called fluxes by abuse of language and are not physical fluxes. The EIRENE flux term will be used in this section for net fluxes. Unidirectional fluxes counted by EIRENE will be called particle streams to distinguish them from the derived net fluxes.

the EIRENE registered particle streams (in-out). This gives an estimate of the residual tungsten, remaining in the core as impurity content. However, the particle gross fluxes are helpful quantities to estimate contributions of tungsten particles which temporarily reside in the core plasma to the core plasma evolution.

The net influx behaves similar to the gross fluxes. A considerable penetration probability of about 1% is attained from the divertor source 5 or 6 on for the L- or H-Mode respectively. An increase to up to 1.6% towards the divertor source 13 ( $s \approx 1.7$  cm) is observed in both cases. For H-Mode operation this is the maximum, while L-Mode operation allows the penetration probability to rise further to about 2% at divertor source 16. Then it drops again to a level of 1.8% further upstream.

Comparison of the target load profiles given in Fig. A.1 and Fig. A.2 in Appendix A.2 with the penetration probability profile yields a favourable situation for L-Mode, where most of the power is deposited on the outer target downward of the strikepoint, in regions with relatively low core penetration probabilities. The same is true for the deuterium influx, which will cause tungsten production by sputtering. In H-Mode however the situation is reversed. Most of the power on the outer target is deposited around  $s \approx 2$  cm and the deuterium influx is largest there. The divertor sources matching this s-coordinate most accurately would be the divertor sources 13 ( $s \approx 1.7$  cm) and 14 ( $s \approx 2.7$  cm). Exactly the sources with the maximum penetration probability. Higher densities seem to push this maximum probability further out (c.f. Fig. 4.19).

An increase in density also seems to have a reducing effect in terms of the penetration probability. Figure 4.19 shows a reduction of the net penetration probability (net influxes) in the H-Mode cases of roughly a factor of two. A onset of core penetration is only observed closer to the strikepoint. The separatrix electron density was approximately 10% higher in the second H-Mode case #31274 (c.f. Tab. 3.5). In L-Mode an electron density increase at the separatrix of about 20% lead to a total suppression of net core penetration.

An interesting difference in L- and H-Mode simulations #30745 and #31273 is the de-

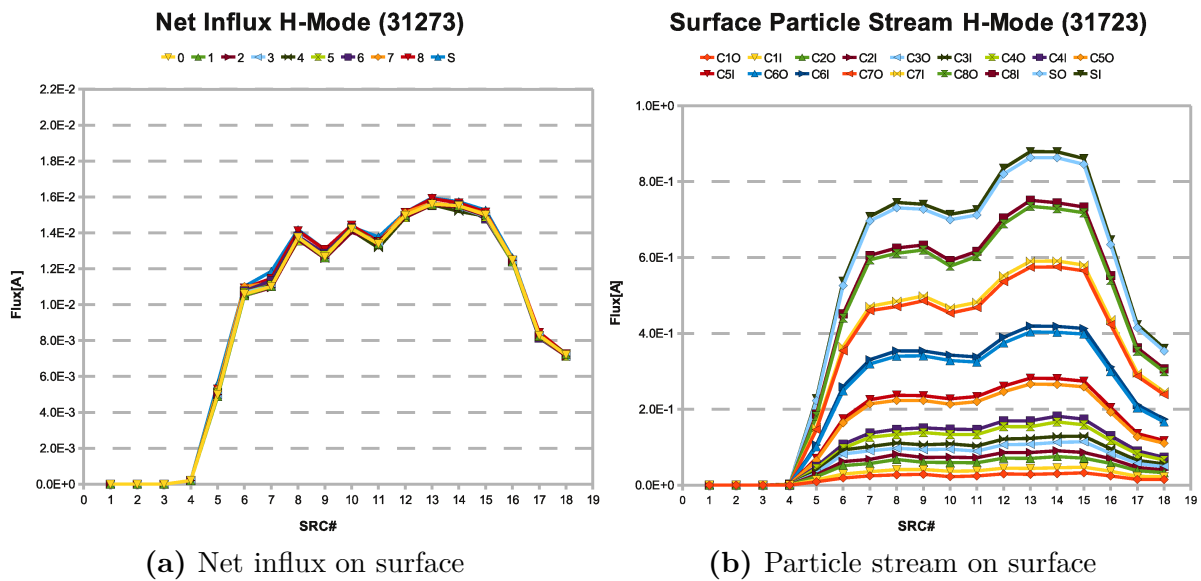


**Figure 4.18:** The net influxes and the particle streams crossing the surfaces for the standard case #31273 are shown. The particle stream and the net influx are not normalized to the surface area and are given in A. The legend is specified according to Fig. 4.17.

pendence of the net influx on the minor radius. While in H-Mode the net influx is approximately constant all over the radius, the L-Mode exhibits a clear decrease of the influx from the separatrix to the core boundary. This is consistent with the results in Sec. 4.2. In L-Mode only about half of the tungsten crossing the separatrix reaches the core boundary. This should reduce the impact of tungsten on the core plasma in L-Mode, because it reduces the tungsten impurity concentration in the innermost central region, which is most important for fusion reactions.

### Limiter Sources

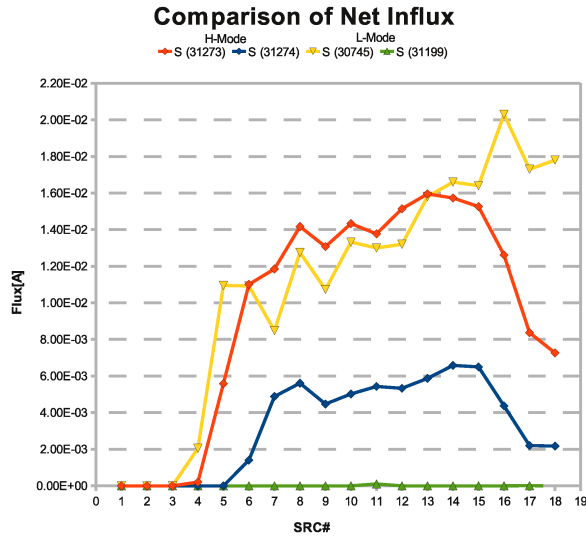
The tungsten density profiles for LFS limiter sources are similar to those of divertor sources with lower density. Additionally, the poloidal variations are less pronounced. The analysis of the penetration probability was done similar to the one for the divertor sources above. The results, however are different. The core penetration probability is strongly peaked around the HFS midplane sources 6, 7 and 8 in all examined simulations. The maximum gross penetration probability spans from 8 for the low-density L-Mode #30745 to 0.25 for the high-density H-Mode #31274. The maximum net penetration probability spans from 19.5% to 1.3% for the same dataset. The penetration probabilities are considerably larger than the divertor penetration probabilities with a maximum of 2%. Both, gross and net penetration probability profiles have the same structure with respect to the source number.

A decisive element in the penetration probability behavior seems to be the midplane. On the HFS, sources closest to and above the midplane show large penetration probabilities, whereas on the LFS the sources beneath the midplane exhibit larger penetration probabilities. The poloidal asymmetry of the penetration probability is significant. The #30745 L-Mode exhibits a difference in net penetration probability of a factor ranging from 20 to 50. The other simulations show the same magnitude of deviations.

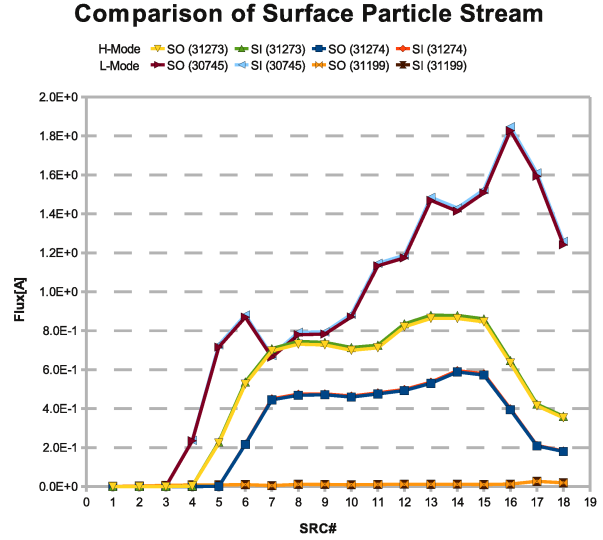
As for the divertor sources an increase in density seems to reduce the penetration probability considerably. A factor of 4.5 in the examined L-Mode simulations and a factor of 2.5 in the H-Mode simulations are achieved.

### Comparison

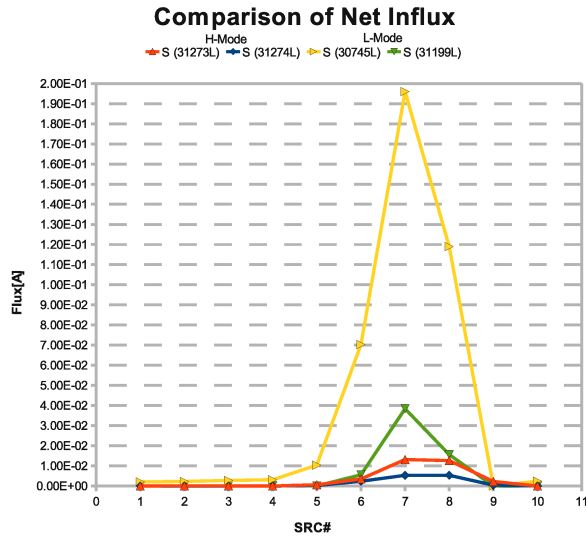
A compilation of all net and gross fluxes crossing the separatrix is shown in Fig. 4.19. A decrease of the penetration probability – of different intensity – for an increase in electron density at the separatrix can be observed. The characteristic behavior of the penetration probability with increasing divertor source number as well as for the different poloidal positions of the limiter sources is shown. Limiter sources above the midplane on the HFS are most disadvantageous for tungsten release.



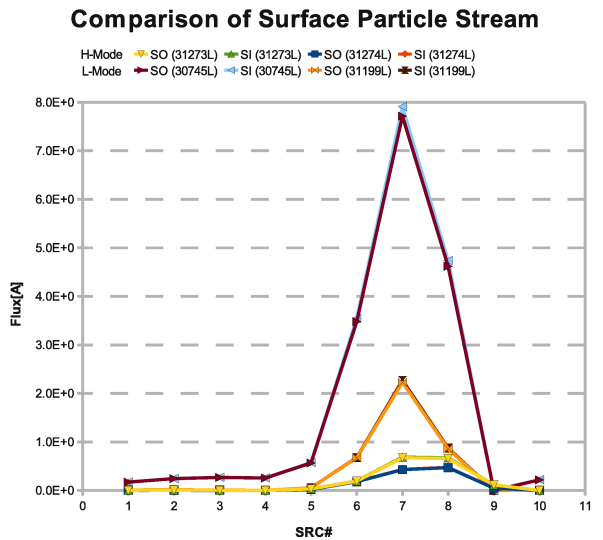
(a) Divertor - Net influx on separatrix



(b) Divertor - Particle stream over separatrix



(c) Limiter - Net influx on separatrix



(d) Limiter - Particle stream over separatrix

**Figure 4.19:** A comparison of the net influxes and the particle streams crossing the separatrix for different backgrounds and sources is shown. The particle stream and the net influx are not normalized to the surface area and are given in A.





# CHAPTER 5

---

## Summary & Outlook

---

### 5.1 Summary

The first part of this thesis is basically an introduction to EIRENE. Both aspects, the theoretical models and the code implementation are explained in detail. Apart from the code description, some code improvements were made in the course of this diploma thesis. They included an update on the sputtering routines, the introduction of a prompt redeposition routine, which checks for redeposition during the first gyration and improvement of the PROUSR coupling. The PROUSR coupling is now able to read either the electric potential or the Cartesian electric field components of the background plasma to supply the necessary electric field for the  $\vec{E} \times \vec{B}$  drift. The TIM functionality was further enhanced by adding a mock-up model of diffusion perpendicular to the magnetic field. It provides the means to include important transport processes in simulations and eliminates the limitation to pure banana transport. Benchmarks to other, diffusion dominated transport codes are now possible and anomalous transport effects can be accounted for in EIRENE simulations. The inclusion of the TIM comes with a steep increase of the need of computational resources. This requirement was met in a first approach by reinstating the parallel EIRENE version. Apart from code improvements the setup of an EIRENE simulation was atomized and a relatively simple process to prepare SOLPS and shotfile related data for the use in EIRENE simulations is provided.

The analysis of the simulation results of this thesis is divided into three main categories. First, a check of the applicability of the code for tungsten transport on AUG plasma backgrounds. The trace and gyroaverage assumptions were tested with respect to the employed background plasmas. The gyroaverage approximations of EIRENE was respected in most simulations on the entire simulation grid. However, an increased explicit integration threshold was necessary to achieve this due to a lack of thermalization of highly ionized tungsten ions. Highly ionized tungsten ions exhibited kinetic energies well above all background plasma temperatures. Temperature deviations up to factors of 20 to 1000 were observed. A direct connection to a known numerical singularity could not yet be established. However, the improvement of thermalization with an increase of the explicit integration threshold points in this direction. A correction of the tungsten temperature with directed motion of the tungsten particle was also not able to explain

the high temperature deviations. However, the temperature profiles at the targets improved when a directed tungsten motion at the speed of around 15% of the flow velocity of deuterium was assumed.

A benchmark of the TIM transport against the well-established NEOART code was performed. Neoclassical transport coefficients, calculated with NEOART, were used to deduce tungsten fluxes over closed flux surfaces from flux surface averaged EIRENE tungsten density profiles. The fluxes were compared to fluxes counted directly by EIRENE. The benchmark showed that EIRENE simulations only match the predicted fluxes of neoclassical banana transport at the separatrix and largely underestimates them towards the core. The shape of the flux profiles did not match either. NEOART results provided flux profiles with an almost exponential decrease of net influxes towards the core, whereas the EIRENE flux profiles were flat or even rising towards the core boundary.

The analysis of the penetration probability exhibited considerable core penetration probabilities of around 1% for divertor sources on the outer target from the strikepoint upwards. For L-Mode the penetration probability is largest at the upper boundary of the target. A favorable situation in regard of the target temperature and deuterium influx profiles measured by Langmuir probes for these simulations was found. Regions of high temperature and deuterium influx exhibit low penetration probabilities. For the studied H-Mode simulations the regions of maximum deuterium influx, maximum target temperature and the maximum core penetration probability coincides. Limiter source at the outer limiter and at the inner heat shield showed for all plasma backgrounds extremely peaked penetration probability profiles. Sources at the midplane on the HFS showed maximum penetration probabilities of around 20%, while for LFS sources and HFS sources above the midplane almost no core penetration of tungsten was observed. 10-20% higher separatrix electron densities reduced the penetration probabilities in L- and H-mode by factors of 2-4.

## 5.2 Outlook

Despite some still missing elements, like the lack of a validated spatial diffusion model, the general suitability of EIRENE for kinetic tungsten simulations was demonstrated. Further improvements of and future work on and with EIRENE can be divided in two parts.

### Simulations

A series of simulations and tests are encouraged by this thesis. Further tests on the thermalization behavior and transport benchmarks have to be performed. The influence of the numerical singularity has to be examined and corrected. Velocity spectra snapshots available with the TIM in time dependent mode could give additional information on the temperature properties of tungsten particles. The degree of Maxwellianization and directed parts of particle motion could be determined. A most crucial aspect in new simulations would be to guarantee better statistics by using the parallelized EIRENE. With more computational resources the impact of different surface model assumptions – especially sputtering – should be tested. Finally, the new spatial diffusion enables experimental validation simulations such as a laser blow-off simulation in order to compare the simulated residual time[82] of tungsten with experimental measurements.

### Code Improvements

To increase the accuracy of EIRENE results and improve the new ion tracing a variety of code improvements could be envisaged. First of all, a proper and validated model of spatial diffusion has to be implemented in EIRENE. This would include the the whole description of neoclassical transport into EIRENE and could be used as a mock-up model for anomalous diffusion. This would open up the possibility of a variety of benchmark against well-established codes, e.g. DIVIMP. The parallelization of EIRENE has to be further optimized in order to improve statistics and enable smaller TIM-time steps. The TIM-time step has to be automatically adapted to particle velocity, the magnetic field curvature and the accuracy requirements imposed by the numerical outward drift. Finally, a coupling to a fluid code could lead to a wide range of applications such as studies of ELM-effects on the tungsten transport.



---

## Bibliography

---

- [1] R.Dux. Impurity transport in tokamak plasmas. Technical Report IPP 10-27, Max-Planck-Institut für Plasmaphysik, Dec 2004.
- [2] R.Neu. Tungsten as a plasma facing material in fusion devices. Technical Report IPP 10/25, Max-Planck-Institut für Plasmaphysik, Dec 2003.
- [3] ASDEX-Upgrade Team. Technical Details ASDEX Upgrade. <http://www.ipp.mpg.de> (28.09.10).
- [4] D.Reiter et al. *The EIRENE Code User Manual*. Forschungszentrum Jülich, nov 2009.
- [5] J.Seebacher. Tim-manual. Private Communication, Apr 2008.
- [6] J.Seebacher. *Consistent kinetic trace impurity transport and chemistry modelling in fusion plasmas*. PhD thesis, Universität Innsbruck, 2009.
- [7] R.Schneider et al. Plasma edge physics with B2-Eirene. *Contrib. Plasma Phys.*, 46(1-2):3–191, jan 2006.
- [8] D.Reiser et al. Improved kinetic test particle model for impurity transport in tokamaks. *Nucl. Fus.*, 38(2):165–176, 1998.
- [9] D.Reiser. *Zur Anwendung der driftkinetischen Theorie in Monte-Carlo-Studien zum Verunreinigungstransport in Tokamak-Plasmen*. PhD thesis, Heinrich-Heine-Universität Düsseldorf, 1997.
- [10] A.G.Peeters et al. Reduced charge state equations that describe Pfirsch-Schlüter impurity transport in tokamak plasma. *Phys. of Plasmas*, 7(1):268–275, Jan 2000.
- [11] R.Dux and A.G.Peeters. Neoclassical impuriy transport in the core of an ignited tokamak plasma. *Nucl. Fus.*, 40(10):1721–1729, 2000.
- [12] DOE. *Annual Energy Outlook 2010*, volume DOE/EIA-0383(2010) of *Annual Energy Outlook*. U.S. Energy Information Administration, Apr 2010.
- [13] IEA. *Key World Energy Statistics 2010*. Key World Energy Statistics. International Energy Agency, 2010.

- [14] M.Scott. Russia-ukraine gas conflict hits europe. *Buisnessweek*, Jan 2009.
- [15] British Petroleum. *Statistical Review of World Energy*. British Petroleum, 2010.
- [16] R.Gold and A.Davis. Oil officials see limit looming on production. *The Wall Street Journal*, Nov 2007.
- [17] M.Parry et al. *Climate Change 2007: Impacts, Adaptation and Vulnerability*, volume 4 of *Assessment Report of the Intergovernmental Panel on Climate Change*. Cambridge University Press, 2007.
- [18] S.Solomon et al. *Climate Change 2007: The Physical Science Basis*, volume 4 of *Assessment Report of the Intergovernmental Panel on Climate Change*. Cambridge University Press, 2007.
- [19] B.Metz et al. *Climate Change 2007: Mitigation of Climate Change*, volume 4 of *Assessment Report of the Intergovernmental Panel on Climate Change*. Cambridge University Press, 2007.
- [20] EFDA. Fusion as an energy source. <http://www.efda.org> (20.10.10).
- [21] NASA. Average nucleus binding energy. <http://www.nasa.gov> (28.09.10).
- [22] P.Aubert et al. Low activation steels welding with PWHT and coating for ITER test blanket modules and DEMO. *J. Nucl. Mater.*, pages –, 2010.
- [23] A.Tavassoli et al. Materials design data for reduced activation martensitic steel type EUROFER. *J. Nucl. Mater.*, 329-333:257–262, 2004. Proceedings of the 11th International Conference on Fusion Reactor Materials (ICFRM-11).
- [24] N. Baluc et al. Status of reduced activation ferritic/martensitic steel development. *J. Nucl. Mater.*, 367-370:33–41, 2007.
- [25] D.Steiner et al. Helium-3 blankets for tritium breeding in near-term fusion devices. *Fusion Engineering and Design*, 8:121–125, 1989.
- [26] H.Kawamura et al. Application of beryllium intermetallic compounds to neutron multiplier of fusion blanket. *Fus. Eng. Design*, 61-62:391–397, 2002.
- [27] K.Tanaka. Summary of inertial fusion sessions. *Nucl. Fus.*, 49, Sep 2009.
- [28] F.Sommer. Charakterisierung und Interpretation von MHD Aktivität zwischen ELMs am Tokamak ASDEX Upgrade. Master’s thesis, Technische Universität München, 2009.
- [29] P.Stangeby. A tutorial on some basic aspects of divertor physics. *Plasma Phys. Control. Fusion*, 42:B271–B291, 2000.
- [30] M.Wischmeier. *Simulating Divertor Detachment in the TCV and JET Tokamak*. PhD thesis, École Polytechnique Fédérale de Lausanne, 2004.

- [31] J. Roth et al. Divertor retention for recycling impurities. *Nucl. Fus.*, 32(10):1835, 1992.
- [32] R. Arnoux. How Fritz Wagner "discovered" the H-Mode. *iter newslines*, (86), Jun 2009.
- [33] E. Doyle et al. Plasma confinement and transport. *Nucl. Fus.*, 47:18–127, 2007.
- [34] M. Keilhacker. JET D–T Experiments and their implications for ITER. 17th SOFE Conference San Diego 1997, Oct 1997.
- [35] R. Dux et al. Plasma-wall interaction and plasma behaviour in the non-boronised all tungsten ASDEX Upgrade. *J. Nucl. Mater.*, 2009.
- [36] K. Krieger. Conclusions about the use of tungsten in the divertor of ASDEX Upgrade. *J. Nucl. Mater.*, 266-269:207–216, 1999.
- [37] K. Hoshino et al. Accumulation process of high-z impurity in toroidal rotating tokamak plasma. *Contrib. Plasma Phys.*, 50(3–5):386–391, 2010.
- [38] T. Pütterich. *Investigations on Spectroscopic Diagnostic of High-Z Elements in Fusion Plasmas*. PhD thesis, Universität Augsburg, Apr 2006.
- [39] T. Pütterich et al. Calculation and experimental test of the cooling factor of tungsten. *Nucl. Fus.*, 50:9, 2010.
- [40] J. Roth et al. Recent analysis of key plasma wall interactions issues for ITER. *J. Nucl. Mater.*, (390-391):1–9, 2009.
- [41] A. Kallenbach et al. Scrape-off layer radiation and heat load to the ASDEX Upgrade LYRA divertor. *Nucl. Fus.*, 30(7):901–917, 1999.
- [42] R. Behrisch. Material erosion at the vessel walls of future fusion devices. *J. Nucl. Mater.*, 313-316:388–392, 2003.
- [43] M. Reich. *A new diagnostic for ASDEX Upgrade edge ion temperatures by lithium-beam charge exchange recombination spectroscopy*. PhD thesis, Ludwig-Maximilians-Universität München, 2005.
- [44] M. Mattioli. Laser blow-off injected impurity particle confinement times in JET and Tore Supra. *Nucl. Fus.*, 35(9):1115, 1995.
- [45] M. Janzer et al. Investigating tungsten transport in the plasma edge of ASDEX Upgrade. Presentation at 37th EPS Conference on Plasma Physics 2010 in Dublin, Apr 2010.
- [46] P. T. Lang et al. ELM frequency control by continuous small pellet injection in ASDEX Upgrade. *Nucl. Fus.*, 43(10):1110, 2003.



- [47] H.Urano et al. Energy and particle losses during type-I ELMy H-Mode in ASDEX Upgrade. *Plas. Phys. Control. Fus.*, 45:1571–1596, 2003.
- [48] J.Strachan. JET radiative mantle experiments in ELMy H-Mode. *Plas. Phys. and Control. Fus.*, 42:A81–A88, 2000.
- [49] K.Schmid. Impact of gyro-motion and sheath acceleration on the flux distribution on rough surfaces. Private Communication.
- [50] J.Greenwood. The correct and incorrect generation of a cosine distribution of scattered particles for monte-carlo modelling of vacuum systems. *Vacuum*, 67:217–222, 2002.
- [51] E.K.Hollmann et al. Monte-carlo simulation of the particle transport during physical vapour deposition of ceramic superconductors. *Physica C*, (425):101–110, 2005.
- [52] W.Eckstein et al. Sputtering data. Technical Report IPP 9/82, Max-Planck-Institut für Plasmaphysik, February 1993.
- [53] W.Eckstein et al. New fit formulae for the sputtering yield. *J. Nucl. Mater.*, (320):209–213, 2003.
- [54] R.Behrisch and W.Eckstein. *Sputtering by Particle Bombardement*, volume 110 of *Topics in Applied Physics*, chapter 3, pages 33–189. Springer-Verlag Berlin Heidelberg, 2007.
- [55] The TRIM code surface database. <http://www.eirene.de/manuals/trim.pdf> (06.10.10).
- [56] J.Roth. Chemical erosion of carbon based materials in fusion science. *J. Nucl. Mater.*, 266-269:51–57, 1999.
- [57] J.Roth. *Review and Status of Physical Sputtering and Chemical Erosion of Plasma Facing Materials*, volume 75 of *Springer Series in Chemical Physics*. Springer-Verlag Berlin Heidelberg, 2005.
- [58] R.Dux. Effektive Sputterausbeute von W bei prompter Redeposition. Private Communication.
- [59] R.Dux. Neoclassical transport - European PHD-network Lecture 2009. Presentation, 2009.
- [60] P.Helander and D.Sigmar. *Collisional Transport in Magnetized Plasmas*. Cambridge Monographs on Plasma Physics. Cambridge University Press, 1 edition, Oct 2005.
- [61] R.Balescu. *Classical Transport Theory*, volume 1 of *Transport Processes in Plasmas*. Elsevier Science Publishers B.V., 1 edition, 1988.

- [62] M.Sertoli. *Local Effects of ECRH on Argon Transport at ASDEX Upgrade*. PhD thesis, Ludwig-Maximilians-Universität München, May 2010.
- [63] S.Günther. Introduction to Plasma Physics - University Lecture 2008. Presentation, 2008. Lecture Notes from University lecture given at Technische Universität München in 2008.
- [64] J.Fuchs and W.Schneider. Routines and tools for working with equilibria data, 2010.
- [65] F.L.Hinton and R.D.Hazeltine. Theory of plasma transport in toroidal confinement systems. *Rev.Mod.Phys.*, 48(2):239–308, Apr 1976.
- [66] O.Garcia et al. Fluctuations and transport in the TCV scrape-off layer. *Nucl. Fus.*, 47:667–676, Jun 2007.
- [67] V.Naulin. Turbulent transport and the plasma edge. *J. Nucl. Mater.*, 363-365:24–31, 2007.
- [68] H.P.Summers, W.J.Dickson, et al. Ionisation state, excited populations and emission of impurities in dynamic finite density plasmas. I: the generalised collisional-radiative model for light elements, 2005.
- [69] H.P.Summers. The ADAS User Manual (2004), Version 2.6. <http://www.adas.ac.uk/manual.php> (25.08.2010), 2004.
- [70] H.P.Summers. Atomic data for modelling fusion and astrophysical plasmas. *Plasma Phys. Control. Fusion*, 44:B323–B338, 2002.
- [71] S. D. Loch et al. Electron-impact ionization of atomic ions in the W isonuclear sequence. *Phys. Rev. A*, 72(5):052716, 2005.
- [72] D.E.Post et al. Calculations of energy losses due to atomic processes in tokamaks with applications to the international thermonuclear experimental reactor divertor. *Phys. Plasmas* 2, (2328), 1995.
- [73] D.E.Post et al. *At. Data Nucl. Data Tables* 20, (397), 1977.
- [74] T.Pütterich et al. Modelling of measured tungsten spectra from ASDEX Upgrade and predictions for ITER. *Plasma Phys. Control. Fusion*, 50(8):085016, 2008.
- [75] H.Frerichs. 3D numerische Parameterstudien zum Verunreinigungstransport in TEXTOR-DED. Master’s thesis, Forschungszentrum Jülich, 2010.
- [76] W.Eckstein. Physical sputtering and reflection processes in plasma-wall interactions. *J. Nucl. Mater.*, 248:1–8, 1997.
- [77] W.Eckstein. *Computer Simulation of Ion-Solid Interactions*. Springer-Verlag, 1st edition, 1991.

- [78] D.Reiter et al. Database for recycling and penetration of neutral helium atoms in the boundary of a fusion plasma. Technical Report Jül-2605, Forschungszentrum Jülich, Apr 1992.
- [79] W.Eckstein and D.Heifetz. Data sets for hydrogen reflection and their use in neutral transport calculations. *J. Nucl. Mater.*, 145-147:332–338, 1987.
- [80] Y.Feng et al. 3D fluid modelling of the edge plasma by means of a Monte Carlo technique. *J. Nucl. Mater.*, 266-269:812–818, 1999.
- [81] Y.Feng et al. A 3D Monte Carlo code for plasma transport in island divertors. *Journal of Nuclear Materials*, 241-243:930–934, 1997.
- [82] T. Lunt et al. 3d modeling of the asdex-upgrade edge plasma exposed to a localized tungsten source by means of emc3-eirene. *J. Nucl. Mater.*, 2010. Presented at PSI in Sofia 2009.
- [83] H.Goedbloed and S.Poedts. *Principles of Magnetohydrodynamics*. Cambridge University Press, 2004.
- [84] K.Schmid et al. DIVIMP modeling of tungsten impurity transport in ITER. *J. Nucl. Mater.*, (363-365):674–679, 2007.
- [85] A.Geier et al. Modeling of tungsten transport in the SOL for sources at the central column of ASDEX Upgrade using DIVIMP. *J. Nucl. Mater.*, (313-316):1216–1220, 2003.
- [86] K.Hoshino et al. High-Z impurity transport code by monte-carlo method in a realistic tokamak geometry - IMPGYRO -. *Contrib. Plasma Phys.*, 48(1–3):280–284, 2008.
- [87] K.Hoshino et al. Numerical analysis of incident angle of heavy metal impurity to plasma facing components by impgyro. *J. Nucl. Mater.*, 390-391:168–171, 2009.
- [88] J.Heikkinen et al. Particle simulation of the neoclassical plasmas. *J. Comp. Phys.*, 173:527–548, 2001.
- [89] J.Spanier and E.Gelbard. *Monte-Carlo Principles and Neutron Transport Problems*. Addison-Wesley Pub. Comp., 1980.
- [90] D. Reiter et al. Detailed atomic, molecular and radiation kinetics in current 2D and 3D edge plasma fluid codes. *J. Nucl. Mater.*, 363-365:649–657, 2007. Plasma-Surface Interactions-17.
- [91] J.D.Huba. *NRL Plasma Formulary 2009*. Naval Research Laboratory, 1 edition, 2009.
- [92] P.McCarthy. Analytical solutions to the Grad-Shafranov equation for tokamak equilibrium with dissimilar source functions. *Phys. of Plas.*, 6(9):3554–3560, Sep 1999.

- [93] W.Schneider et al. ASDEX Upgrade MHD equilibria reconstruction on distributed workstations. *Fus. Eng. Design*, 48:127–134, 2000.
- [94] MDSplus - Introduction. <http://www.mdsplus.org> (28.09.10).
- [95] V.Kotov et al. Numerical study of the ITER divertor plasma with the B2-EIRENE ode package. Technical Report Jül-4257, Forschungszentrum Jülich, Nov 2007.
- [96] R.Schneider et al. *Plasma Edge Physics with B2-Eirene*, volume 46 of *Contrib. Plasma Phys.*, chapter 1–2, pages 3–191. Wiley-VCH Verlag, 2006.
- [97] J.Seebacher et al. EDGE2D-EIRENE study on tungsten fluid vs. tungsten kinetic. *37th EPS Conference on Plasma Physics*, 2010.
- [98] I.Bronstein. *Handbook of Mathematics*. Springer-Verlag, 5 edition, 2007.
- [99] C.Gardiner. *Handbook of Stochastic Methods*. Springer-Verlag, 2 edition, ???
- [100] D.Reiter. *The Monte-Carlo Method for Particle Transport Problems*, volume 739 of *Lect. Notes Phys.*, pages 141–158. Springer-Verlag, 2008.



# APPENDIX A

---

## Appendix

---

### A.1 EIRENE Standard Input

The standard input parameters given in Tab. A.1 are explained in the following list and can be found in[4; 5]:

- Drift-Flags - The Drift-Flags are in reality drift coefficients, which scale the drift effects. In this thesis they were used as flags with a values of either 0 or 1.
- Diffusion-Flag - Activates the spatial diffusion contribution.
- FKP-Flag - Activates the Fokker-Planck collision operator.
- 13-Moments-Correction-Flag - Activates the 13-moment correction of the gyroaveraging description[61].
- Ion-Electron-Collisions-Flag - Activates the consideration of ion-electron collisions in the Fokker-Planck operator.
- Implicit- $k_{perp}$ -Flag - Activates the implicit integration scheme in order to reduce the effects of the numerical singularity in the Trubnikov-Rosenbluth potentials[6].
- $D_{eff}$ -Flag - Activates the description of velocity diffusion in the Fokker-Planck operator with an effective diffusion coefficient.
- TIM-timestep - Time step between recalculations of the particle velocity for the linear displacement in between TIM-time steps. The numerical drift is critically determined by the TIM-timestep.
- Time surface interval - Restriction of the simulated physical time.
- Sputtering-Flag - Activates Sputtering

- Reflection-Flag - Activates Reflection at the walls. If inactive particles are absorbed and stopped at all wall elements.

EIRENE-Input Variable	Value	EIRENE-Input Variable	Value
<i>Coulomb Collisions (FKP):</i>		<i>Drifts:</i>	
FKP-Flag	1	$\vec{E} \times \vec{B}$ -Flag	1
13-Moments-Correction-Flag	1	gradB-Flag	1
Ion-Electron-Collisions-Flag	0	curvB-Flag	1
Implicit- $k_{perp}$ -Flag	1	Diffusion-Flag	0
$D_{eff}$ -Flag	1		
Colliding Background-Species	D, He, C		
<i>Time-Characteristics:</i>		<i>Surface-Model:</i>	
TIM-timestep	$10^{-7}$ s	Sputtering-Flag	0
Time surface interval	20 ms	Reflection-Flag	0

**Table A.1:** EIRENE-Input settings for standard cases. The input parameters are explained in [4; 5].

## A.2 EIRENE Source coordinates & Divertor Target Langmuir Data

The following table shows the coordinates of the EIRENE sources of tungsten specified in the EIRENE input file.

No.	Coordinates	No.	Coordinates	No.	Coordinates
<i>Divertor Sources (s-coordinate [m])</i>					
1	0.0132 - 0.0102	7	0.0020 - 0.0010	13	0.0132 - 0.0212
2	0.0102 - 0.0071	8	0.0010 - 0.0003	14	0.0212 - 0.0334
3	0.0071 - 0.0051	9	0.0003 - 0.0000	15	0.0334 - 0.0506
4	0.0051 - 0.0041	10	0.0000 - 0.0030	16	0.0506 - 0.0760
5	0.0041 - 0.0030	11	0.0030 - 0.0071	17	0.0760 - 0.1205
6	0.0030 - 0.0020	12	0.0071 - 0.0132	18	0.1205 - 0.2208
<i>Limiter Sources (x/y-coordinate [m])</i>					
<i>outer Limiter</i>		<i>inner Heatshield</i>			
1	2.1510/ 0.4590	6	1.1560/ 0.7361		
2	2.1990/ 0.1629	7	1.0840/ 0.4370		
3	2.1640/-0.1494	8	1.0460/ 0.0973		
4	1.9940/-0.5250	9	1.0500/-0.2443		
5	2.0850/-0.3681	10	1.1060/-0.5481		

**Table A.2:** Source coordinates for standard cases.

The following two figures show the Langmuir probes data collected during the AUG shots #23029 and #21372. We concentrate on LFS sources in this thesis.

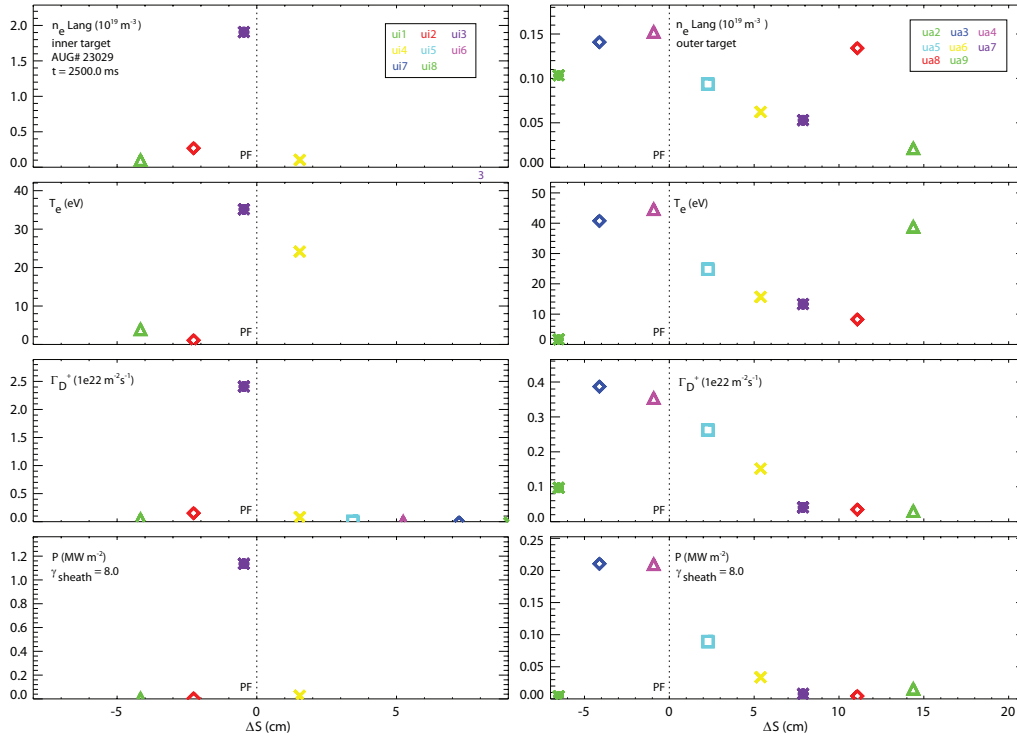


Figure A.1: Langmuir probe data for AUG shot #23029.

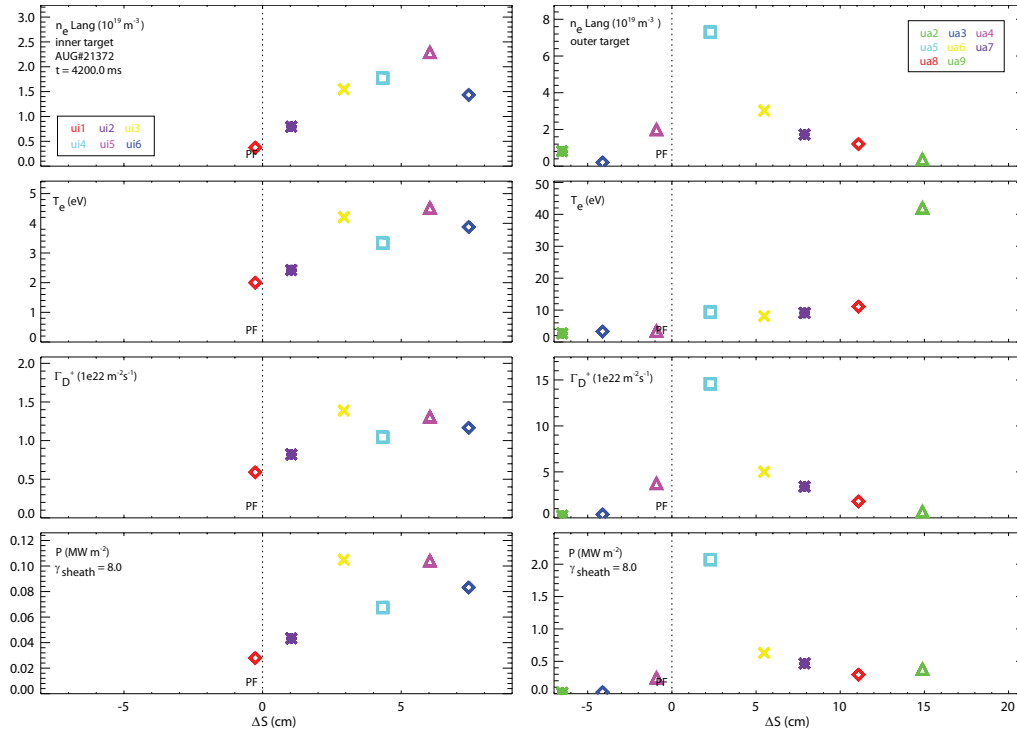


Figure A.2: Langmuir probe data for AUG shot #21372.



### A.3 Plasmaprofiles

Background Tallies - SOLPS Shot 30745

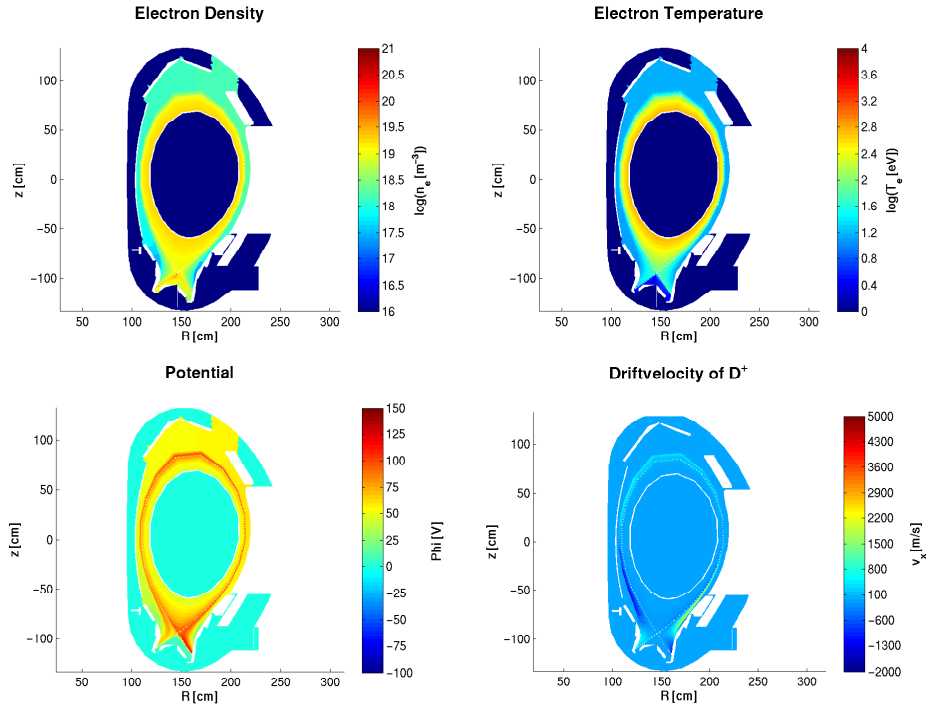


Figure A.3: Background profiles for the SOLPS shot #30745.

Background Tallies - SOLPS Shot 31199

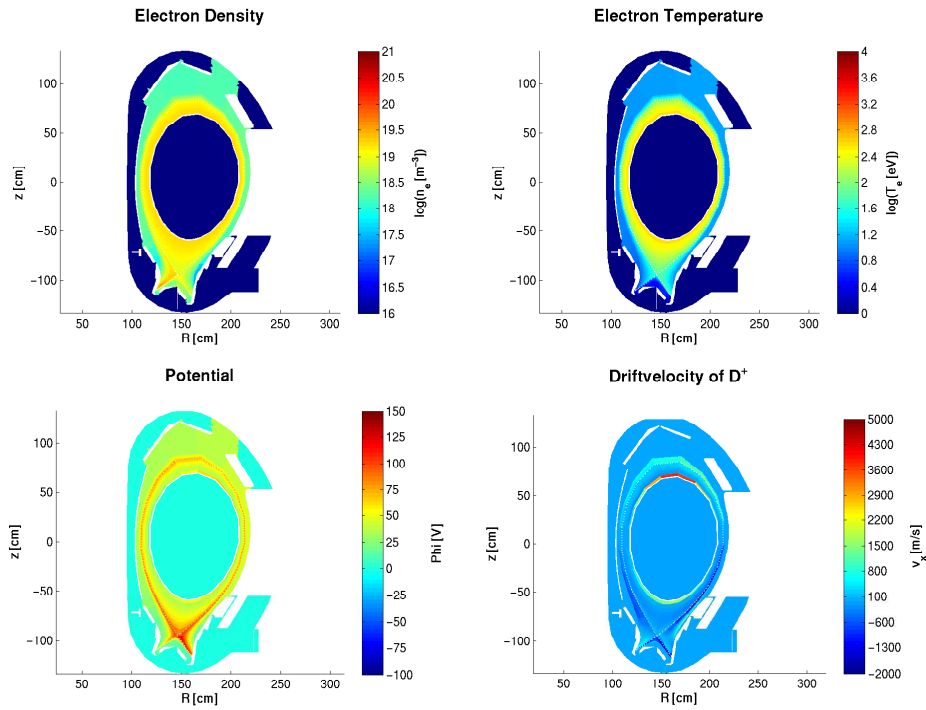
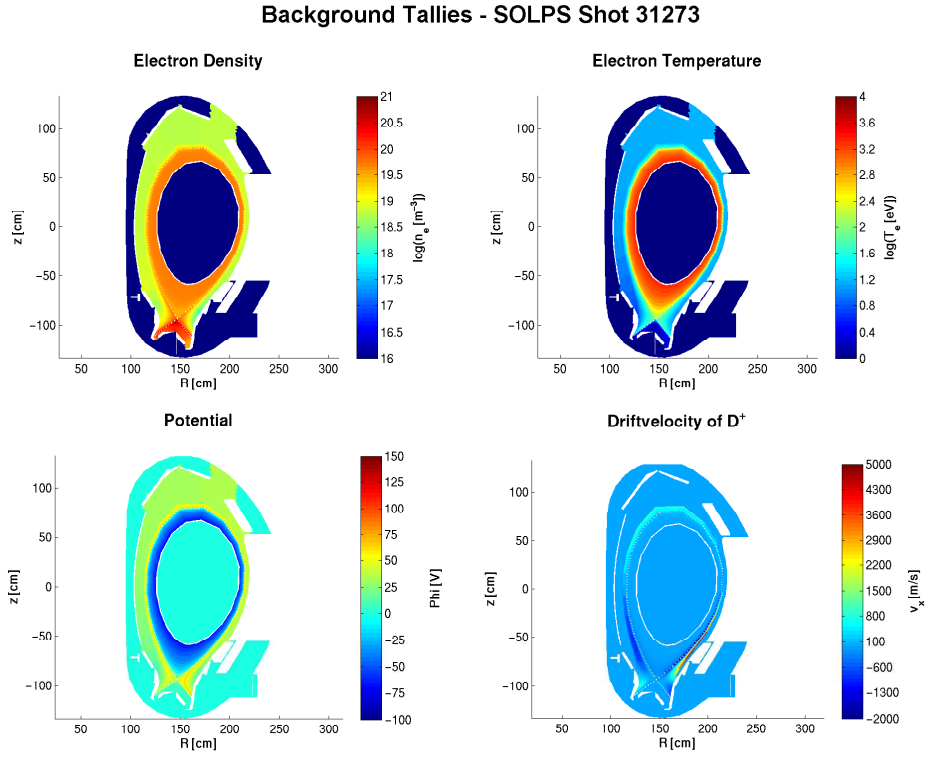
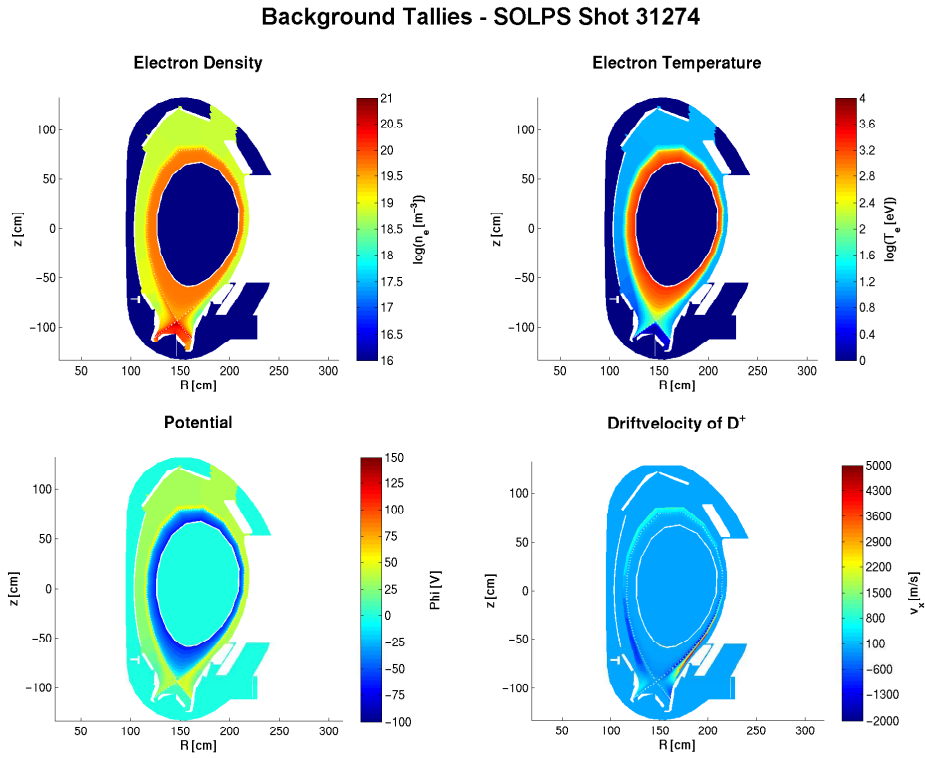


Figure A.4: Some important background quantities for the SOLPS shot #31199.



**Figure A.5:** Some important background quantities for the SOLPS shot #31273.



**Figure A.6:** Some important background quantities for the SOLPS shot #31274.

SOLPS Index	#30745	#31273	#31199	#31274
Plasma Type	L-Mode	H-Mode	L-Mode	H-Mode
Related Magnetic Equilibrium (AUG)	23029	21372	23029	21372
Shot Time of Equilibrium [s]	2.5	4.2	2.5	4.2
Divertor Configuration	DivIIb	DivIIb	DivIIb	DivIIb
Grid (nx,ny)	50,20	50,20	50,20	50,20
Simulated Species	D, C, He	D, C, He	D, C, He	D, C, He
Outer Midplane Separatrix Electron Temperature [eV]	85	143	74	135
Outer Midplane Separatrix Ion Temperature [eV]	160	279	67	249
Outer Midplane Separatrix Electron Density [m <sup>-3</sup> ]	$7.8 \times 10^{18}$	$2.8 \times 10^{19}$	$8.2 \times 10^{18}$	$3.2 \times 10^{19}$
Ion Energy Flux (Core>SOL) [eVm <sup>-2</sup> s <sup>-1</sup> ]	372630	2646740	119240	2616880
Electron Energy Flux (Core>SOL) [eVm <sup>-2</sup> s <sup>-1</sup> ]	559950	4954250	419160	5054180
Ion Particle Flux (Core>SOL) [m <sup>-3</sup> ]	$3.4 \times 10^{21}$	$8.4 \times 10^{21}$	$3.5 \times 10^{21}$	$8.6 \times 10^{21}$
Electron Particle Flux (Core>SOL) [m <sup>-3</sup> ]	$3.4 \times 10^{21}$	$8.7 \times 10^{21}$	$3.7 \times 10^{21}$	$8.7 \times 10^{21}$

**Table A.3:** Characteristic parameters of the SOLPS simulations of the employed background plasmas[94].

## A.4 EIRENE Program Flowcharts

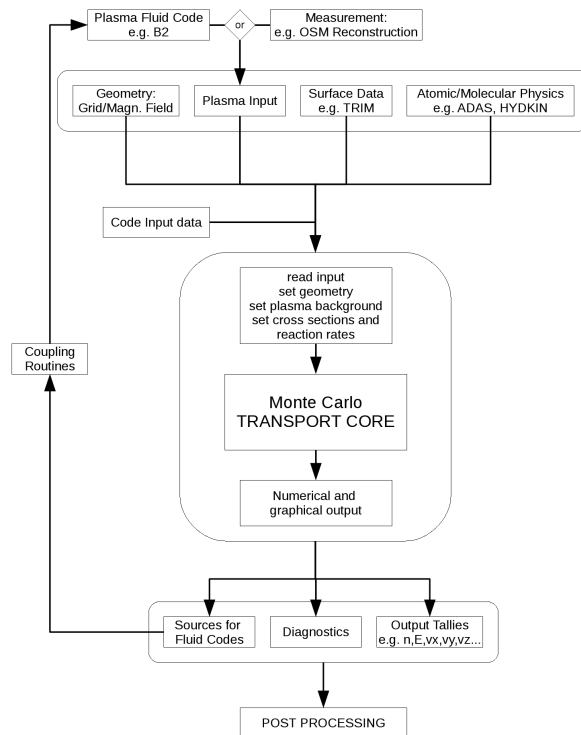


Figure A.7: General EIRENE program flow[6, p.23]

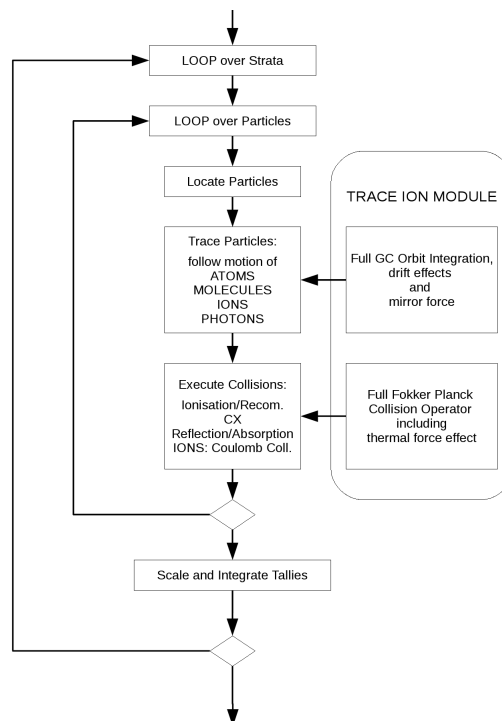


Figure A.8: New EIRENE transport core (TIM included)[6, p.24]

## A.5 Derivation of Monte-Carlo Transport Calculations

Basic quantities in Monte-Carlo procedures are the standard tools of probability theory, like the expectation value  $E$  and the standard deviation  $\sigma$ , which are both dependent on the probability measure  $p$ .

$$\begin{aligned} E(X) &= \int_{\Omega} dp X \\ \sigma^2(X) &= \int_{\Omega} dp (X - E(X))^2 \end{aligned} \quad (\text{A.1})$$

One usually does not have direct access to these theoretical exact value, but the common estimators are to be used instead. The arithmetic mean  $I_N$  and the empirical variance  $s$  are readily calculated and replace the expectation value and the standard deviation for practical means.

$$\begin{aligned} I_N &= \frac{1}{N} \sum_{i=1}^N X(\omega_i) \\ s^2 &= \frac{1}{N-1} \sum_{i=1}^N (X(\omega_i) - I_N)^2 \end{aligned} \quad (\text{A.2})$$

Both these quantities converge to the theoretical quantities for  $N \rightarrow \infty$ . Further reading on probability theory can be found in [98][99]. To actually implement Monte-Carlo methods, a necessary ingredient are (pseudo<sup>1</sup>) random numbers in order to be able to simulate 'randomness' in an otherwise deterministic apparatus[89]. The following paragraph will focus on transport simulations as a possible application of Monte-Carlo routines.

The presented derivation of the basic equation follows the description for neutral particle transport found in [95, p.19ff]. Further reading in [4; 89; 100].

As mentioned above the primary objective in kinetic modelling is to retrieve the one-particle distribution function  $f(\vec{r}, \vec{v}, t)$  and follow its evolution with given boundary conditions. The Boltzmann kinetic equation is used as a starting point.

$$\begin{aligned} \partial_t f(\vec{v}) + \vec{v} \cdot \nabla_{\vec{r}} f(\vec{v}) &= \iiint \sigma(\vec{v}', \vec{V}'; \vec{v}, \vec{V}) \left| \vec{v}' - \vec{V}' \right| f(\vec{v}') f_b(\vec{V}') \\ &\quad - \sigma(\vec{v}, \vec{V}; \vec{v}', \vec{V}') \left| \vec{v} - \vec{V} \right| f(\vec{v}) f_b(\vec{V}) d^3v' d^3V' d^3V \end{aligned} \quad (\text{A.3})$$

where  $f_b$  is the background one-particle distribution and  $\sigma$  is the collision cross-section. No external forces are taken into account for neutrals. The simplified Boltzmann equation accounting for multiple particle species ( $i$ ) can be transformed to

$$\partial_t f_i + \vec{v} \cdot \nabla_{\vec{r}} f_i + \nu_i(\vec{r}, \vec{v}) f_i = \int C(\vec{r}; \vec{v}', i' \rightarrow \vec{v}, i) \left| \vec{v}' - \vec{V}' \right| f_i d^3v' + Q_i(\vec{r}, \vec{v}, t) \quad (\text{A.4})$$

---

<sup>1</sup> Pseudo means that given a seed for the random number generation the sequence of random numbers is exactly determined, but the sequence itself behaves randomly. This is necessary to be able to debug and retrace calculations for validation or repetition of the 'experiment'.

where  $C(\vec{r}; \vec{v}', i' \rightarrow \vec{v}, i)$  is the collision kernel giving the number of particles of species  $i$  with velocity  $\vec{v}$  emerging from collision of particles  $i'$  with velocity  $\vec{v}'$ ,  $Q_i$  is the (primary) source of particles  $i$  with velocity  $\vec{v}$  and  $\nu_i$  is the total collision frequency giving the number of collisions for particles  $i$  with velocity  $\vec{v}$  during a unity time interval. The expressions can be evaluated from

$$\begin{aligned}\nu_i^t &= \sum_k \nu_{i,k}(\vec{r}, \vec{v}) \\ \nu_{i,k}(\vec{r}, \vec{v}) &= \iiint \sigma(\vec{v}, \vec{V}; i; \vec{v}', \vec{V}', i') |\vec{v} - \vec{V}| f_b(\vec{V}) d^3v' d^3V' d^3V \\ C(\vec{r}; \vec{v}', i' \rightarrow \vec{v}, i) &= \sum_k \nu_{i',k}(\vec{r}, \vec{v}') c_k(\vec{r}; \vec{v}', i' \rightarrow \vec{v}, i) \\ c_k(\vec{r}; \vec{v}', i' \rightarrow \vec{v}, i) &= \frac{\iint \sigma(\vec{v}', \vec{V}', i'; \vec{v}, \vec{V}, i) |\vec{v}' - \vec{V}'| f_b(\vec{V}') d^3V' d^3V}{\iiint \sigma(\vec{v}', \vec{V}', i'; \vec{v}, \vec{V}, i) |\vec{v}' - \vec{V}'| f_b(\vec{V}') d^3V' d^3V d^3v'}\end{aligned}\tag{A.5}$$

The total collision frequency is determined by summing up the collision frequencies for all possible processes. This may include surface and volume processes of very different nature as well as absorption, which can be implemented as a transition to an 'empty' speciem. Equation (A.4) can be transformed into a Fredholm integral of second kind. This approach is used for rigorous mathematical description and not pursued any further here.

$$\begin{aligned}\Psi_i(\vec{r}; \vec{v}) &= \int \underbrace{Q_i(\vec{r}'; \vec{v})}_{\text{Birth}} \underbrace{T_i(\vec{v}; \vec{r}' \rightarrow \vec{r})}_{\text{Free Flight}} d^3r' \\ &+ \sum_{i'} \iint \Psi_{i'}(\vec{r}'; \vec{v}') \underbrace{C(\vec{r}'; \vec{v}', i' \rightarrow \vec{v}, i)}_{\text{Collision Event}} \underbrace{T_i(\vec{v}; \vec{r}' \rightarrow \vec{r})}_{\text{Free Flight}} d^3r' d^3v'\end{aligned}\tag{A.6}$$

where  $\Psi$  is the (pre-)collision density distribution[100]. In EIRENE all terms in the Fredholm integral equation are sampled by different routines explained later on in the subsections 3.2.4 - 'Source' (Birth), 3.2.5 - 'Transport' (Free Flight) and 3.2.6 - 'Reactions' (Collisions).

In order to calculate the moments of the one-particle distribution function – in EIRENE the distribution function is never actually calculated – the track-length estimator has been used.

An estimate of a moment is calculated by

$$R = \frac{1}{N} \sum_{i=1}^N X(\omega_i)\tag{A.7}$$

where the function  $X(\omega)$  depends on the type of estimator. The track-length estimator is defined by

$$X_T(\omega) = \sum_{j=1}^n \int_{x_j}^{x_{j+1}} \frac{ds}{|\vec{v}(s)|} w(s) g_t(s)\tag{A.8}$$

where  $w(s)$  is the statistical weight,  $g_t(s)$  is the detector function determining the resulting moment and  $s$  is the track-length variable between the collision points  $x_j$  and  $x_{j+1}$ . The track-length estimator gives an unbiased estimation of the moment of the

distribution function according to

$$\int f(\vec{r}, \vec{v}, t) g_t(\vec{r}, \vec{v}, t) d^3v \quad (\text{A.9})$$

For the sake of completeness it shall be mentioned that in EIRENE the collision estimator given by

$$X_C(\omega) = \sum_{j=1}^n g_c(x_j) w(x_j) \quad (\text{A.10})$$

is also implemented.

Weight functions are used to introduce so-called non-analog sampling methods such as Russian-Roulette or splitting in order to improve statistics while cutting computational time. However, we use purely analog sampling ( $w = 1$ ) throughout this work and will not deal with theoretical issues connected to non-analog sampling.

## A.6 SOLPS Fluid Equations

The basic fluid equations integrated into SOLPS are presented in this section. The so called Braginskii equations form the basis of SOLPS calculations. Starting with the continuity equation for electrons ( $x = e$ ) and ions ( $x = i$ ) responsible for the balance of particles with densities  $n_x$ , flow velocities  $\vec{v}_x$  and particle source terms  $S_n^x$ .

$$\partial_t n_x + \nabla \cdot (\vec{v}_x n_x) = S_n^x \quad (\text{A.11})$$

The momentum equation for ions

$$\partial_t (m_i n_i \vec{v}_i) + \nabla \cdot (m_i n_i \vec{v}_i) = -\nabla p_i - \nabla \cdot \overleftrightarrow{\Pi}_i + q_i n_i (\vec{E} + \vec{v}_i \times \vec{B}) + \vec{R}_i + \vec{S}_p^i \quad (\text{A.12})$$

and for electrons

$$-\nabla p_e - q_e n_e (\vec{E} + \vec{v}_e \times \vec{B}) + \vec{R}_e = 0 \quad (\text{A.13})$$

where  $S_p^x$  is the momentum source term and the friction force  $R_x$  defined by

$$\vec{R}_e = -\vec{R}_i = e n_e \left( \frac{j_{\parallel}}{\sigma_{\parallel}} + \frac{j_{\perp}}{\sigma_{\perp}} \right) - 0.71 n_e \nabla_{\parallel} T_e - \frac{3 q_e n_e^2}{2 \sigma_{\perp} B^2} \vec{B} \times \nabla T_e \quad (\text{A.14})$$

is responsible for maintaining the momentum balance. The total electric current is given by

$$\vec{j} = (q_i n_i \vec{v}_i - q_e n_e \vec{v}_e) \quad (\text{A.15})$$

The summed up total momentum equations then reads

$$\partial_t (m_i n_i \vec{v}_i) + \nabla \cdot (m_i n_i \vec{v}_i) = -\nabla p - \nabla \cdot \overleftrightarrow{\Pi}_i + \vec{j} \times \vec{B} \vec{S}_p^i \quad (\text{A.16})$$

Eventually, there are the energy equations for ions

$$\partial_t \left( \frac{3}{2} n_i T_i + \frac{m_i n_i}{2} \vec{v}_i^2 \right) + \nabla \cdot \left( \left( \frac{5}{2} n_i T_i + \frac{m_i n_i}{2} \vec{v}_i^2 \right) \vec{v}_i + \vec{\Pi}_i \cdot \vec{v}_i + \vec{q}_i \right) = (q_i n_i \vec{E} - \vec{R}) \cdot \vec{v}_i - Q_{ei} + S_{E_i} \quad (\text{A.17})$$

and electrons

$$\partial_t \left( \frac{3}{2} n_e T_e \right) + \nabla \cdot \left( \frac{5}{2} n_e T_e \vec{v}_e + \vec{q}_e \right) = (q_e n_e \vec{E} + \vec{R}) \cdot \vec{v}_e + Q_{ei} + S_{E_e} \quad (\text{A.18})$$

The energy source term  $S_E$ , the heat fluxes  $q_x$  as well as the energy exchange term  $Q_{ei}$  ensure the energy conservation. The energy exchange term is given by

$$Q_{ei} = \frac{3m_e n_e}{m_i \tau_e} (T_i - T_e) \quad (\text{A.19})$$

where the collision frequency  $\tau_x$  is used

$$\tau_x = \frac{3}{4\sqrt{\pi}} \frac{\sqrt{m_e} T^{3/2}}{n_i q_x^2 e^2 \ln \Lambda} \quad (\text{A.20})$$

with the Coulomb logarithm defined by

$$\ln[\Lambda] = 15.2 - 0.5 \ln \left[ \frac{n_e}{10^{20}} \right] + \ln \left[ \frac{T_e}{1000} \right] \quad (\text{A.21})$$

The heat fluxes are given by the following equations for ions

$$\vec{q}_i = -\kappa_{\parallel}^i \nabla_{\parallel} T_i - \kappa_{\perp}^i \nabla_{\perp} T_i + \kappa_*^i \frac{\vec{B}}{B} \times \nabla_{\perp} T_i \quad (\text{A.22})$$

and electrons

$$\vec{q}_e = -\kappa_{\parallel}^e \nabla_{\parallel} T_e - \kappa_{\perp}^e \nabla_{\perp} T_e + \kappa_*^e \frac{\vec{B}}{B} \times \nabla_{\perp} T_e - 0.71 \frac{T_e j_{\parallel}}{e} - \frac{3}{2} \frac{T_e}{e \omega_e \tau_e B} \vec{B} \times \vec{j}_{\perp} \quad (\text{A.23})$$

with the electron cyclotron frequency  $\omega_e$ . The thermal conductivities  $\kappa_y^x$  and the parallel viscosity  $\eta$  are given by

$$\begin{aligned} \kappa_{\parallel}^e &= \frac{1.35}{\sqrt{m_e} q_e^4} \frac{T_e^{5/2}}{Z_{eff} \ln \Lambda} \\ \kappa_{\parallel}^i &= \frac{1.51}{q_e^4} \sum_a \frac{Z_a^{-2} n_a}{\sum_b n_b Z_b^2 \sqrt{\frac{2m_a m_b}{m_a + m_b}}} \frac{T_i^{5/2}}{\ln \Lambda} \end{aligned} \quad (\text{A.24})$$

The Braginskii equations in this section are taken from [96] whereas the transport coefficients are taken from [95].



## A.7 Mean free path - First Ionization

As an example of the atomic data used by EIRENE the ionization length of neutral tungsten is shown. The ionization length was evaluated from the modified ADAS data for electron impact ionization of neutral tungsten. This ionization length forms the basis of the prompt redeposition model presented in subsection 3.3.1.2. The following figure shows the mean free path of a tungsten atom to its first ionization at different electron densities and temperatures.

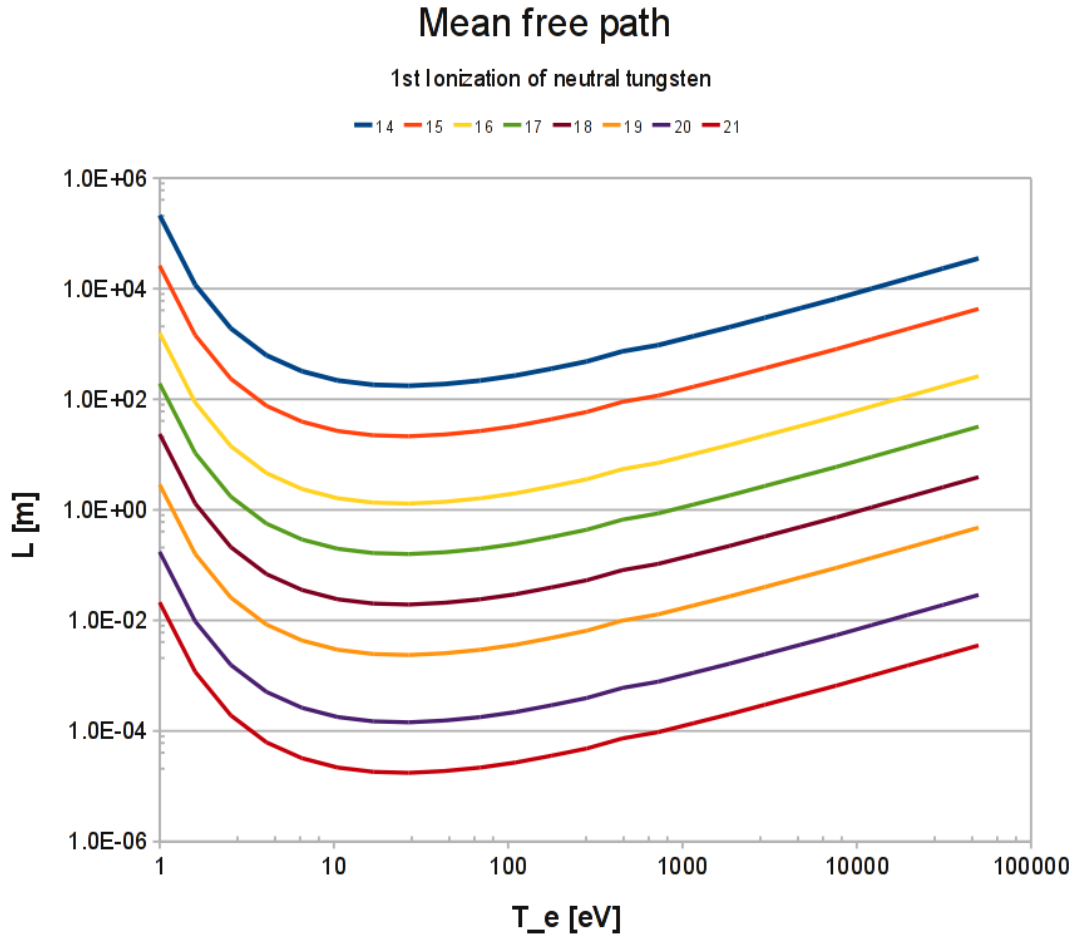


**Figure A.9:** Mean free path to first ionization event after calculated with EIRENE reaction coefficients.